DESIGN AND COMMISSIONING OF PULSED WIRE MAGNETIC MEASUREMENT SYSTEM FOR INSERTION DEVICE CHARACTERIZATION

A Thesis submitted for the Master's degree of Synchrotron Radiation Based Science
by

Mohammed Ebbeni

Department of Physics, Synchrotron Radiation Division, Lund University

Supervised by Hamed Tarawneh and Sverker Werin

March 2021

LUND
UNIVERSITY

Abstract

Synchrotron and Free Electron Laser (FEL) light is becoming an increasingly sought after tool for almost all scientific research aspects. MAX IV Laboratory introduced the first 4^{th} generation light source that provides the brightest synchrotron light in the world. Since all of the experiments at MAX IV rely only on Insertion Device (ID) radiation, the need for improving ID technology has subsequently been prioritized.
The Pulsed Wire (PW) magnetic measurement system could prove to be an excellent solution for the construction and tuning of small aperture and limited access ID designs which are under investigation for the proposed FEL project at MAX IV.
Therefore this thesis is dedicated to show the simulation, design and commissioning results of a PW system developed at MAX IV Laboratory, as well as comparisons against well proven magnetic measurement techniques.

Acknowledgements

I am grateful to have been given the chance to develop a cutting edge system and myself in the process, this goes to my supervisors, Hamed Tarawneh and Sverker Werin who have given me the vision and motivation to carry out this work.

My gratitude also goes to MAX IV Laboratory, where the work was carried at the Insertion Device group that showed an increased interest in this project and provided everything that was needed for its progress and countless contributions and discussions. The Engineering group has also provided technical designs and assistance throughout the project for which I am grateful.

I am grateful to my parents that were always a great source motivation and prepared me with love, support, education and motivation to seek a career in science and research. And grateful that my wife was by my side providing immense support and a graceful patience.

Contents

List of Figures

List of Tables

1 Introduction

Magnets are essential components in the construction of particle accelerators as they can curve the trajectory of charged particles which can be useful to contain them in a ring by curving their trajectory 360° in total, or to focus the particle beam to keep its size within limits.
Magnets can also be used to generate light from an electron beam, these magnets are called Insertion Devices (IDs), and they operate by rapidly curving the electron beam transversally when passing through them.

These processes must be kept well under control in order to meet the demand of today's accelerators and users, and therefore, magnets used in particle accelerators need to be well measured to control and correct their -inevitable- manufacturing defects and ensure their operation as intended.
The most common technique for measuring the magnetic fields within an insertion device is the Hall-Probe mapper (HP) which is a well known and straight forward method. It works by placing a magnetic sensor (the Hall-probe) on a moving arm and record the magnetic field at the desired locations. This method suffers from the need to have side-way access to place the probe into the magnetic field which is not always possible or can lead to an over sized insertion device design, increasing cost and complexity.

The Pulsed Wire (PW) is an alternative technique for performing magnetic measurements, it works by creating vibrations within a wire that correspond to the magnetic field surrounding it. This is achieved by sending a current pulse through the wire. By measuring and analyzing these vibrations, we can determine the magnetic field and check the performance of the magnets before installing them in an accelerator system.

This project was aimed at designing, constructing and testing a pulsed wire system which can be used to measure the magnetic fields of insertion devices where access is limited, as this method requires space only for a thin wire and has the potential to change the way IDs are currently constructed and enable designing closed structure IDs with small footprint, reducing their cost and complexity. This benefit becomes especially important for FEL undulators, where tens of identical IDs must be built, measured, tuned and installed.

During this master's project the PW system was designed, constructed and commissioned.

Design: A mathematical model was used for calculating the wire oscillations resulting from the magnetic field and vice versa, a novel method was introduced to recover the magnetic field information from any given pulse shape.
The model was used to run various simulations identifying the shape and boundaries of the wire oscillations to be expected for different insertion devices. Then the components of the system were selected accordingly.
An optical wire position sensing unit was also simulated and designed during this project,

which offers varying sensitivity and range to accommodate different oscillation levels to be expected from different IDs and wires.

Construction: The system was built to be ready for performing magnetic measurement on full scale insertion devices, therefore, various degrees of freedom were implemented to position the wire and sensors freely within the magnetic field. The sensing electronics were also selected to have a high degree of tunability.
Control software was written to automate the process as much as possible and offer an easy to use Graphical User Interface (GUI) in which the operator can tune the system's parameters to quickly and systematically obtain results.

Commissioning: A full size insertion device was measured using the HP system and used as a reference to compare the PW results against. External factors that influence the measurement were identified and methods for their corrections were introduced.
Finally, measurements were obtained and compared against the reference data.

Improvements: Experimental results reveal shortcomings of the mathematical model, were some unexpected behaviors were observed and could not be explained. An experimental method was found to reduce the effect of these anomalies and a more inclusive model is suggested and simulated to try and explain the experimental results.

2 Synchrotron Radiation

Light is a form of radiated electromagnetic field, which is a part of the field that gets detached from the source charge and propagates into infinity. According to classical electrodynamics this is only possible when the source charge undergoes acceleration, and therefore, accelerating charged particles can be an effective method of generating radiation.

2.1 The Synchrotron

The force needed to accelerate a charged particle is known as the Lorentz force, which acts through electric $\boldsymbol{E}$ and magnetic $\boldsymbol{B}$ fields only. The acceleration of a charged particle also changes its momentum $\boldsymbol{p}$, the Lorentz force and momentum change of a particle in an electromagnetic field is described by the equation [1]:

$$\boldsymbol{F} = \boldsymbol{p'} = m_0 \gamma \boldsymbol{v'} = q(\boldsymbol{E} + \boldsymbol{v} \times \boldsymbol{B}) \tag{2.1}$$

We can see that electric fields are capable of accelerating particles in the direction of the field, which can be aligned with the direction of motion to achieve energy gain to the particles. Magnetic fields however can only accelerate particles perpendicular to their direction as well as the particle's direction of motion ($\boldsymbol{v} \times \boldsymbol{B}$) and their force is proportional to the particle's speed, which is why magnetic fields can only be used to "bend" the trajectory of moving charged particles.
Also to note is that acceleration is inversely proportional to a particle's mass, which is why accelerator based light-sources use electrons as accelerated particles due to their small rest mass as well as their ease of generation.
A synchrotron is an accelerator machine in which the particle beam is kept in a fixed trajectory (orbit) while being accelerated, this is achieved by "synchronizing" the magnetic field in the machine with the beam's energy.
Figure 1 (Source: [2]) shows the main components of a synchrotron storage ring machine. A beam of electrons is accelerated in a previous stage either to their full energy or to an intermediate level, they are then injected into the storage ring via the Injector Magnet.
Once inside the ring, Bending Magnets keep the electrons confined within by applying a total of 360° deflection angle, allowing the beam to be "stored" for long time periods.
Electrons can get scattered and lost when interacting with matter, therefore near-absolute vacuum levels are required to maintain the electron beam for prolonged periods of time, and must be contained within a Vacuum Chamber surrounding its trajectory.
The electron beam loses energy in the form of synchrotron radiation as it travels through the storage ring. Therefore, the Radio-Frequency Cavity maintains an alternating electric field, which compensates for the lost energy of the electrons.

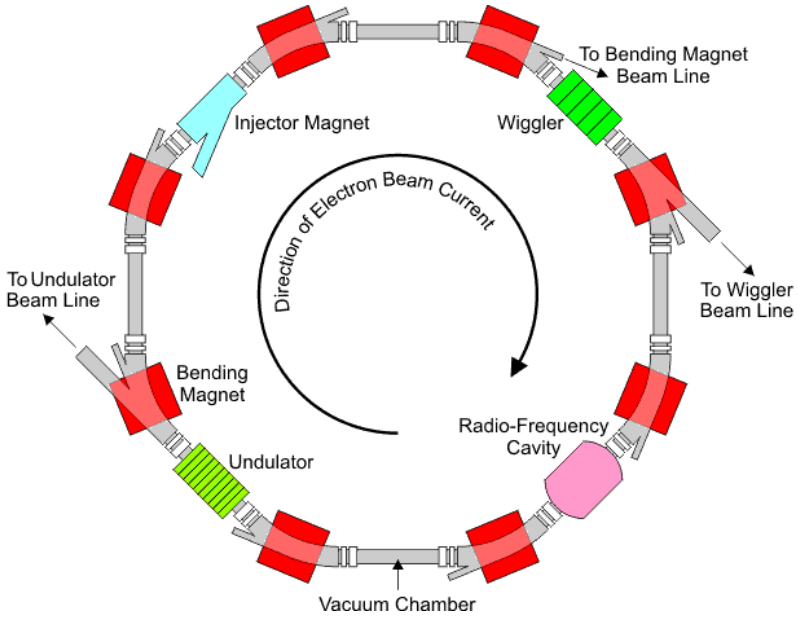

Figure 1: Schematic of a synchrotron storage ring.

2.2 Synchrotron Radiation Experiments

Synchrotron radiation is emitted from the electron beam within the Bending Magnets as well as Insertion Devices (Wigglers and Undulators), this radiation is then transported to the Beamlines where it can be used for probing various samples for research.
A single storage ring can house several Beamlines, each will be designed for a particular type of research, here we present an example of NanoMAX Beamline at MAX IV Laboratory, which is an X-ray imaging beamline capable of achieving *nm* resolutions.

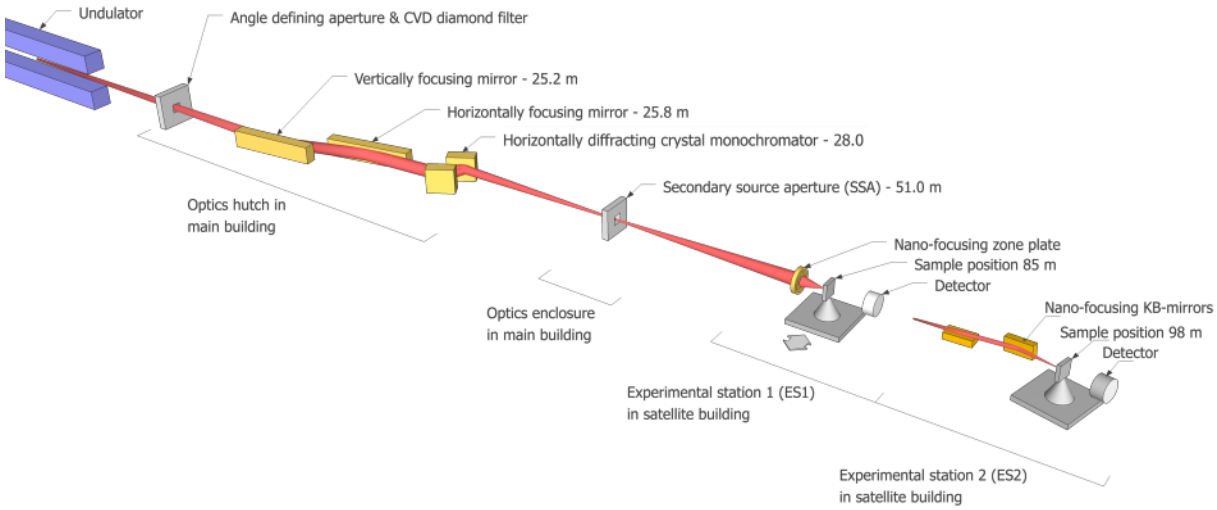

Figure 2: Schematic of Beamline Optics and Components.

Figure 2 (Source: [3]) shows the NanoMAX Beamline optical components. The hard X-rays start from the Undulator and pass through apertures that absorb of-axis radiation which are also off-energy. The beam goes through Vertical and Horizontal focusing mirrors followed by a monochromator, this allows only the required wavelength of light to pass through with a very narrow bandwidth. Final focusing before the sample is achieved by zone plates, which reduce the beam size to *nm* scale.
The sample gets scanned by translation stages, while the detectors behind the sample record the pattern and intensity of the transmitted light and an image of the sample can be obtained.

2.3 Insertion Devices

Modern 4th generation accelerator-based light sources rely solely on Insertion Devices (ID) for light generation. An ID is an array of periodically alternating magnetic poles which produces a semi-sinusoidal magnetic field. An accelerated electron beam passes through the magnetic field and experiences sinusoidal acceleration, this in turn produces high energy X-ray light. More details are provided in appendix A.

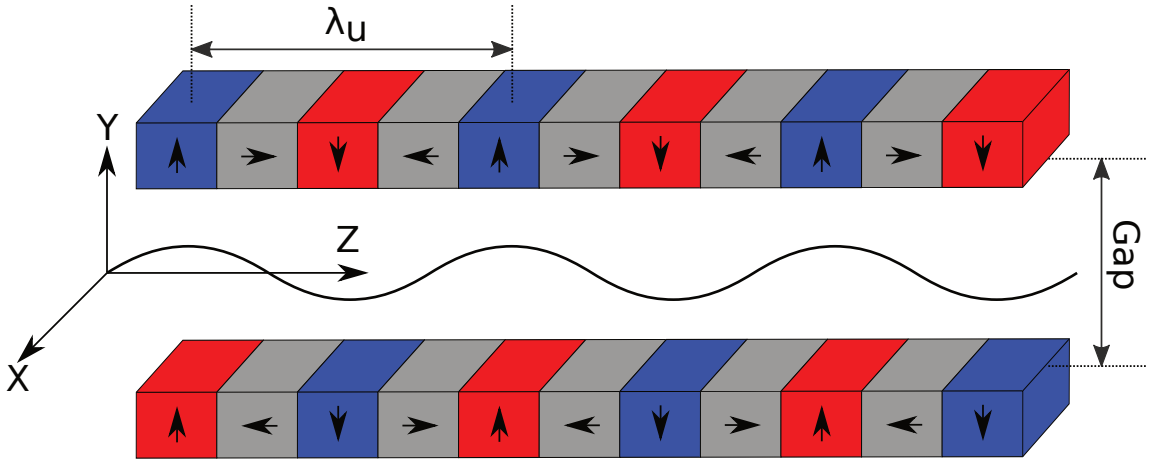

Figure 3: Schematic of an Insertion Device

Figure 3 shows the basic schematic of an ID indicating the period length λ_u and the gap distance as well as the coordinate system which shall be used throughout this document.

Insertion devices are typically large and heavy machines with length measured in meters and tens or hundreds of magnetic periods exerting large magnetic forces between its arrays in the order of kN.
The periodic magnetic fields within an insertion device are usually generated using permanent magnet arrays, but can also be generated using normal or super-conductive electromagnets. These field sources can be placed either outside the vacuum chamber containing

the electron beam or within a common larger vacuum vessel and operated at room or cryogenic temperatures.
Regardless of the construction technology of the insertion device, magnetic field errors will be present due to the accumulated manufacturing tolerances, defects of the sources and interactions within the mechanical and magnetic components.
All accelerator magnets require a quality control check that involves measuring the magnetic field to determine if it falls within the acceptable error levels. In the case of IDs the magnets are rarely acceptable immediately after their physical constructions.
This is why IDs need to go through a phase of tuning to achieve the required performance figures described in appendix B before they can be used in an experiment.
This tuning process is generally referred to as "shimming" and involves measuring the magnetic field and making small adjustments to the local field of each half-period of each magnet array making up the ID. The process of taking measurement and making small changes is repeated over and over until all errors fall within the acceptable limits.
It is then clear that the quality of an insertion device will eventually be determined during the shimming process that aims at ensuring the sensitive nature of its operation. And this in turn is limited by the accuracy and precision of the available magnetic measurement instruments used during the process (see appendix C).

3 Pulsed Wire Magnetic Measurement Technique

The Pulsed Wire (PW) technique can be considered the holy-grail of magnetic measurements for insertion devices. It attempts to combine the benefits of traditional measurement techniques into one, i.e. obtaining local magnetic field information using a long thin wire, without the need of lateral access.

In principle it consists of a thin wire placed in a magnetic field. Force is exerted on the wire when current is passed through due to the Lorenz force (equation 2.1). The forces generate a traveling wave in the wire that is detected by optical sensors that measure the passing wave in time. From this, the magnetic field causing this wave can be known in space, providing local measurement of the IDs field. See figure 4 for a schematic illustration.

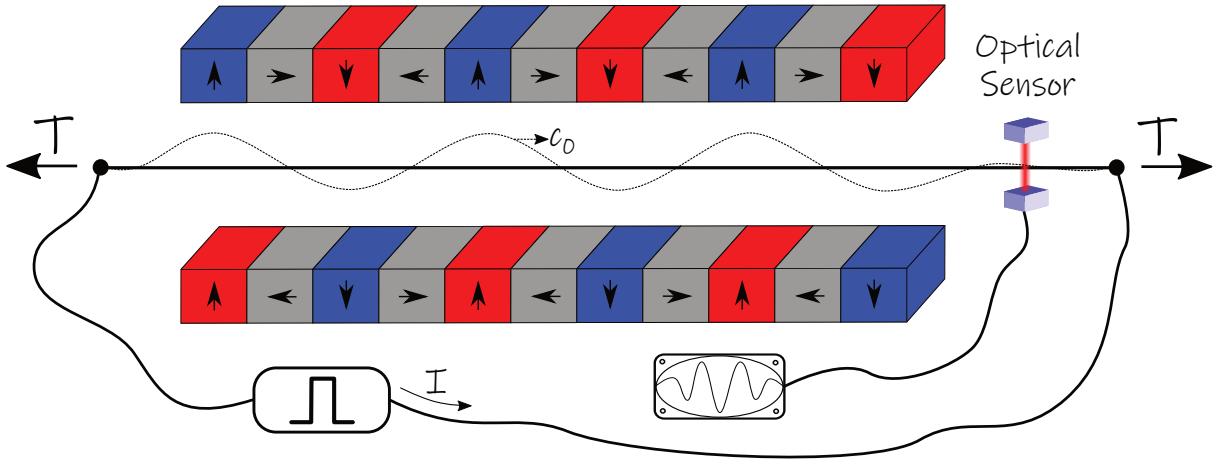

Figure 4: Sketch of the pulsed wire measurement setup.

For the ideal case of a thin flexible wire, the governing relation of the PW system can be expressed as loaded tensioned string [11]:

$$-T\frac{\partial^2 u_x}{\partial z^2} + \mu\frac{\partial^2 u_x}{\partial t^2} = B_y(z)I(t). \tag{3.1}$$

Where the u_x is the horizontal wire oscillation, μ is the linear mass density of the wire, T is the wire tension, $I(t)$ is the current pulse and $B_y(z)$ is the vertical magnetic field. This is the wave equation for a wave travelling at a constant speed of $c_0 = \sqrt{\frac{T}{\mu}}$.
When solved for a current pulse of amplitude I_m and width δt, the wire oscillations take the form:

$$u_x(t) = \frac{I_m}{2T}\int_{c_0(t-\delta t)}^{c_0 t}\int_0^{\tilde{z}} B_y(\hat{z})\cdot d\hat{z}d\tilde{z}. \tag{3.2}$$

If a short current pulse ($c_0\delta t \ll \lambda_u$) is applied to the wire, the resulting oscillations at the

detection point turn out to be proportional to the 1st integral of the magnetic field:

$$u_x(t) = \frac{I_m \delta t}{2 c_0 \mu} \int_0^{c_0 t} B_y(\tilde{z}) \cdot d\tilde{z}. \tag{3.3}$$

Two waves traveling in opposite directions are in fact generated, and only the one traveling towards the detection point ($z = 0$) is considered. The horizontal and vertical magnetic fields would generate their own separate traveling waves independently and can both be detected using two optical sensors. However, the longitudinal magnetic field doesn't exert any force on the wire due to the cross product in the Lorentz force and therefore cannot be detected using this method and it is usually of no interest in insertion devices as discussed in section B.5.

This measurement technique has the advantage of rapidly obtaining local field information without the need of lateral access nor specialized supports in the insertion device. Therefore it carries the promise of replacing Hall-probe based measurements. This is especially advantageous for small gap and in-vacuum insertion devices.

3.1 Pulsed Wire Challenges Overview

This Pulsed Wire method has been investigated since the late 80's [12], where it was found to be very delicate and can be influenced by many internal and external factors that hindered its potential advantages and limited its application.
The challenges found in this technique including:

- Dispersion: The wave propagation speed is different for different frequency components, this is due to the rigidity (stiffness) of the wire material [12][13].
- Pulse shape: The current profile will differ from the analytical formulation used in corrections algorithms.
- Wire sag: Gravity forces the wire shape into a parabola in the vertical direction, this means that the field is not measured along a straight axis.
- Wave scattering: Non-homogeneous wire material and shape could scatter the traveling waves and affect the measurement results [12]. The wire deformation due to the traveling waves can also cause inhomogeneity effecting the wave itself.
- Background vibration sources: Floor vibration, air movement and motorized stage closed-loop all contribute to background vibrations of the wire and sensors.
- Electrical noise: The output of any analogue electronic system will always contain background noise that could effect its performance.

- Calibration: Any sensor used to measure a physical quantity can be susceptible to calibration errors and non-linearity.
- Induced currents: The motion of a conductive wire in a magnetic field induces a voltage across the wire length, which produces secondary currents in the wire at resonance with the traveling wave.

These mentioned effecting factors will be tackled during this study using simulations and experimentation. Solutions to these problems will be given when applicable to make better use of this system for performing magnetic measurements.

3.2 Dispersion

In order to obtain a more representative model of the pulsed wire system behaviour, we need to take into account the flexural rigidity of the wire in order to describe the dispersion effect which causes vibrations of different wavelengths to travel the wire at different speeds, similar to what happens when white light passes through a prism. This can be achieved by using the tensioned Bernoulli-Euler theory of beams which has the following loaded governing equation [13]:

$$EI_w \frac{\partial^4 u_x}{\partial z^4} - T\frac{\partial^2 u_x}{\partial z^2} + \mu \frac{\partial^2 u_x}{\partial t^2} = B_y(z)I(t). \tag{3.4}$$

Where E is the Young's modulus of the wire material and I_w is the moment of inertia, which in the case of the wire is $I_w = \frac{\pi}{64} Diameter^4$. Together, EI_w forms the flexural rigidity of the wire, a measure of its resistance to bending.
By injecting a travelling wave of the form $u = e^{-i(kz-\omega t)}$, we can obtain the relationship between the wavenumber k and the angular frequency ω under this model:

$$\omega(k) = c_0 k \sqrt{1 + \frac{EI_w}{T} k^2}. \tag{3.5}$$

Therefore, the phase velocity is:

$$v_p(k) \equiv \frac{\omega}{k} = c(k) = c_0 \sqrt{1 + \frac{EI_w}{T} k^2}. \tag{3.6}$$

And the group velocity:

$$v_g(k) \equiv \frac{\partial \omega}{\partial k} = \frac{2v_p^2(k) - c_0^2}{v_p(k)}. \tag{3.7}$$

So it is clear that the phase and group velocities aren't equal, therefore we have a formulated expression for the dispersion relationship.
The relationship between ω and k is therefore, $\omega = kc(k)$. Where $c(k) = v_p(k)$ is the phase velocity. Since all the above mentioned quantities can be known once the wave speed is

known, $c(k) = v_p(k)$ shall be referred to as the wave speed.
The inverse of equation 3.5 can be found by solving it as a quadratic equation to yield [14]:

$$k(\omega) = \sqrt{\frac{-T}{2EI_w} + \sqrt{\frac{T^2}{4E^2I_w^2} + \frac{T}{c_0^2 EI_w}\omega^2}} \tag{3.8}$$

3.3 Pre-Defined Pulse Response

The latest and most descriptive literature articles found have described the system's response using a Green solution method [13]. In it, the system's behavior to Dirac-delta function current pulse is obtained and used to calculate the response for selected cases of short and long current pulses. The Green's function describing the wave motion in any point in space and time is given as:

$$g(z,t) = \int_{-\infty}^{\infty} \frac{\overline{B}(k)}{2i\omega\mu} \left[e^{-i(kz-\omega t)} - e^{-i(kz+\omega t)}\right] \cdot dk. \tag{3.9}$$

And for the special case where we are observing the wire oscillations at a single point located in $z = 0$, and considering only the wave travelling towards the sensor $e^{-i(kz+\omega t)}$ from the region $z > 0$ containing the magnetic field, we have the Green's function:

$$g(t) = \int_{-\infty}^{\infty} \frac{i\overline{B}(k)}{2\omega\mu} e^{-i\omega t} \cdot dk. \tag{3.10}$$

With $\overline{B}(k)$ being the Fourier Transform of the magnetic field profile $B(z)$ defined as:

$$\begin{aligned} \overline{B}(k) &= \mathscr{F}\left[B(z)\right] = \frac{1}{2\pi}\int_{-\infty}^{\infty} B(z)e^{ikz} \cdot dz \\ B(z) &= \mathscr{F}^{-1}\left[\overline{B}(k)\right] = \int_{-\infty}^{\infty} \overline{B}(k)e^{-ikz} \cdot dk. \end{aligned} \tag{3.11}$$

Therefore, the oscillations at the sensor location ($z = 0$) will be the convolution of the Green's function and the current pulse $I(t)$:

$$u(t) = g(t) * I(t) = \int_0^t g(t-\tau)I(\tau) \cdot d\tau. \tag{3.12}$$

Equation 3.12 above was then used to calculate the oscillations resulting from a short current pulse $I(t) = I_m[H(t) - H(t-\delta t)]$, where $H(t)$ represents the Heaviside-step function. The resulting oscillations therefore were [13]:

$$u(t) = \frac{I_m}{2\mu}\int_{-\infty}^{\infty} \frac{e^{i\omega\delta t} - 1}{\omega^2}\overline{B}(k)e^{-i\omega t} \cdot dk \tag{3.13}$$

Furthermore, these results were used to find analytical correction functions to correct for the dispersion effect and the finite pulse width.

Similarly the oscillations of a bipolar square pulse can be worked out as follows, when assuming a current pulse $I(t) = I_m[H(t) - 2H(t-\delta t) + H(t-2\delta t)]$ into equation 3.12:

$$u(t) = \frac{-I_m}{2\mu} \int_{-\infty}^{\infty} \frac{(e^{i\omega\delta t} - 1)^2}{\omega^2} \overline{B}(k) e^{-i\omega t} \cdot dk \tag{3.14}$$

3.4 Arbitrary Pulse Response

The previous analysis found in literature has formulated the arbitrary current pulse response and used it to build analytical correction functions for specific cases of current pulses.
Here I present a novel alternative, in which the arbitrary current pulse is used throughout the treatment to both simulate the pulsed wire and recover the magnetic field from the wire oscillations.
Equation 3.7 can be rearranged into:

$$dk = \frac{d\omega}{v_g(k)},$$

which can be inserted into equation 3.10 and compared with equation 3.11 to yield:

$$g(t) = \int_{-\infty}^{\infty} \frac{i\overline{B}(k(\omega))}{2\omega\mu v_g(k(\omega))} e^{-i\omega t} \cdot d\omega = \mathscr{F}^{-1}\left[\frac{i\overline{B}(k(\omega))}{2\omega\mu v_g(k(\omega))}\right].$$

Therefore, we can write the Green's function in frequency domain as:

$$G(\omega) = \mathscr{F}\left[g(t)\right] = \frac{i\overline{B}(k(\omega))}{2\omega\mu v_g(k(\omega))}. \tag{3.15}$$

We can now apply the Fourier convolution theorem [15] on equation 3.12 to obtain the wire oscillations in frequency domain as:

$$U(\omega) = \mathscr{F}\left[u(t)\right] = \mathscr{F}\left[g(t) * I(t)\right] = 2\pi G(\omega)\overline{I}(\omega). \tag{3.16}$$

And substituting with 3.15 for $G(\omega)$ we finally arrive at:

$$U(\omega) = \frac{i\pi\overline{B}(k(\omega))\overline{I}(\omega)}{\omega\mu v_g(k(\omega))}. \tag{3.17}$$

Which allows us to easily describe the pulsed wire oscillations in terms of the magnetic field and current pulse in frequency domain, while at the same time correcting the dispersion effect due to the wire's stiffness.

In the hypothetical case of a non-dispersion wire material, equation 3.17 would reduce to:

$$U_0(\omega_0) = \frac{i\pi\overline{B}(k(\omega))\overline{I}(\omega_0)}{\omega_0\mu c_0}. \tag{3.18}$$

Where $c_0 = \sqrt{T/\mu}$ is the non-dispersion wave speed and $\omega_0 = kc_0$. Equations 3.17 and 3.18 can be combined to obtain a correction formula that would only correct the dispersion effect in the wire oscillations:

$$U_0(\omega_0) = \frac{c(k(\omega))v_g(k(\omega))\overline{I}(\omega_0(k))}{c_0^2\overline{I}(\omega(k))}U(\omega(k)). \tag{3.19}$$

On the other hand, the purpose of the pulsed wire system is to measure the magnetic field along the wire, and equation 3.17 can be re-arranged to become:

$$\overline{B}(k(\omega)) = \frac{-i\mu\omega v_g(k(\omega))U(\omega)}{\pi\overline{I}(\omega)}. \tag{3.20}$$

Here the angular frequency can be obtained directly from equation 3.8. And the magnetic field profile is obtained through an inverse Fourier transform operation:

$$B(z) = \mathscr{F}^{-1}\left[\overline{B}(k(\omega))\right] \tag{3.21}$$

Due to dispersion effects, the phase velocity $c(k)$ is not constant, therefore for discrete uniform values of ω we get non-uniform values for k and the standard Fast Fourier Transform (FFT) algorithms would yield incorrect results. Traditionally, the inverse Fourier transform had to be calculated manually by integration of each point in frequency domain for each point in space, a process which is time consuming. Luckily, there exist non-uniform FFT algorithms which yield accurate results in a short amount of time [16].

Looking again at equation 3.20, we notice that we had to perform a division over $\overline{I}(\omega)$ in order to obtain the magnetic field information. Therefore, in the pulsed wire technique, the current pulse must have enough frequency content to cover all the k components of the magnetic field.
The advantage of the proposed arbitrary current method is that now we can design a current pulse in frequency domain to give enough sensitivity for the magnetic field we want to measure, invert it back to time domain and apply it, without the need for analytical formulas for each current pulse case.
This approach allows us to worry less about accurately generating the current pulse, but rather accurately measure it. Which was found to be easier to do in practice. At the same time, it allows for the flexibility to generate endless pulse shapes without needing to find analytical correction functions for each case.
For instance, imagine we want to measure the magnetic field of an undulator with period length λ_u up to its nth field harmonic, then the maximum wave number we need to consider is $k_c = 2n\pi/\lambda_u$, which in frequency domain translates into $\omega_c = k_c c(k_c)$. Now let us assume a current pulse that contains only the needed frequency components, such that we only excite the frequency band from $-\omega_c \rightarrow \omega_c$, we can calculate the required current pulse in time domain to be:

$$\overline{I}(\omega) = H(\omega + \omega_c)H(\omega_c - \omega) \xrightarrow{\mathscr{F}^{-1}} I(t) = \frac{2\sin(\omega_c t)}{t} = 2\omega_c \operatorname{sinc}(\omega_c t). \tag{3.22}$$

The *sinc* shaped current pulse generates a flat frequency response up to the required cut-off frequency ω_c. Nevertheless, this method can also be used to calculate other pulses that amplify or attenuate certain frequency bands if needed.

3.5 Wave Speed Calculation

The wave speed of our tensioned wire is of crucial importance to the success of the pulsed wire measurement method, as it forms the link in converting the wire oscillation signals measured in time domain into a magnetic field map in space. Looking at equation 3.6, we see that it consists of two parts, c_0 which is also called the non-disperse wave speed and EI_w which is the flexural rigidity of the wire. Even though these values can be easily calculated or looked up in tables for the particular wire material, the actual value might differ. Which is why, the wave speed needs to be measured in-situ in order for pulsed wire results to be meaningful.
We can perform two measurements to obtain the wave speed, the first being with the magnet in a nominal position $B(z)$, while the other with the magnet displaced by Δz resulting in the field $B_\Delta(z) = B(z - \Delta z)$. The Fourier transform of two magnetic fields are then $\overline{B}(k)$ and $\overline{B_\Delta}(k) = \overline{B}(k)e^{ik\Delta z}$, respectively. By inserting the two fields into equation 3.17, we can see that the resulting wire oscillations are $U(\omega)$ and $U_\Delta(\omega) = U(\omega)e^{ik\Delta z}$, respectively.
Now we can also write the quantity $U^*(\omega)U_\Delta(\omega) = |U(\omega)|e^{ik\Delta z}$ which we can extract the phase information from to yield:

$$\phi(\omega) = \text{phase}(U^*(\omega)U_\Delta(\omega))) = k\Delta z \tag{3.23}$$

If we use $k = \omega/c$, we can write:

$$c(w) = \frac{\omega\Delta z}{\phi(\omega)} \tag{3.24}$$

Which can be used to fit $c(k)$ and obtain c_0 and EI_w from two measurements.
If instead we substitute equation 3.8 into equation 3.23 we obtain:

$$\phi(\omega, \Delta z) = k(\omega)\Delta z = \Delta z\sqrt{\frac{-T}{2EI_w} + \sqrt{\frac{T^2}{4E^2I_w^2} + \frac{\mu}{EI_w}\omega^2}}. \tag{3.25}$$

Using the relation in 3.25 above, we can fit any number of scans with two independent variables w and Δz instead of one. This has the potential to reduce the effect of noise as well as avoiding the division by the small and unstable phase values near $w = 0$.
It is worth mentioning that the more k components of the magnetic field available the better the fit results become, therefore, this measurement is preferably performed using a short magnetic field in space which will contain a broad range of wavenumbers.

3.6 Wire Sag Correction

The hanging wire will "sag" due to gravity in the vertical direction and thus the measured field within the ID will not be along straight line anymore. We can model the gravitation effect by replacing the magnetic force in equation 3.1 with the gravitation force μg:

$$T\frac{\partial^2 u_y}{\partial z^2} - \mu\frac{\partial^2 u_y}{\partial t^2} = \mu g. \tag{3.26}$$

However, in the static case, this can reduce to:

$$\frac{d^2 u_{y,static}}{dz^2} = \frac{\mu g}{T}, \tag{3.27}$$

which can be easily solved by integration:

$$u_{y,static}(z) = \int\int \frac{d^2 u_{y,static}}{dz^2} \cdot dz \cdot dz = \frac{\mu g}{2T} z^2 + C_1 z + C_2. \tag{3.28}$$

If we imagine the wire is put to nominal height $u_{y,static} = 0$ at the two ends of the undulator indicated by points $z = z_1$ and $z = z_2$, the boundary conditions $u_y(z_1) = u_y(z_2) = 0$ can then be imposed, resulting in:

$$C_1 = \frac{-\mu g}{2T}(z_2 + z_1) \quad \text{and} \quad C_2 = \frac{\mu g}{2T} z_2 z_1$$

And the wire shape due to sag can be written as:

$$u_{y,static}(z) = \frac{\mu g}{2T}\left(z^2 - (z_1 + z_2)z + z_1 z_2\right) \tag{3.29}$$

The magnetic field within a planner undulator is a periodic magnetic field of period λ_u, and its distribution can be written as [17]:

$$B_y(y, z) = A \cosh\left(\frac{2\pi}{\lambda_u} y\right) \cos\left(\frac{2\pi}{\lambda_u} z\right). \tag{3.30}$$

Therefore, we can write a compensation function for the effect of measuring along the wire sag in a magnetic field as:

$$f_{sag}(z) = \frac{B_y(0, z)}{B_y(u_{y,static}(z), z)} = \left(\cosh\left(\frac{2\pi}{\lambda_u} u_{y,static}(z)\right)\right)^{-1} \tag{3.31}$$

The magnetic field distribution described in 3.30 can also be obtained numerically through magnetic field simulations of the particular undulator design at hand to get a more accurate correction function.

3.7 Simulation Results

Before constructing the pulsed wire measurement bench, I have built a framework of MATLAB codes and later performed many simulations that were used in the design of the system later on, as well as check the integrity of the mathematical model proposed earlier for arbitrary current treatment. The same algorithm that is used for recovering the simulated wire oscillations is applied on the experimentally measured wire oscillations from the measurement bench.
The simulations are performed using the data measured by Hall-probe methods, which is a well proven technique that can be used as a reference throughout the remaining discussions. The emitted radiation from the undulators at MAX IV storage rings was found to correspond well with the calculations based on these Hall-probe measurements [18].

3.7.1 Large-Period Undulator Simulation

Most of the bench commissioning will be performed using an Elliptically Polarizing Undulator (EPU) at the Insertion Device lab in MAX IV Laboratory. This undulator is dedicated for testing in the ID lab and has a period length $\lambda_u = 69.1mm$ and a total length of $2m$.
Magnetic field data form a Hall-probe mapper was obtained earlier, this data was used to simulate the pulsed wire response such that magnetic field was converted to wire oscillations and then back to magnetic field.
Both the Hall data and the recovered fields from the pulsed wire were analyzed as described in section B to observe the impact of the pulsed wire.
Earlier I proposed the use of a *sinc* function in section 3.4 as a wide-band exciter. For practical reasons the *sinc* pulse was truncated in time to only the the part seen in figure 5. And the pulse width used in this simulation was $\delta t = 25\mu s$, corresponding to $f_c = \omega_c/2\pi = 1/\delta t$.

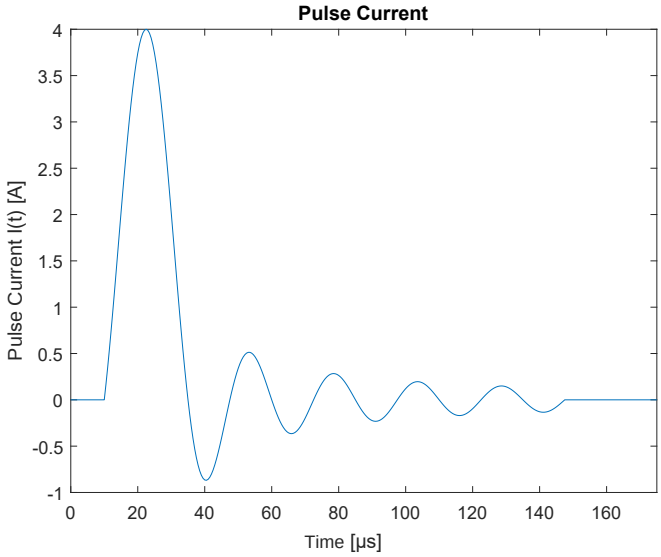

Figure 5: Truncated *sinc* current pulse of $25\mu s$ width.

The frequency components of the truncated *sinc* pulse can be evaluated using a Fourier Transform as seen in figure 6, which shows that oscillations up to $f_c = 40kHz$ can be efficiently excited.

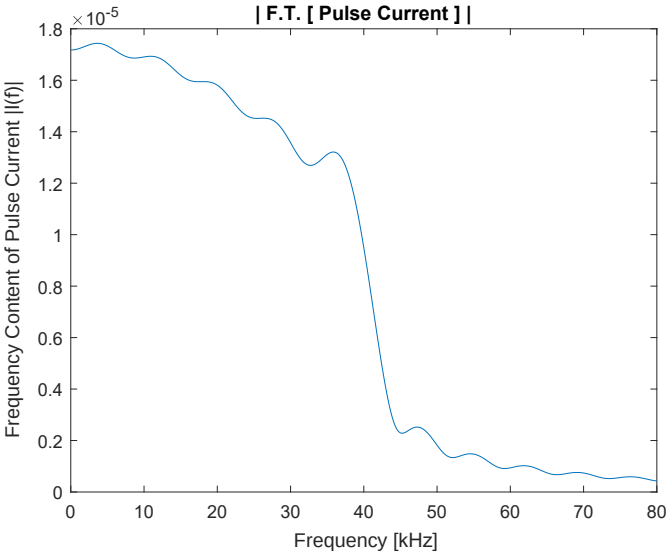

Figure 6: Fourier Transform of truncated *sinc* current pulse of $25\mu s$ width.

A wire $100\mu m$ in diameter, volumetric density $8800kg/m^3$ and a Young's modulus of $138GPa$ was used in this simulation with a tension force of $2N$. This resulted in the wire oscillations seen in figure 7, which shows both the wire oscillations resulting from the

pulse of figure 5 as $u_x(t)$ as well as the normalized Dirac-delta function response $g_x(t)$. The simulated wire oscillations were then restored back into magnetic field using the arbi-

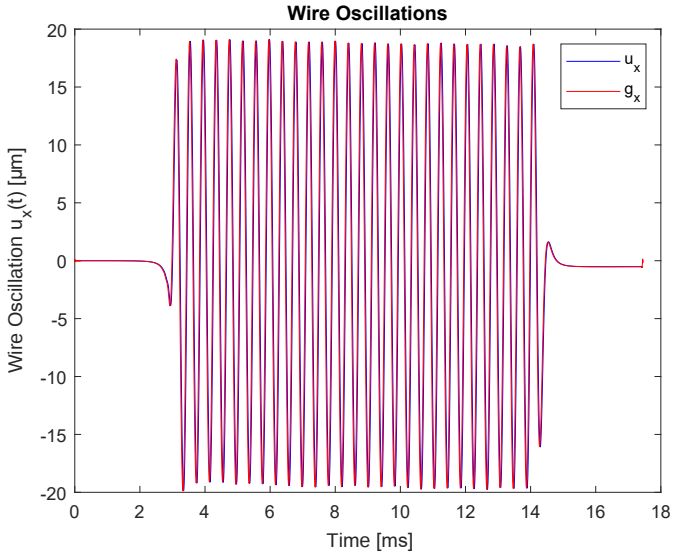

Figure 7: Simulated wire oscillations for a large period ID.

trary pulse response treatment proposed in section 3.4. The resulting fields are shown in figure 8. The standard results of ID analysis are summarized in table 1.

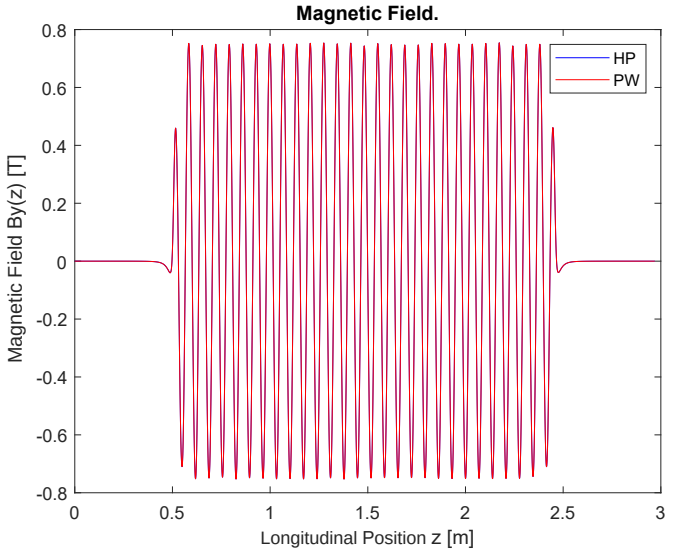

Figure 8: HP and recovered PW magnetic fields for a large period ID.

Parameter	HP	PW	Unit
λ_u	69.109	69.109	mm
B_{eff}	0.7513	0.7513	T
σ_ϕ	2.986	2.985	$^\circ$
I_1	-222.2	-224.5	$G.cm$
I_2	-39.440	-39.276	$kG.cm^2$

Table 1: Simulated PW results of large period ID compared against HP.

Table 1 shows excellent agreement between the Hall-probe and the simulated pulsed wire results. This raises confidence in the arbitrary pulse current method proposed. Nevertheless, this case of a large period ID contains very little dispersive effects, which is why the next case of small-period ID is studied.

3.7.2 Small-Period Undulator Simulation

The undulator of DanMAX beamline at MAX IV Laboratory was measured using Hall-probe, this ID has a period length of $\lambda_u = 16mm$ and a total length of $3m$. These conditions pose a greater challenge for the PW method as the traveling wave speeds will differ more due to the higher wave numbers involved, and the longer device length means more time for these components to separate.
For this device, a shorter pulse current is used, with $\delta t = 10\mu s$, as shown in figure 9.

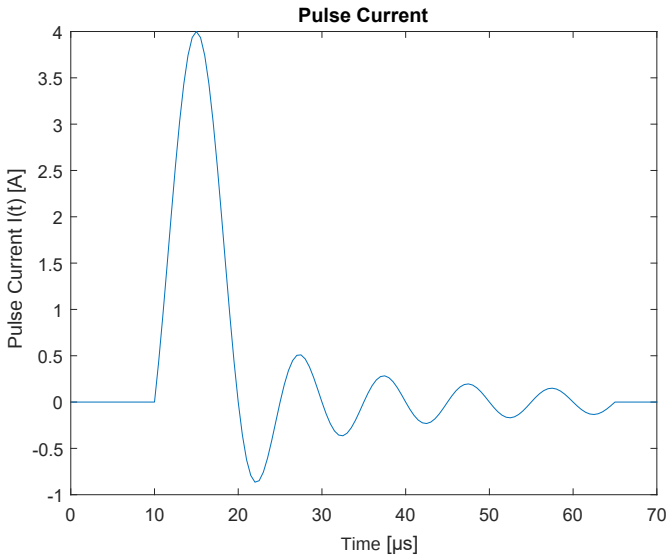

Figure 9: Truncated *sinc* current pulse of $10\mu s$ width.

As before, this can efficiently excite frequencies up to $f_c = \omega_c/2\pi = 1/\delta t = 100kHz$, which is shown in figure 10.

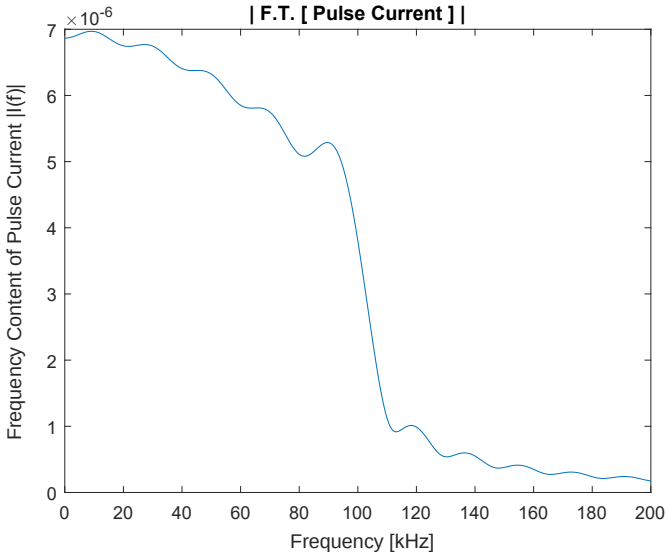

Figure 10: Fourier Transform of truncated *sinc* current pulse of $10\mu s$ width.

The wire oscillations in this case visibly show the effect of dispersion, where the higher frequencies lead the signal and the lower frequencies follow. This can be seen in figure 11.

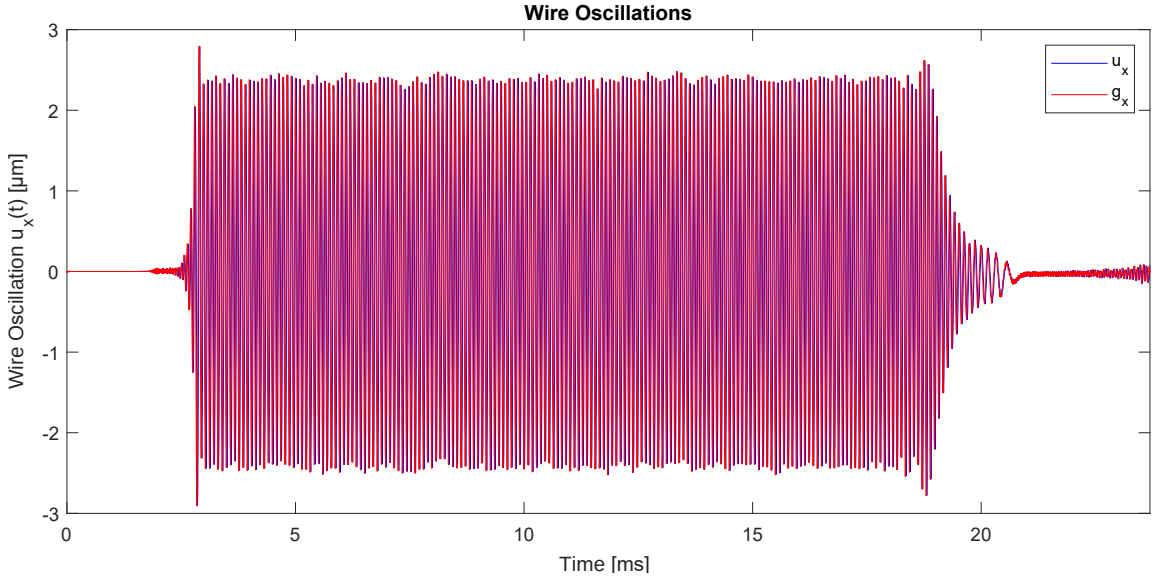

Figure 11: Simulated wire oscillations for a small period ID.

Despite the visible dispersion, the algorithm was able to correct for it and re-construct the magnetic field profile as seen in figure 12 and table 2.

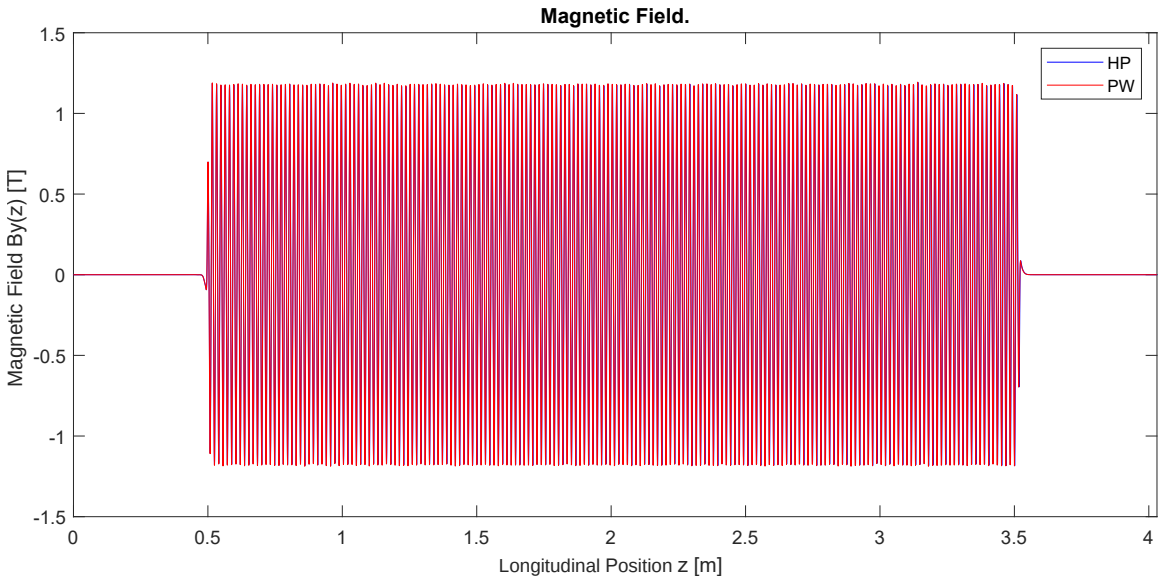

Figure 12: HP and recovered PW magnetic fields for a small period ID.

Parameter	HP	PW	Unit
λ_u	15.999	15.999	mm
B_{eff}	1.1217	1.1216	T
σ_ϕ	2.078	2.079	$^\circ$
I_1	-28.5	-28.6	$G.cm$
I_2	-10.400	-10.413	$kG.cm^2$

Table 2: Simulated PW results of small period ID compared against HP.

Here table 2 also shows excellent match in the ID parameters from a reconstructed PW signal. Both the pulse shape and the dispersion were efficiently corrected without major errors. These simulations aim to prove the effectiveness of the arbitrary current pulse method once all the involved parameters are known accurately, such as wire's tension, diameter and Young's modulus as well as the current pulse profile.

3.7.3 Wave Speed Measurement Simulation

In order to check the integrity of the wave speed measurement method described in section 3.5, a simulation model was built. The simulation uses the magnetic field of a single period of wavelength $\lambda = 16mm$ as a source of wide-band oscillation generator. This field is shown in figure 13.

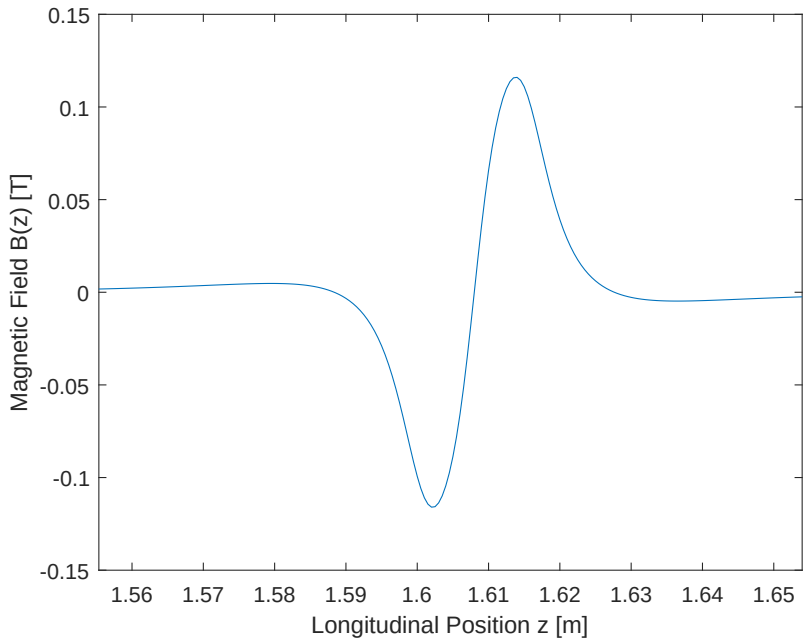

Figure 13: Short single period magnetic field used for wave speed measurement simulation.

In this study, six simulations were performed where the magnetic field was shifted by $\Delta z = 0, 10, 20, 30, 40$ and $50mm$. To test the robustness of this method, a number of expected errors were added to the simulation. These errors are summarized in table 3.

Δz	5	μm	RMS
T	5	mN	RMS
Wide-band Gaussian noise	5	nm	RMS
Wire eigenfrequency 37Hz	250	nm	Amplitude

Table 3: Simulated errors within the wave speed calculation.

The magnetic field was used to simulate the wire oscillations, and the above errors were imposed, resulting in the wave forms shown in figure 14.

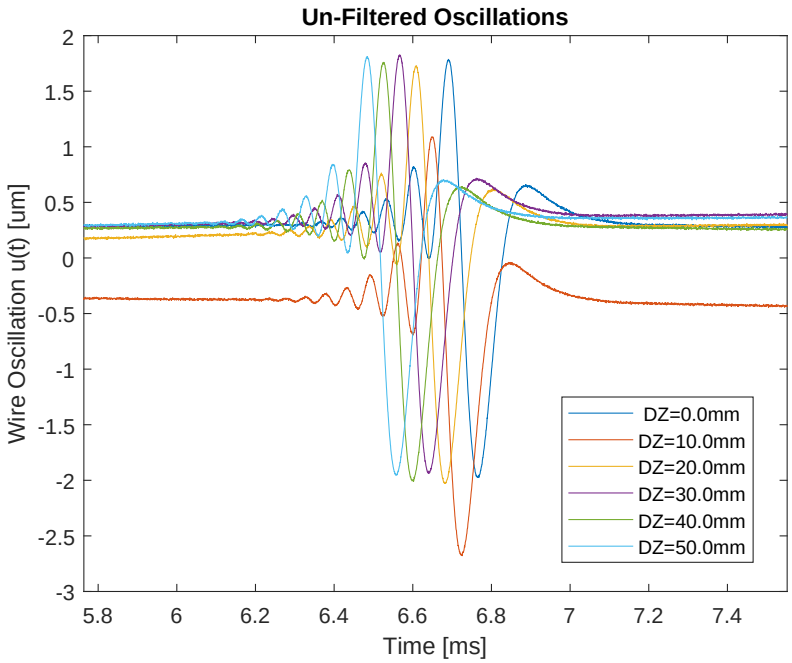

Figure 14: The wire oscillation patterns used in the wave speed calculation simulation.

The phase difference as a function of frequency between each pair of wave forms was calculated in correspondence with equation 3.23. This resulted in fifteen phase data sets that are shown in figure 15. These data sets were used in a fitting function as described in equation 3.25.

The wave speed of the raw data as well as the fit result is shown in figure 16, which shows how the wave speed is affected by the random noise which is why a large number of data set is preferred.

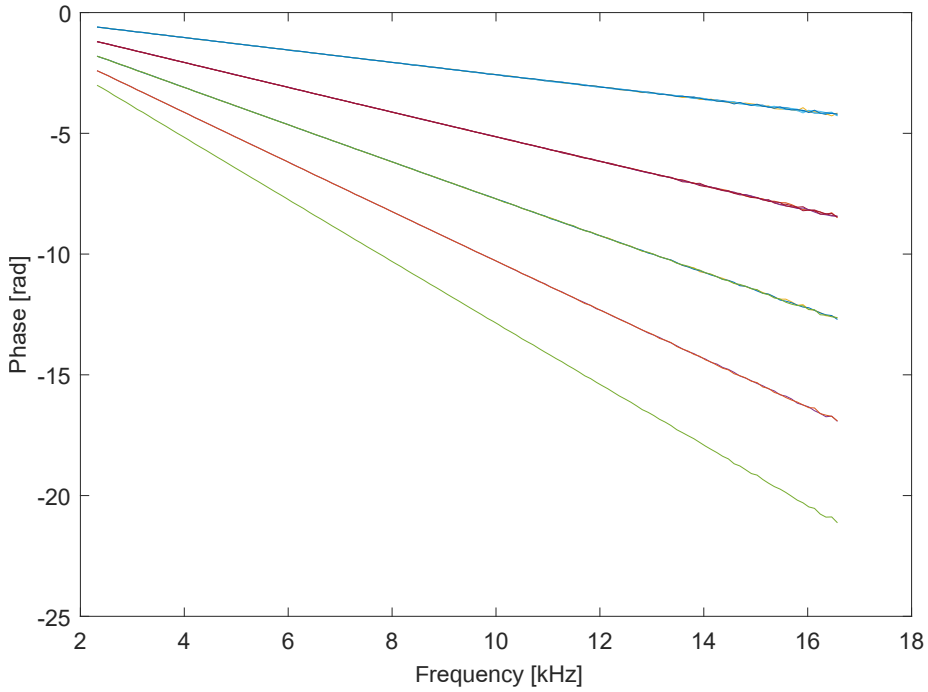

Figure 15: The phase differences used in the wave speed simulation.

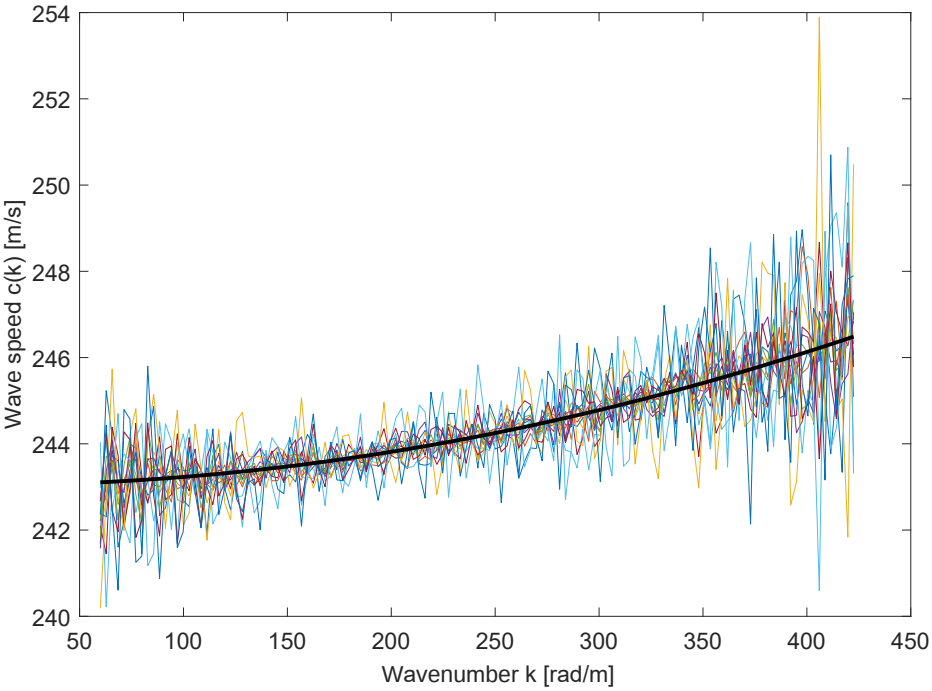

Figure 16: The simulated wave speed and fitting result.

The model of dispersion was used in the fitting process to identify the non-dispersive wave speed c_0, the flexural rigidity EI_w as well as the wire's tension T. The initial guessed values for the fitting algorithm were artificially deviated in order to show the robustness of this method.
The values actually used in the simulation, the guessed and those resulting from the fitting process are summarized in table 4.

Parameter	Actual	Guessed	Fit	Unit	Error
c_0	243.001	267.301	242.997	m/s	-0.0017%
EI_w	6.507e-07	1.607e-06	6.555e-07	$N.m^2$	0.7294 %
T	4.000	3.760	4.000	N	-0.0034 %

Table 4: Simulated wave speed calculation results.

The largest amount of error falls on the flexural rigidity of the wire, this is mainly because it is already such a small value to begin with, and the dispersion effect produces small differences in the wave speed. Nevertheless, knowing this quantity accurately is crucial for the success of the pulsed wire method.
The values resulted from the fitting process were used to re-construct the magnetic field form the wire oscillations which is shown in figure 17. It shows that the magnetic fields were correctly reconstructed following the wave speed characterization.

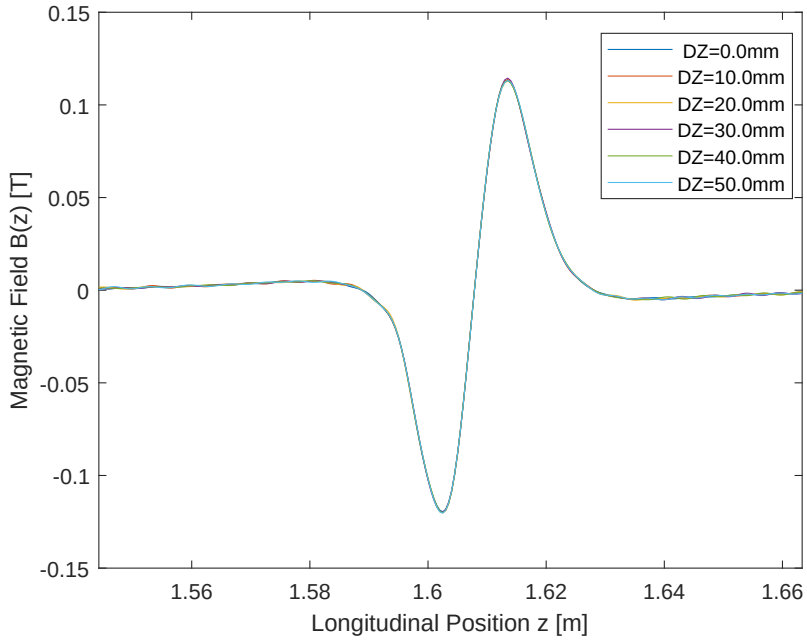

Figure 17: The re-constructed magnetic fields after the simulated wave speed characterization.

4 System Design, Setup and Troubleshooting

The need for a pulsed wire magnetic measurement system at MAX IV Laboratory falls under two folds, the first is the ability to measure the performance of In-Vacuum undulators and the second is to allow compact "Table-Top" closed structure undulators, primarily for the proposed Free Electron Laser (FEL) project.
Due to the variety in the undulator types and therefor sizes, the system was designed as a hybrid of a Stretch Wire (SW) system for field integrals as well as a Pulsed Wire (PW) for local field information.

4.1 Sensor Design

The pulsed wire system encodes magnetic field information into a wave traveling through a thin wire, therefore, a non-contact high-bandwidth method of measuring the wire position over time is required. And an optical sensor was designed as shown in figure 18.

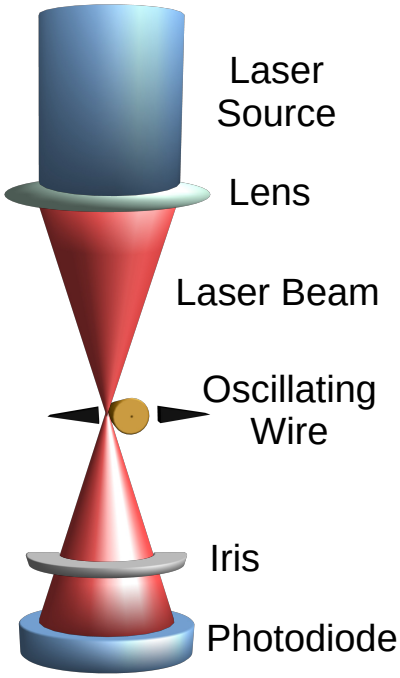

Figure 18: Sketch of optical wire position sensor.

A visible laser source is focused by a lens to create a small spot size, and the intensity of the laser beam is detected by a photodiode. The wire intersects the beam at or near the focal point, which partially casts a shadow over the photodiode active area, thus reducing its photocurrent output. Therefore, a signal correlated with the wire position is obtained. A red laser with a wavelength of $670nm$ is used, and as seen from previous simulations, the wire oscillations are in the order of $1\mu m$, this raised concerns about the presence of

diffraction effects. Therefore, light wave propagation calculations were coded into the PW MATLAB framework which were used to perform diffraction simulations. These simulation are shown below and validate the concern that the wire does not in fact cast a classical "shadow" over the photodiode.

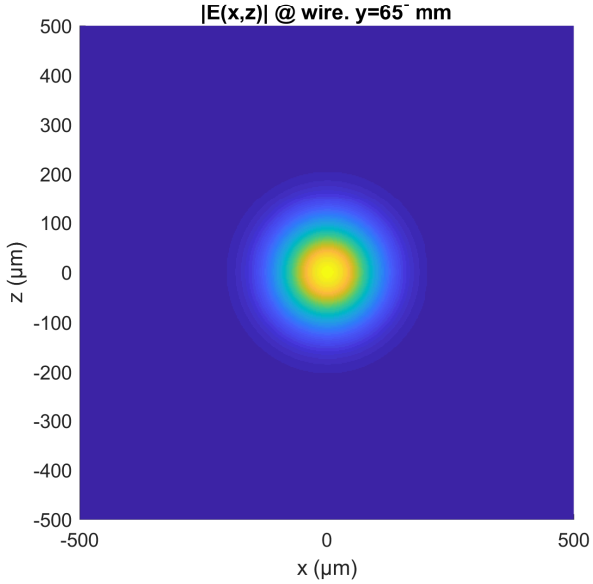

Figure 19: Laser E-field distribution immediately before wire ($y = 65^{-}mm$).

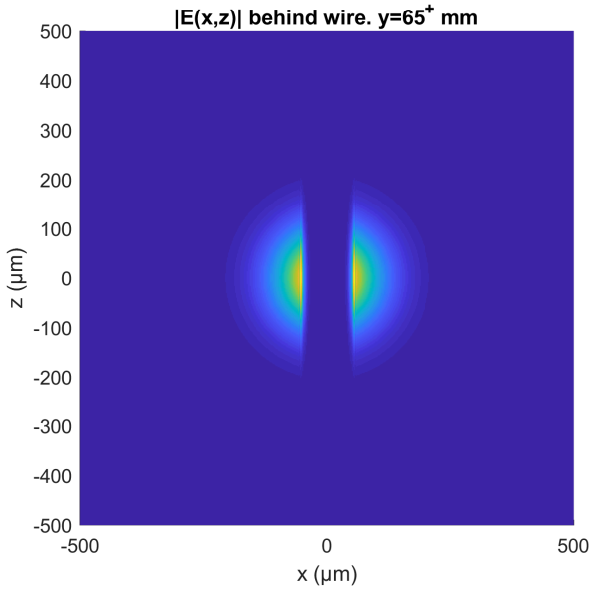

Figure 20: Laser E-field distribution immediately behind wire ($y = 65^{+}mm$).

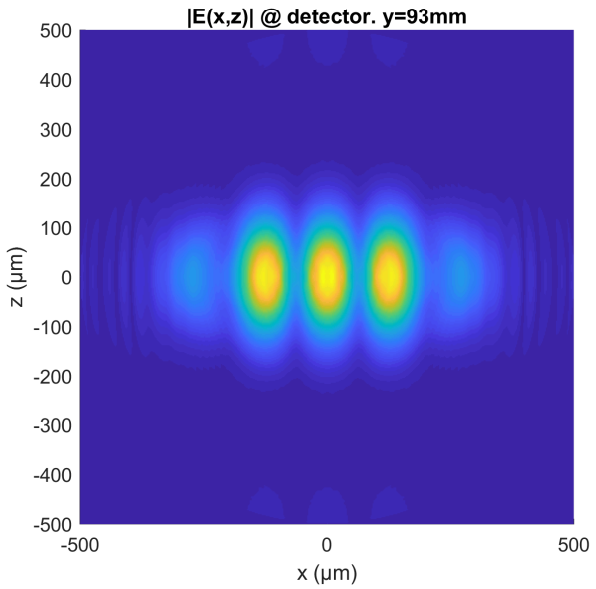

Figure 21: Laser E-field distribution on photodiode detector ($y = 93mm$).

The above simulations were performed using a Gaussian laser beam (figure 19). The $100\mu m$ wire is intersecting the center of the beam (figure 20), the EM wave was then propagated to the location of the photodiode, passing the iris (figure 21). It is then clear that diffraction effects are present within this sensor arrangement.
The photodiode output current is proportional to the power incident light over its surface, which is the integral of the intensity. Thus regardless of the distribution of the light, the amount of blocked laser power due to the wire is what provides the signal, and the sensitivity to the wire location is still maintained with the diffraction effects present. Figure 22 shows the simulated output current of the photodiode as the wire is moved across the laser beam, taking into account diffraction effects.

To detect displacement efficiently, the wire is placed in the midpoint of either the falling or rising slope ($x \approx \pm 75\mu m$ in figure 22) which will effectively create a signal correlated to the wire's position.
Sensor output signal needs a calibration process which involves scanning the wire across the beam and recording the sensor's signal against the wire position. In practice, the sensor is moved across the wire in order minimize vibrations.
Placing the wire in the thin section of the beam, close to the focal point offers higher sensitivity and less range, while operating on the larger sections of the beam offers greater range of wire oscillation at the expense of sensitivity. This is useful for tuning the sensor response for different magnetic field and oscillation magnitudes.

The measured photodiode output against wire position is shown in figure 23 which also indicates the detected transition points, the range of detectable wire position and corre-

sponding signal.

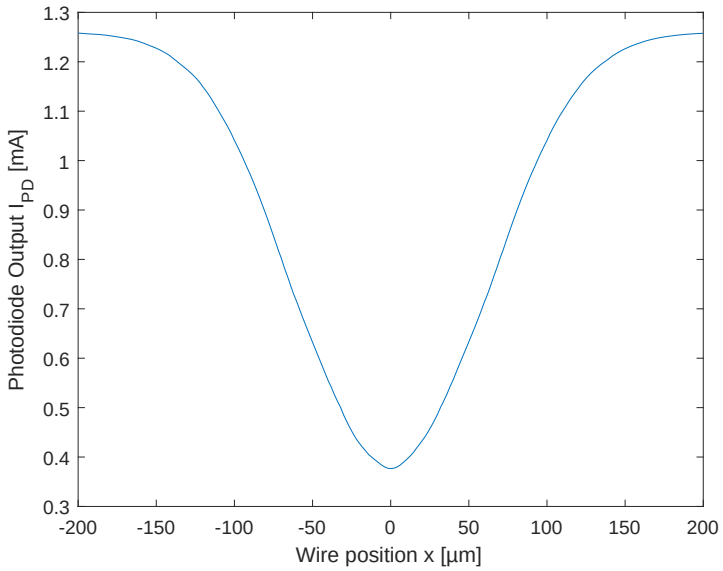

Figure 22: Simulated photodiode current as a function of wire position.

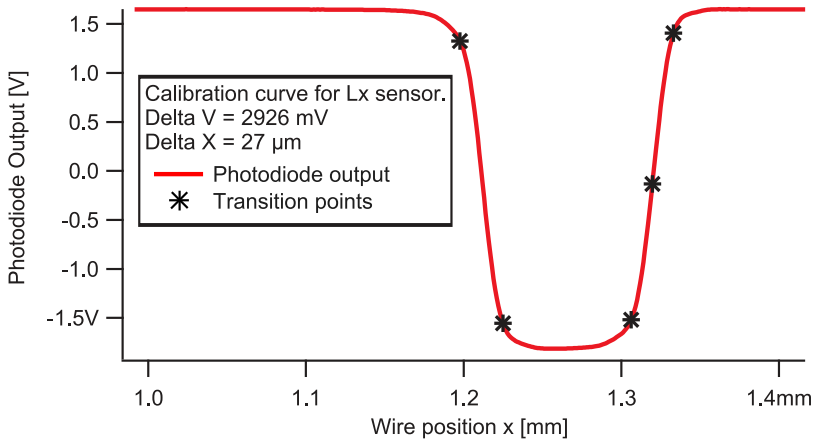

Figure 23: Measured photodiode output as a function of wire position.

The measured photodiode signal above is trimmed keeping only the rising edge and inverted to give the wire position as a function of signal. This is then fitted with a polynomial to be used as a transfer function $u(t) = P^n(V_{Photodiode}(t))$ which accounts for the non-linearity of the sensor's output. Figure 24 shows the measured and fitted transfer function as well as the difference between them (fit residual).

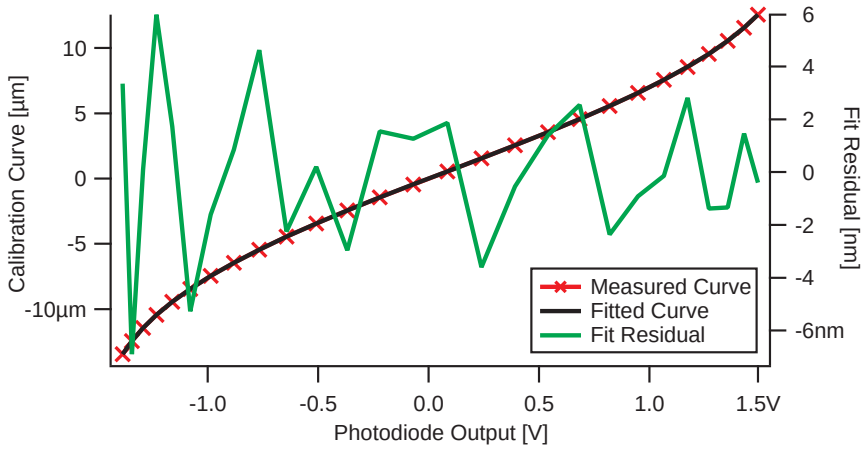

Figure 24: Measured and fitted wire position sensor transfer function.

The sensor's response to the wire position seen in figures 22 and 23 can be thought of as the result of convoluting the wire shape with the laser beam i.e. a convolution of a square function and a Gaussian distribution. Under this assumption, we can use the experimentally obtained response curve to calculate the laser beam shape and size.
This procedure can be repeated for various "setpoints" that intersect the laser beam at various longitudinal positions along the laser beam axis. The experimental results of such a scan showing the trade off between sensitivity and oscillation range of the unit sensor is shown in figure 25. The figure also shows the calculated laser beam profile for the same data set.

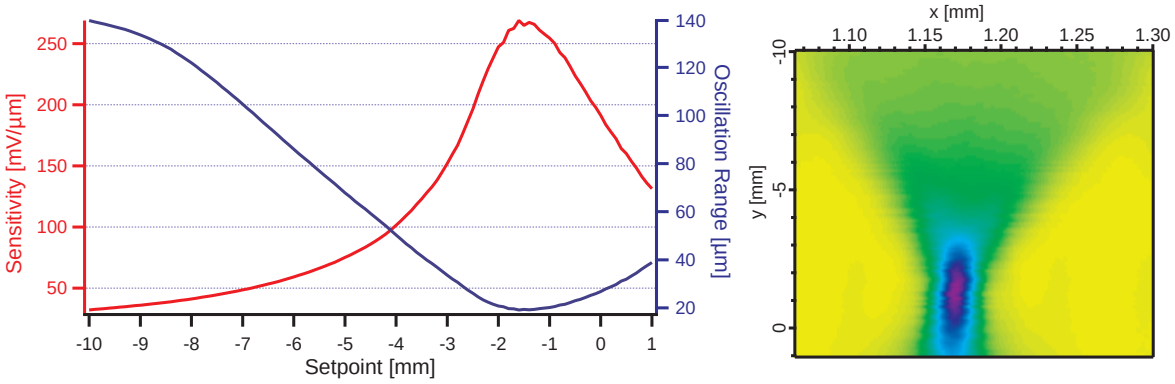

Figure 25: Measured sensor response against setpoint (left) and beam profile (right).

Figure 26 shows the actual photo of the wire oscillation sensor as built in MAX IV Laboratory where the laser spot is visible on the wire and on the iris.

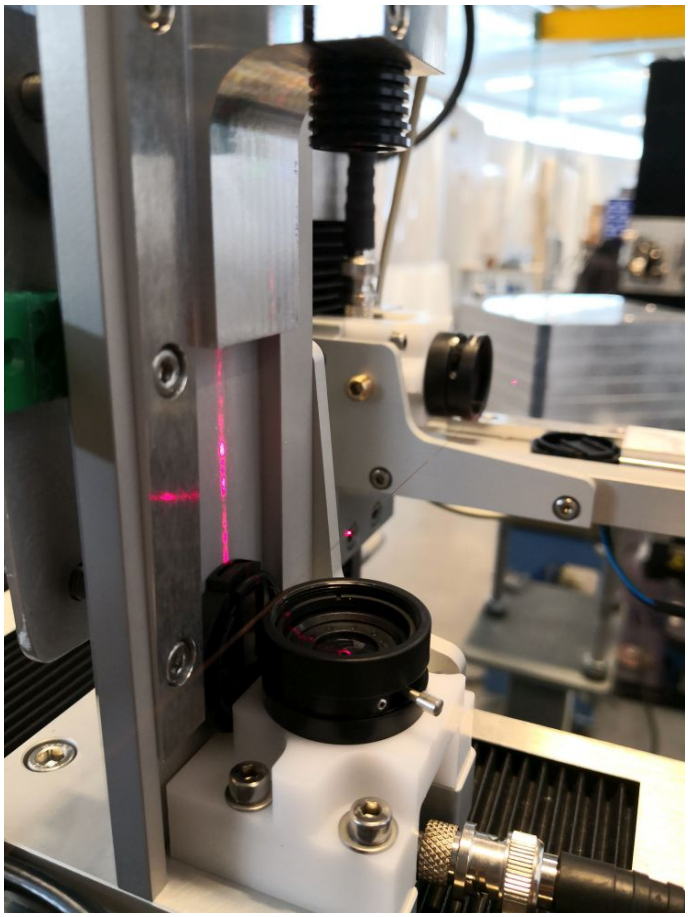

Figure 26: The sensing unit of the pulsed wire system at MAX IV Laboratory.

4.2 System Architecture

The system at MAX IV Laboratory was built as a combined Stretch Wire (SW) and Pulsed Wire (PW) system aimed primarily for Insertion Device characterization.
A tensioned wire is supported on two towers (A and B), where motorized stages can transverse the wire in the XY plane. A wire tensioner mechanism is placed on tower A, while a tension sensor is placed on tower B. These two towers are used for positioning the wire within an undulator as well as performing translations needed for the SW measurements. The two towers are shown in figure 27.

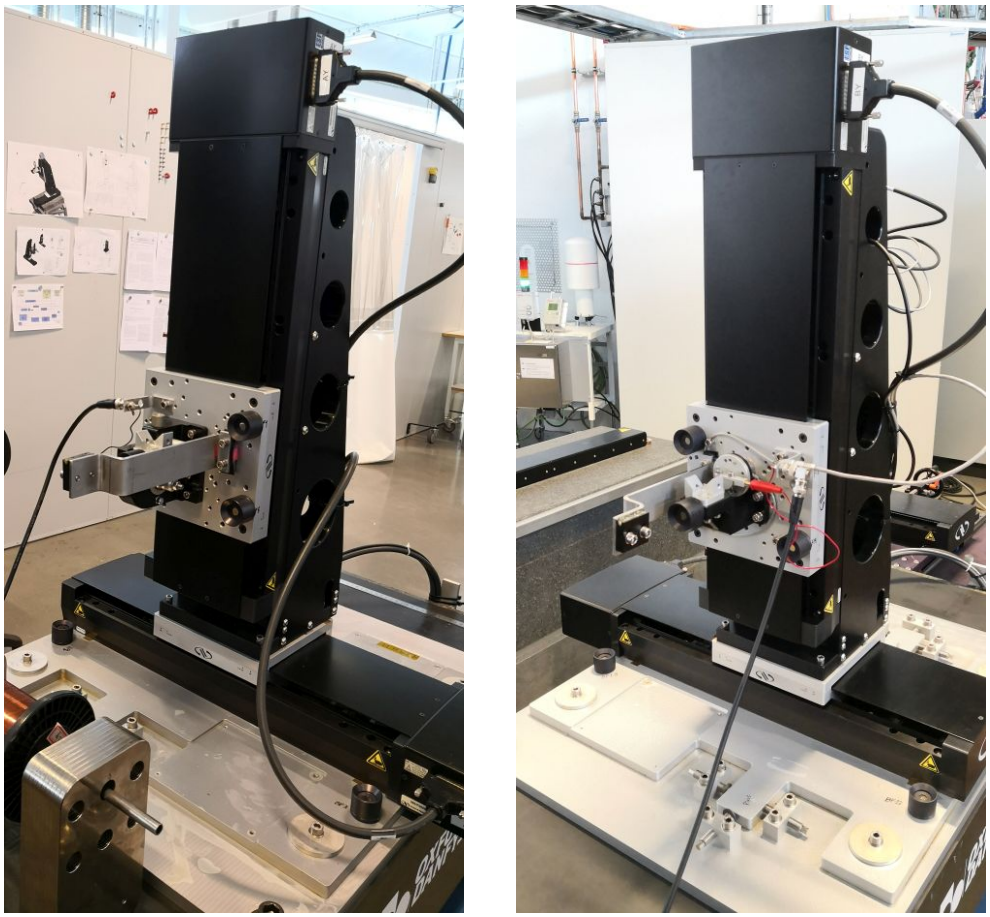

Figure 27: Towers A (left) and B (right) of the SW/PW system.

A third tower (tower C) supports the non-contact optical sensors of pulse wire oscillations, motorised XY stages maintain the sensor position over the wire when it moves. A Z stage moves the sensors longitudinally along the wire, and is used for the wave speed characterization procedure. Each optical sensor has a single independent smaller stage, which effectively allows for independent XY motion of each laser sensor when combined with the remaining stages. This tower is shown in figure 28.

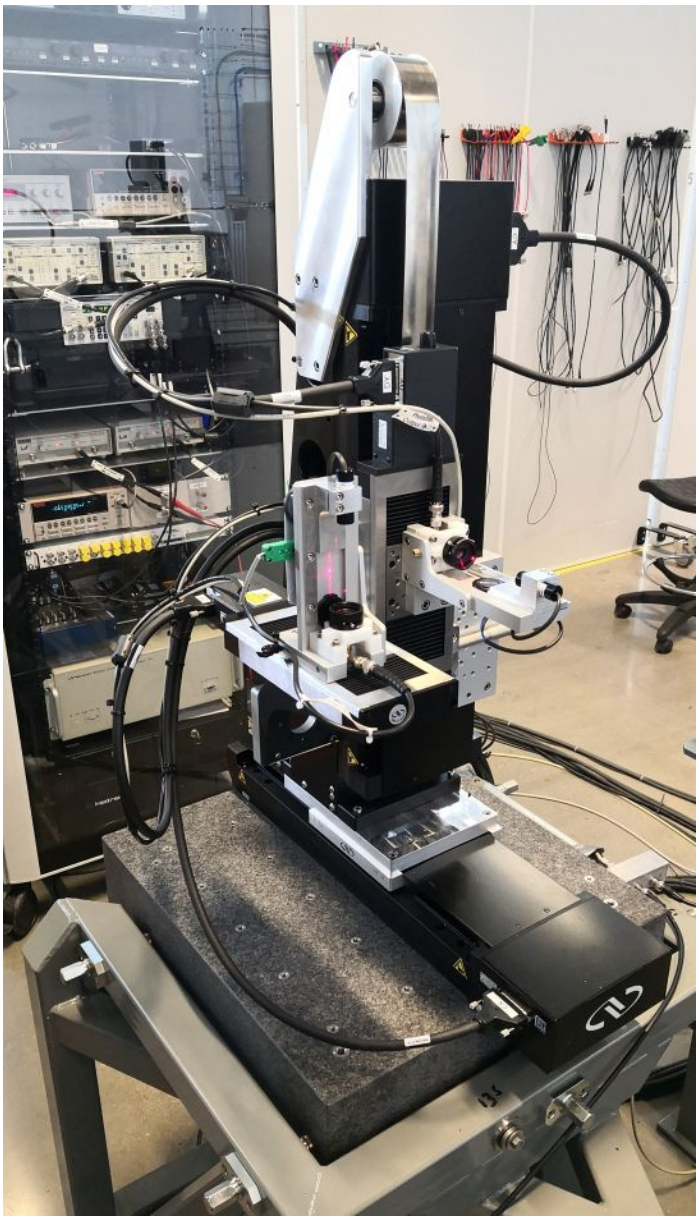

Figure 28: Tower C supporting the laser sensors of the PW system.

The following page illustrates the mentioned main components of the system and their inter-connections.

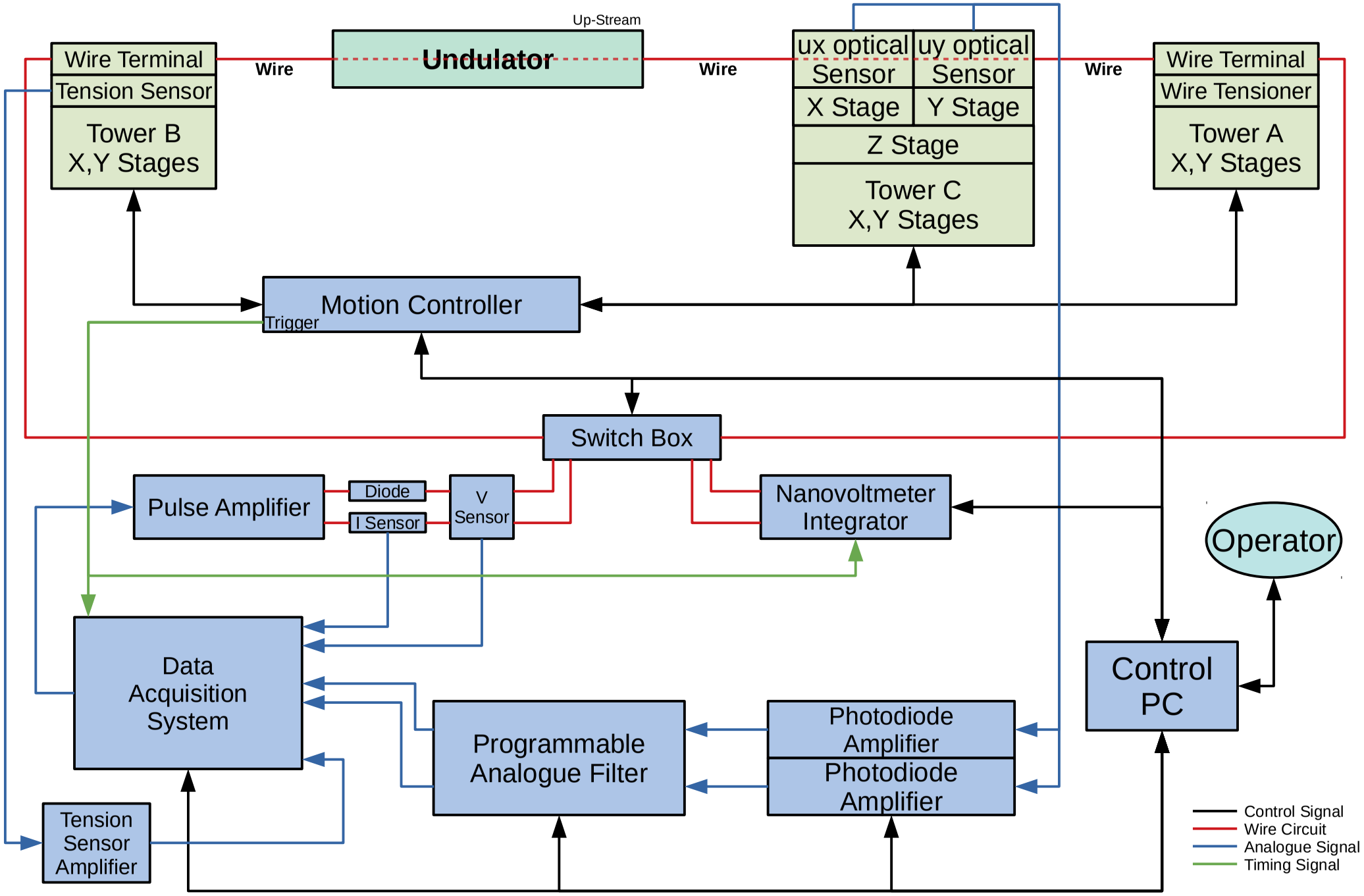
Up-Stream
Undulator
Wire Terminal
Tension Sensor
Tower B
X,Y Stages
Wire
Wire
ux optical
Sensor
uy optical
Sensor
X Stage
Y Stage
Z Stage
Tower C
X,Y Stages
Wire
Wire Terminal
Wire Tensioner
Tower A
X,Y Stages
Motion Controller
Trigger
Switch Box
Pulse Amplifier
Diode
I Sensor
V
Sensor
Nanovoltmeter
Integrator
Operator
Data
Acquisition
System
Control
PC
Programmable
Analogue Filter
Photodiode
Amplifier
Photodiode
Amplifier
Tension
Sensor
Amplifier
Control Signal
Wire Circuit
Analogue Signal
Timing Signal

All motion stages used are powered and controlled by a common motion controller, this allows precise position synchronization of all three towers as well as obtaining a position trigger pulse signal that can be used to synchronize other instruments to the position of any motion stage.

In order to facilitate the operation of the same wire under both measurement modes (PW and SW), a switch box is used to completely isolate the two independent signal paths. In SW mode, the wire is connected to a nano-voltmeter, which integrates the induced voltage of the moving wire.

In PW mode, a pulse profile is digitally generated and sent to the pulse amplifier which in turn is connected to the wire. The voltage and current profiles of the pulse are measured accurately and recorded.
The resulting wire oscillations are detected by the sensing photodiodes as a current signal, which gets conditioned by the photodiode amplifier and filtered (if necessary) by a programmable filter.
The data acquisition system is used to synchronously digitize the analogue signals as well as generate the required pulse profile.

The electronics used in the SW/PW system are installed in a single electrical cabinet as shown in figure 31. All equipment in the cabinet are grounded to a single common point using a star network to avoid forming ground loops that could interfere with the sensitive analogue signals.

The software layers used in this system are split into two main parts, Igor Pro is used for the equipment control, data acquisition and primary processing as well as error checking. The system operator is provided with a Graphical-User-Interface (GUI) that allows fine control over the system's parameters (figure 29) and execution of many predetermined procedures (figure 30). The raw measurement data can then be exported in files containing the wire oscillations, currents, voltages and other metadata.
The second layer consists of MatLab functions and scripts that can then import the raw data and further process the wire oscillation and current data to re-construct the magnetic fields, calculate the undulator parameters and compare against simulations and Hall-probe measurements if needed.

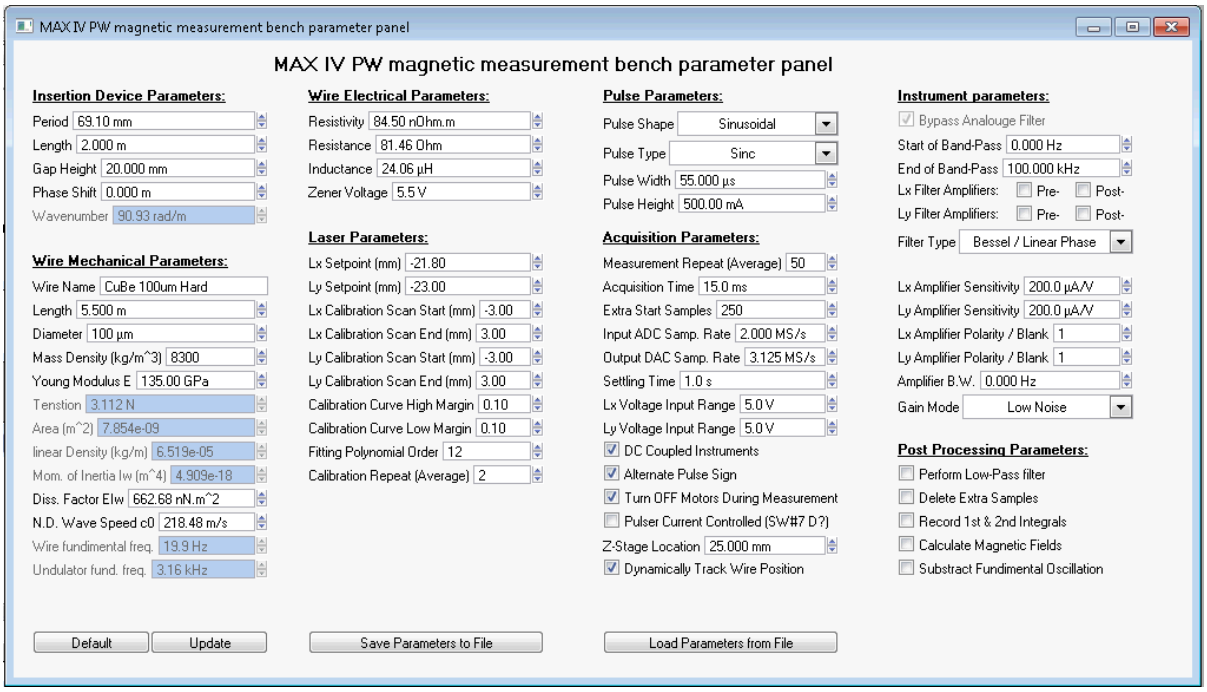

Figure 29: Pulsed wire system operator parameter GUI.

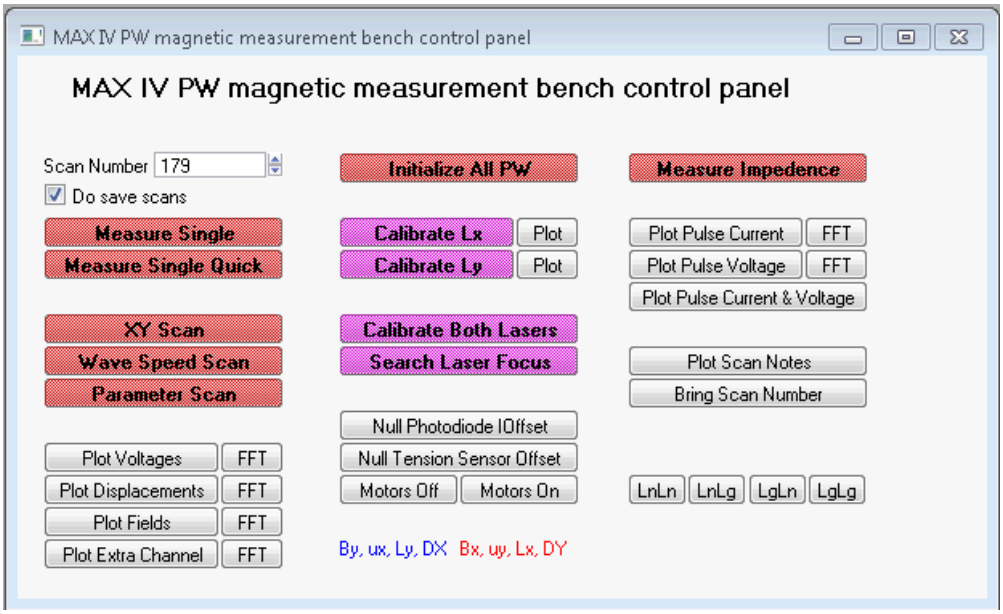

Figure 30: Pulsed wire system operator control GUI.

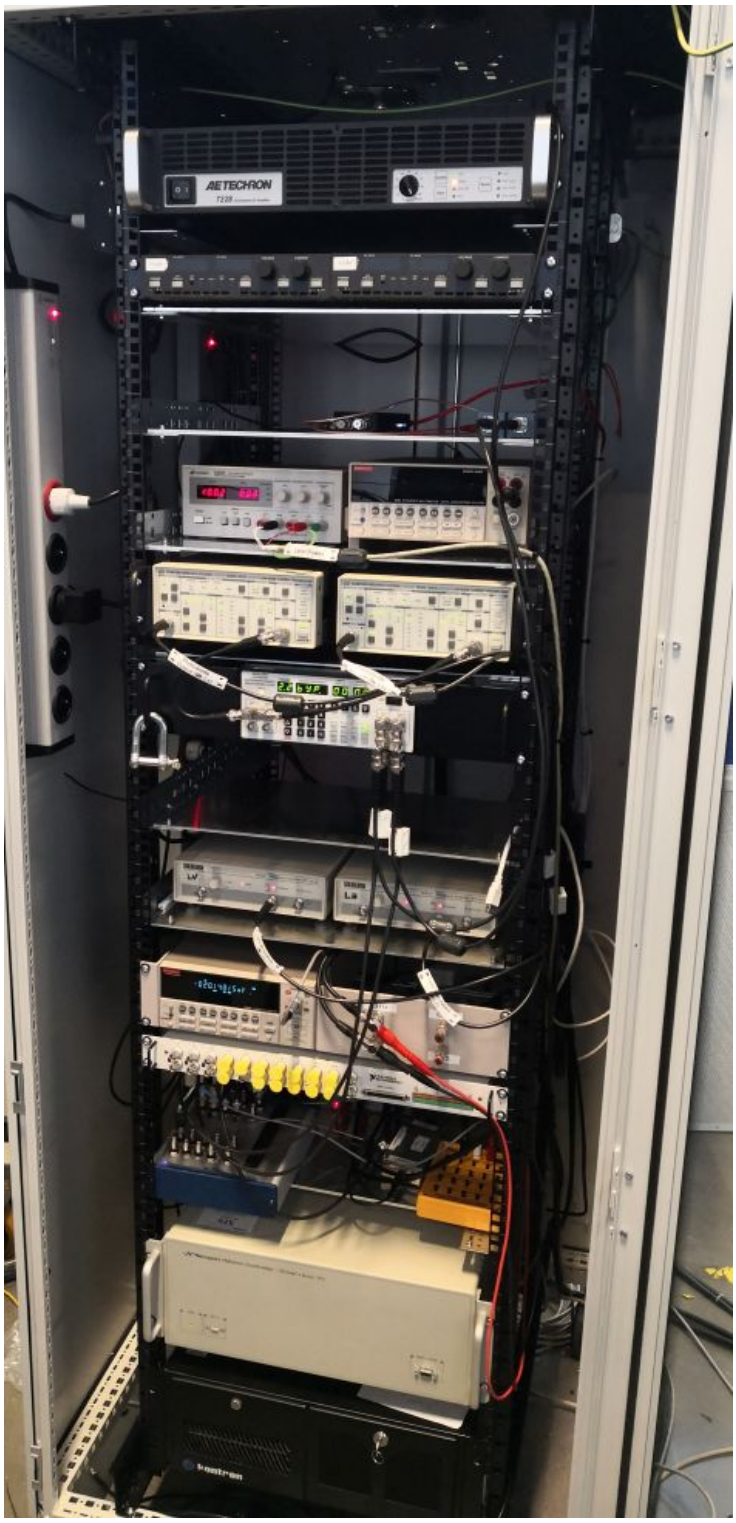

Figure 31: The electronic cabinet of the PW/SW system.

4.3 Wire Material Selection

The pulsed wire demands the use of a material with high strength and low mass density in order to reduce the wire sag, low resistivity is needed for passing sufficient current through and finally low stiffness is desired for reducing the dispersion effects.
The mentioned requirements are unfortunately conflicting and cannot all be optimized within a single material. Therefore a material search was conducted to find the best compromise.
A set of quantitative figures of merit were identified and used in the wire selection which are:
1- The achievable tension before breaking:

$$T = \frac{\pi \eta \sigma_y D^2}{4}$$

Where σ_y is the yield strength in Pa, η is a safety ratio set to 80% and D is the wire diameter set to $100\mu m$.
2- The achievable current through the wire:

$$I = \frac{V}{R} = \frac{\pi V D^2}{4 \rho_e L}$$

Where V is the available voltage set to $150V$, R is the wire resistance in Ω, ρ_e is the resistivity in $\Omega.m$ and L is the wire length set to $5.5m$.
3- The wire sag:

$$S = \frac{\pi \rho_m g L^2 D^2}{32T} = \frac{\rho_m g L^2}{8 \eta \sigma_y}$$

Where ρ_m is the volumetric mass density in $kg.m^{-3}$.
4- The dispersion factor:

$$DF = \frac{E I_w}{T} = \frac{E D^2}{16 \eta \sigma_y}$$

Where E is Young's modulus of elasticity in Pa.
5- The oscillation factor:

$$OF = \frac{I c_0}{2T} = \frac{I}{D\sqrt{\pi T \rho_m}}$$

Where c_0 is the non-disspersive wavespeed in $m.s^{-1}$.
A list of materials were investigated and the results are summarized in table 5.

Parameter	T $[N]$	I $[A]$	S $[mm]$	DF $[m^2]$	OF $[A.s.kg^{-1}]$
Cu	0.8	12.6	3.45	7.6e-7	866
CuBe	2.2	3.1	1.10	3.0e-7	128
CuCrZr	2.5	9.4	1.02	2.7e-7	358
CuNiSi	3.3	5.6	0.79	2.0e-7	185
TiAlV	5.2	0.15	0.25	1.0e-7	5.6
W	3.5	4.0	1.63	5.8e-7	88

Table 5: Summary of investigated wire materials.

We can see that copper (Cu) can pass high currents through, but it cannot be tensioned well, resulting is excessive sag and dispersion. Titanium alloy (TiAlV) on the other hand is light, and can be tensioned well, resulting is low sag and dispersion, but very little current can pass though the wire due to it's high resistivity, therefore producing very small oscillation amplitudes.
Copper-Beryllium (CuBe) is the classic material of choice in most of the literature, as it offers high strength and low resistivity. Tungsten (W) allows more current than CuBe at the cost of increased sag and dispersion, but will eventually create smaller oscillation amplitudes due to its high density.
Copper-Chromium-Zirconium (CuCrZr) and Copper-Nickel-Silicon (CuNiSi) seem better suited for PW application when compared to CuBe (classical choice). Therefore, these two materials were chosen to be used in the system.

4.4 Secondary Induced Currents

The concept of the PW measurement system is to pass an electric current in a wire that is located in a magnetic field to obtain a travelling wave along the wire. Nevertheless, according to Faraday's law of induction, a moving conductor in a magnetic field would induce an electric potential as well. In other words, every electric motor is also an electric generator. Moreover, the wire oscillations are matching in wavelength to the period length of the insertion device, resulting in efficient induction process (resonance).
Therefore, the induced potentials are unavoidable in this system. Figure 32 shows the circuit diagram including the source voltage Vs, source impedance (Rs and Ls), wire impedance (Rw and Lw) including the induced Electromotive Force potential (Vemf).
The current pulse source is in fact a voltage amplifier with a low output impedance. Immediately after the pulse, the voltage of Vs will collapse to 0V, this provides a low impedance path which allows the induced potential to circulate current in the circuit which distorts the traveling wave.
One solution to reduce the secondary induced currents is to add resistance to the circuit, this has the drawback of reducing the pulse current or require the use of much higher pulse voltage. Another solution is adding a switching element that cuts off the low impedance path at the end of the pulse. Due to the large difference between the pulse and induced

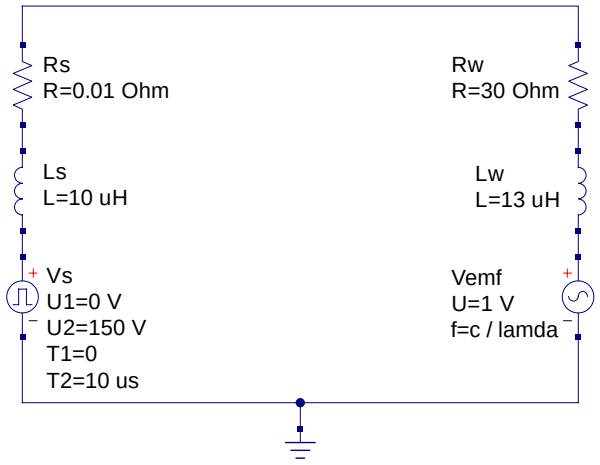

Figure 32: Circuit representation of the pulse source and wire.

voltage levels (150V and 1V respectively), this switching can be achieved using diodes as shown in figure 33.

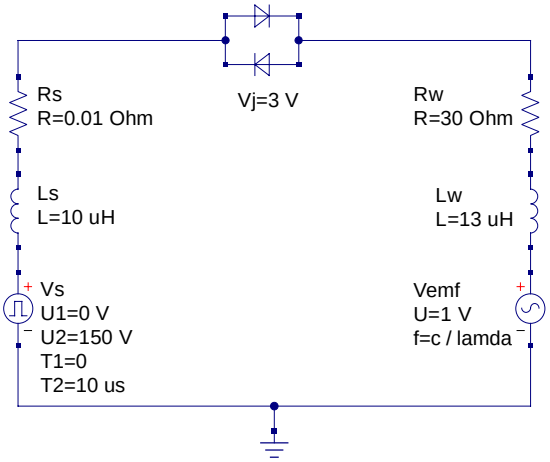

Figure 33: Circuit representation of the pulse source, wire and blocking diodes.

The diodes used have a junction voltage of 3V, this effectively forms a threshold where voltages below this level see a high impedance circuit, eliminating the induced current flow. Meanwhile the pulse voltage can easily overcome this threshold and drive the required pulse current through the circuit efficiently.
Figures 34 and 35 show the measured circuit voltage and current with and without the use of blocking diodes. It can be seen that the diodes block the flow of the induced currents effectively without noticeable reduction in the intended pulse current. Meanwhile the induced voltage seem to disappear without the diodes, this is not true, but rather is hidden due to the low source impedance compared to the wire impedance forming a voltage divider network.

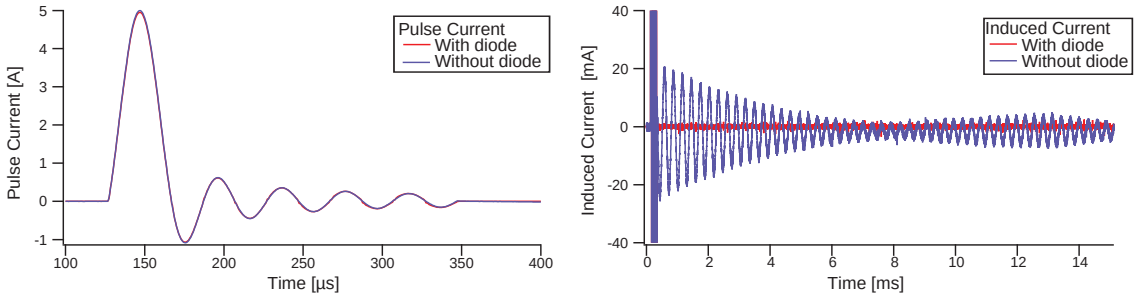

Figure 34: Diode effect on pulse current (left) and the induced currents (right).

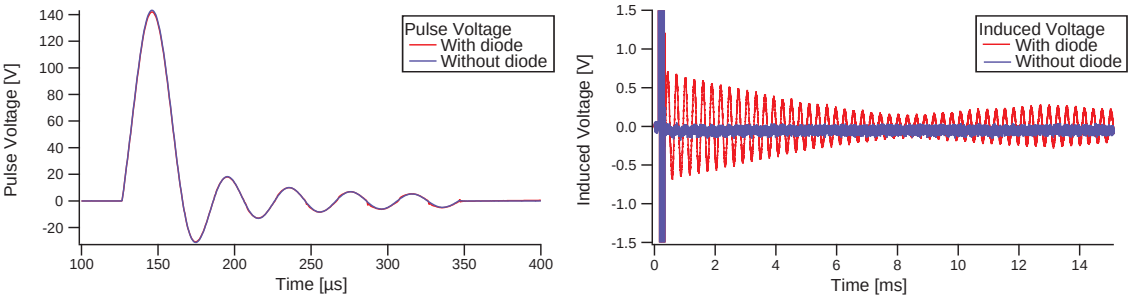

Figure 35: Diode effect on pulse voltage (left) and the induced voltage (right).

Finally figure 36 shows the effect of introducing the blocking diodes on the measured wire oscillations. The induced currents attenuate the oscillation amplitude due to energy transfer from the travelling wave to electrical current, while also inducing new oscillations after the end of the original wave.
The distortion makes it very difficult to obtain accurate magnetic field information from the pulsed wire signal even if the arbitrary pulse response method is applied, since now the governing equations of the wire oscillations need to be coupled to the induced potential and account for the energy loss and exchange in the circuit.

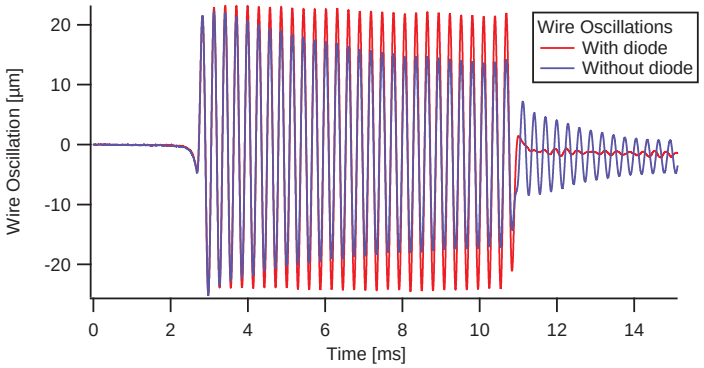

Figure 36: Diode effect on wire oscillations.

4.5 Background Vibrations

An absolutely static object is physically impossible to obtain, and the wire is no exception. In this context, any motion of the wire that occurs without sending a current pulse does not carry with it magnetic field information, and is considered a background oscillation. Three main sources of background oscillations has been identified in the PW setup at MAX IV Laboratory which are:

- Moving Air: Moving air from the ventilation system, people walking and air currents caused by the sun all contribute to very slow oscillations in the wire. These oscillations have a cycle time in seconds or tens of seconds. And can be isolated by covering the entire pulse wire system with a plastic wrap cover. The effect of this air cover is shown in the contrast between figures 37 and 38.
  Due to the slow nature of this type of oscillation, the pulsed wire system doesn't need to be covered during operation, but it is enough to include this oscillation in the range of motion the sensors can detect. Over the measurement time of $10-20ms$ this motion can be considered a static position shift that can be subtracted away as an offset by applying the initial condition $u(t=0)=0$.

- Motorized Stages: The wire is suspended on two XY towers (A and B), these towers contain motorized stages that work in closed PID loops. Therefore, the stages are constantly monitoring the position errors and correcting them, which adds to the background vibrations of the wire.
  Figure 39 shows the total background vibrations seen during an $8ms$ long scan, while figure 40 shows the background when the motors are switched off. It can be seen that the motors contribute to significant oscillations of frequency near $250Hz$. Therefore it is good practice to switch the motors off while obtaining the measurements.

- Wire eigenmode: The fundamental eigenmode of tensioned wire has the frequency of $f_1 = c_0/2L$. And this vibration has been found to be always present in the wire. Due to the fact that this oscillation has a very well defined frequency, it is possible to perform a curve fit of a sinusoidal function with this frequency and subtract it from the measured oscillations. The remaining vibrations after performing this operation is shown in figure 41 for an eigenfrequency of $38.5Hz$.

Figures 39, 40 and 41 were performed using a $5.5m$ long $200\mu m$ diameter TiAlV wire. The high resistivity of the material limits the pulse current to $0.5A$, resulting in very small oscillation amplitudes and therefore increased the effect of background oscillations.
The oscillations of this wire when pulsed within the test undulator is shown in figure 42 where the $\pm 300nm$ signal was averaged on 50 pulses resulting in noise of about $\pm 1nm$ which is equivalent to ± 5 titanium atoms.

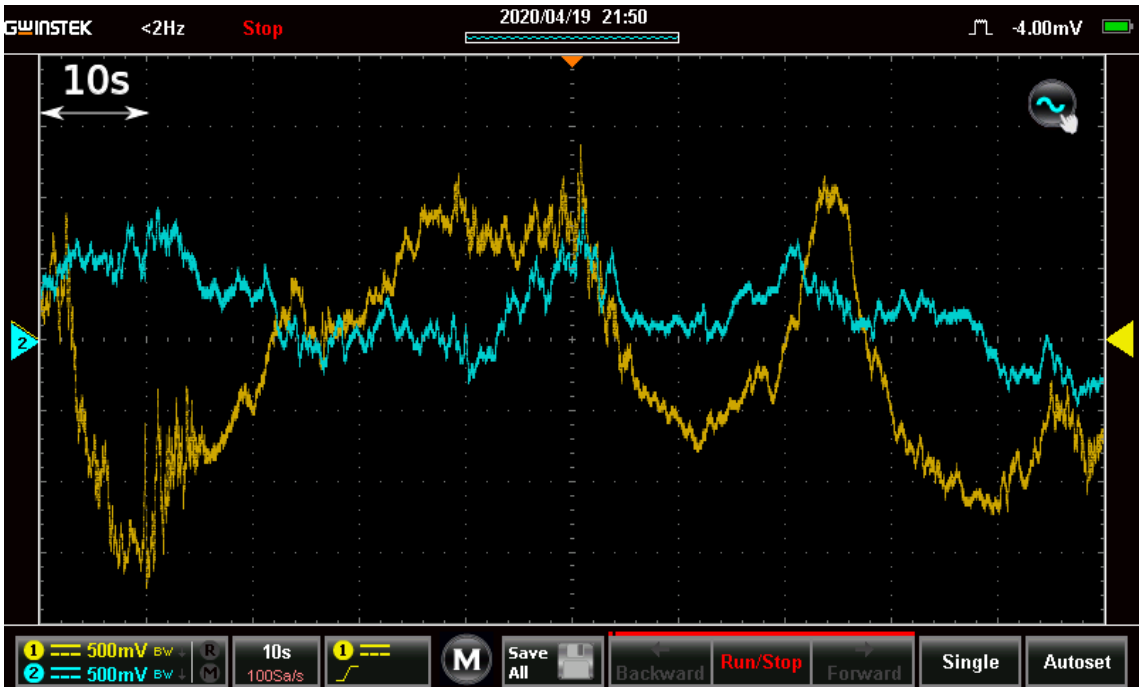

Figure 37: Slow background oscillations.

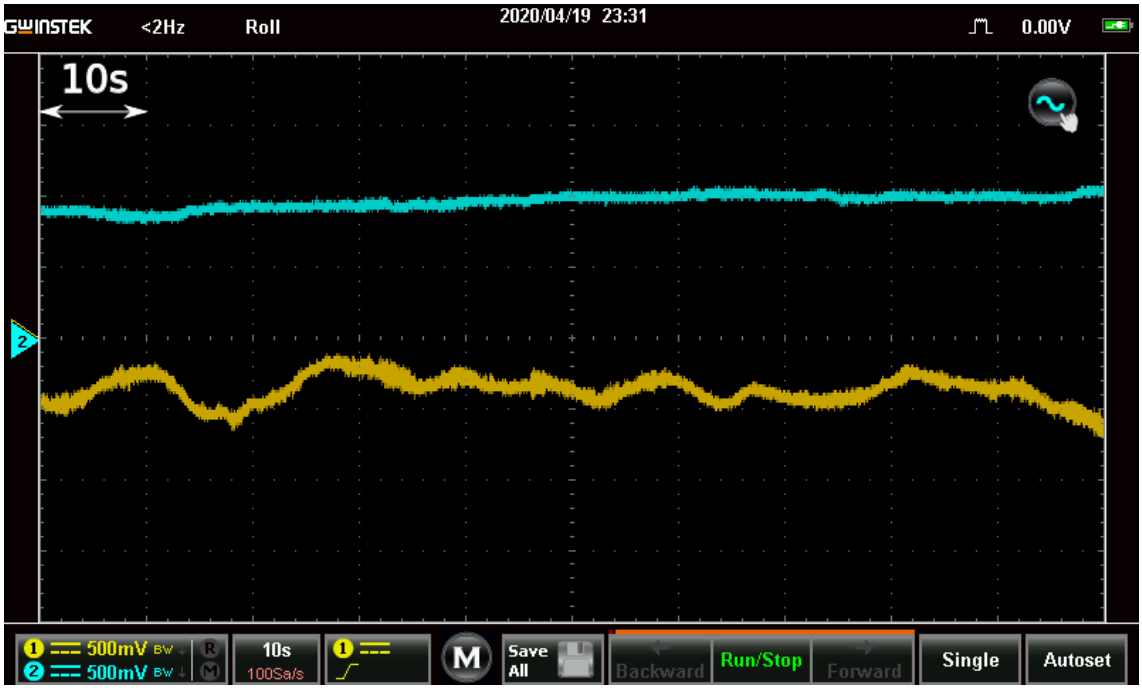

Figure 38: Slow background oscillations, with air cover.

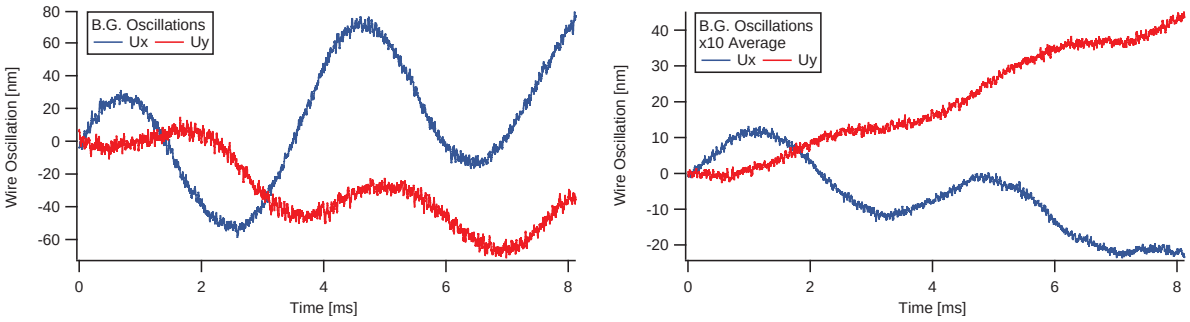

Figure 39: Fast Oscillations, 1 and 10x average.

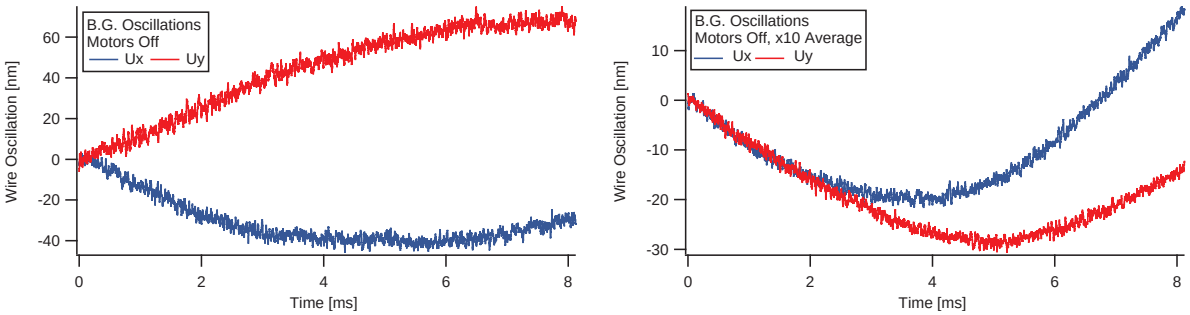

Figure 40: Fast Oscillations, Motors Off, 1 and 10x average.

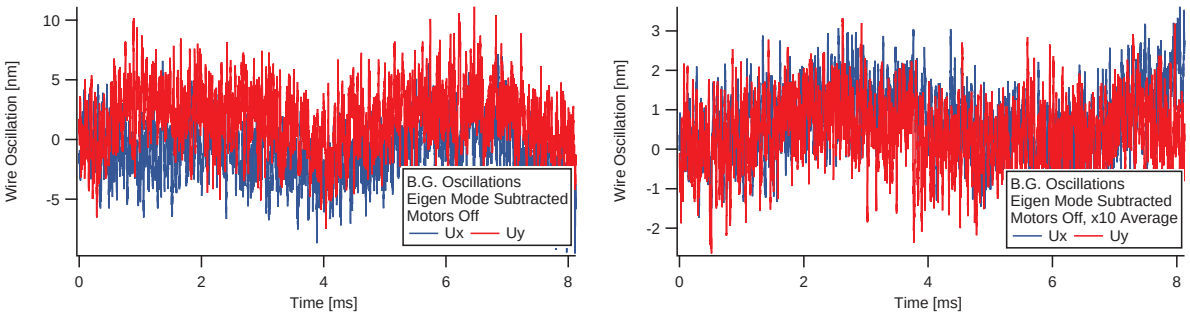

Figure 41: Fast Oscillations, Motors Off, Eigen Mode Removed, 1 and 10x average.

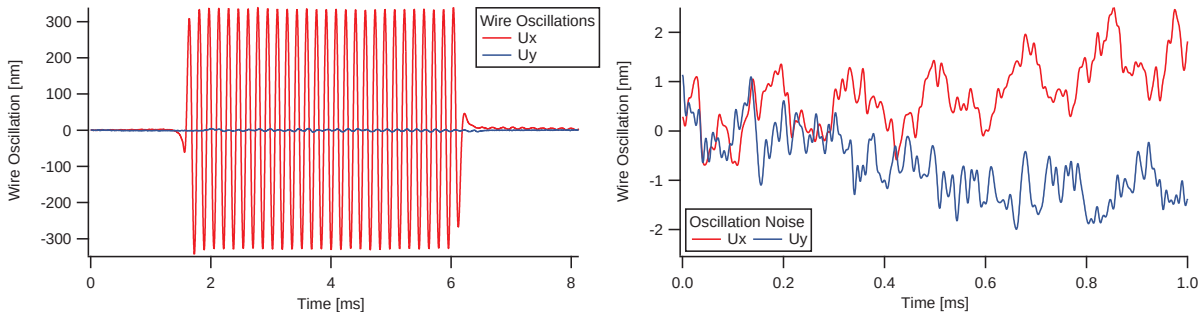

Figure 42: Wire oscillations for test undulator using $200\mu m$ TiAlV wire 50x average.

4.6 Electrical Noise

The pulsed wire system senses the wire oscillations and transmits a corresponding electrical signal in both analogue and digital forms as discussed in sections 4.1 and 4.2. Therefore, electrical noise is an unavoidable consequence of the analogue signal path. Electrical noise is any signal that is present while having the wire away from the laser sensor unit.
The first noise signal that was detected and addressed in the measurement system was the power network $50Hz$ and its odd harmonics. It was found that using a modulation ready laser source was very susceptible to this noise and this problem was solved when a continuous wave laser source was used instead. A frequency domain comparison between the two lasers is shown in figure 43.

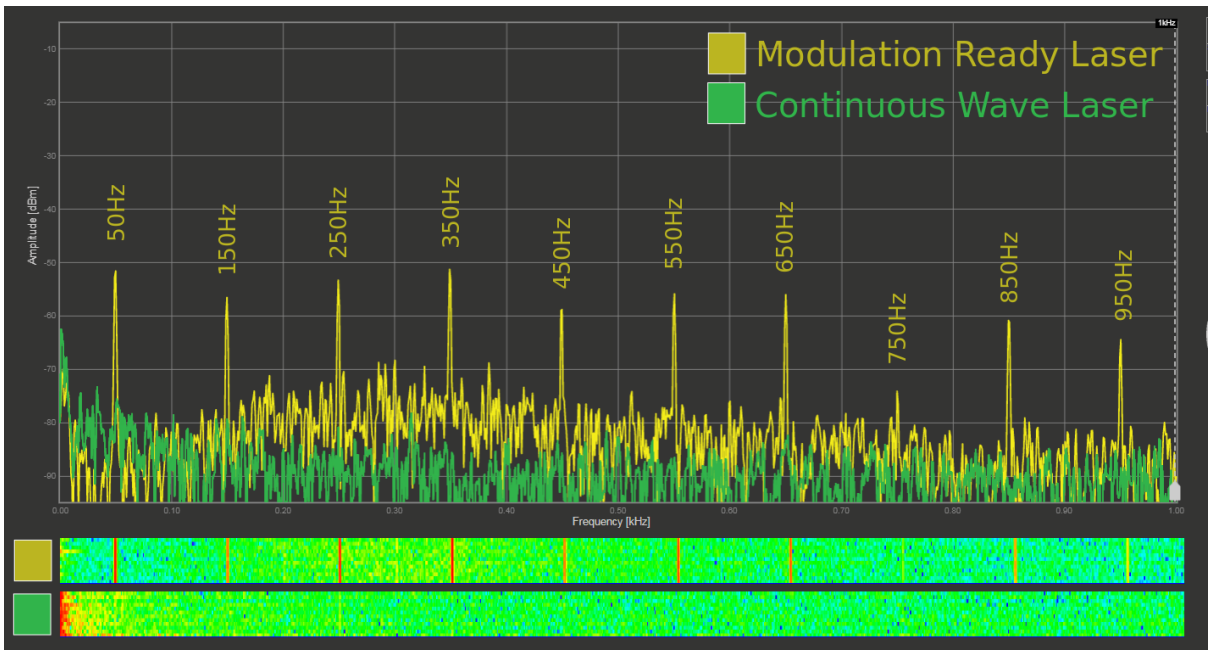

Figure 43: Spectrum analyzer comparison between modulation and continuous laser sources.

The simplified analogue signal path consists of the Laser source, Photodiode (PD), Photodiode Amplifier (Amp) and finally the Analogue-to-Digital Converter (ADC). In order to quantify the noise contribution of each component, the signal was artificially interrupted at each stage and then recorded using 1, 10 and 20x average. An example measurement is shown in figure 44 and the detailed results of the study is summarized in table 6.

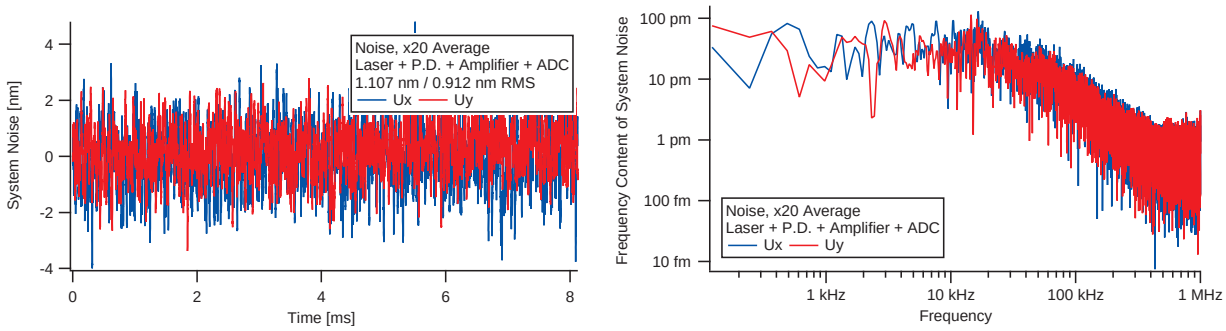

Figure 44: Electrical noise of the system using x20 Average in time and frequency domain.

Signal Components	RMS value of measured signal $[nm]$					
	x1 Average		x10 Average		x20 Average	
	u_x	u_y	u_x	u_y	u_x	u_y
Undulator Measurement	170.055	3.232	169.348	2.165	169.018	1.818
Laser + PD + Amp + ADC	5.158	3.938	1.691	1.358	1.107	0.912
PD + Amp + ADC	0.554	0.608	0.177	0.218	0.126	0.151
ADC	0.368	0.413	0.120	0.132	0.083	0.095

Table 6: Summary of electrical noise measurement experiment at various stages.

It can be seen from figure 44 that when using a 20x averages, the overall electrical noise contribution is fairly within a $\pm 4nm$ window. Also, the frequency analysis of the noise show no significant peaks indicating a white noise nature.
The noise contribution of each component was calculated separately from the above data set and is summarized in table 7.

Noise Source	RMS value of noise source $[nm]$					
	x1 Average		x10 Average		x20 Average	
	u_x	u_y	u_x	u_y	u_x	u_y
Laser	5.128	3.891	1.682	1.340	1.100	0.899
PD + Amp	0.414	0.446	0.130	0.173	0.095	0.117
ADC	0.368	0.413	0.120	0.132	0.083	0.095

Table 7: Breakdown of electrical noise contribution of each instrument.

The above treatment indicates that the laser source is the largest contributor to the overall electrical noise within the system built at MAX IV Laboratory, therefore a more stable laser source can be beneficial to reducing the overall system noise floor. This becomes increasingly important when using titanium wires as their high resistivity limits the pulse current amplitude resulting in small oscillations in the order of $\pm 300nm$ as in figure 42 and table 6, where the Signal to Noise Ratio (SNR) is $30.4dB$, $40.0dB$ and $43.7dB$ for x1, x10 and x20 averages respectively.

5 Measurement Results and Comparisons

The pulsed wire is a magnetic measurement device, that is built to replace the Hall-probe in obtaining local magnetic field information within limited access Insertion Devices.
In order to characterize the performance of the system, measurements were performed on an undulator that is previously known through Hall-probe measurements. The results of the two systems are compared, and any deviation from the Hall-probe results can be considered as errors of the pulsed wire measurement.

5.1 Wave Speed Measurement Results

The theory behind the wave speed measurement of a thin wire was discussed in section 3.5 and simulated in section 3.7.3, the purpose of which is to enable in-situ characterization of the wire parameters, namely, linear mass density (μ), tension (T) and flexural rigidity (EI_w). It was found that requesting the fit to obtain all three of these parameters can lead to inconsistent results. To overcome this, the linear mass density (μ) of the wire was measured independently by precisely cutting wire samples of different lengths and measuring their mass using a precision scale. The results of these measurements are shown in table 8.

Material	Diameter $[\mu m]$	Measured $[kg/m]$	σ $[kg/m]$	Catalog $[kg/m]$
CuCrZr	100	$7.22 \cdot 10^{-5}$	$1.7 \cdot 10^{-7}$	$6.98 \cdot 10^{-5}$
CuNiSi	100	$6.98 \cdot 10^{-5}$	$3.7 \cdot 10^{-8}$	$6.90 \cdot 10^{-5}$
TiAlV	200	$1.42 \cdot 10^{-4}$	$2.0 \cdot 10^{-7}$	$1.39 \cdot 10^{-4}$

Table 8: Measured linear mass density (μ) of available materials.

The wave speed measurement procedure relies on detecting the phase shift in time caused by a position shift in space. And due to dispersion, the wave speed will be dependent on its wavelength (frequency) and therefore, a pulse consisting of a wide frequency content is desirable. A short magnet of period $\lambda = 16mm$ was built and used for this purpose, the field of which is shown in figure 13. And the magnet is shown in figure 45.

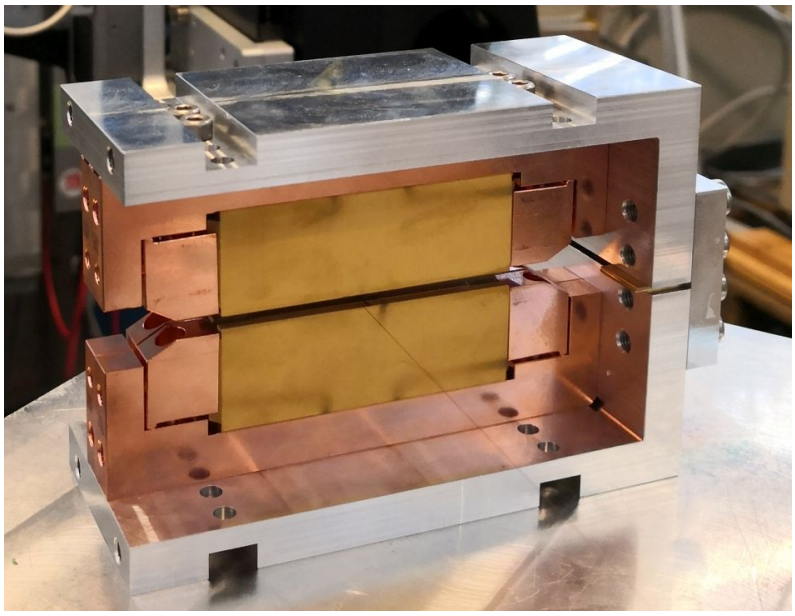

Figure 45: The short magnet used for wave speed measurement.

The wave speed measurement of the $100\mu m$ diameter CuCrZr wire is shown subsequently. Pulsed wire measurement was performed on 5 relative longitudinal displacement of the sensor unit, these measurements are shown in figure 46. From this, there were 15 possible pairs of measurements, where the relative phase difference of each pair was calculated as a function of frequency as shown in figure 47.

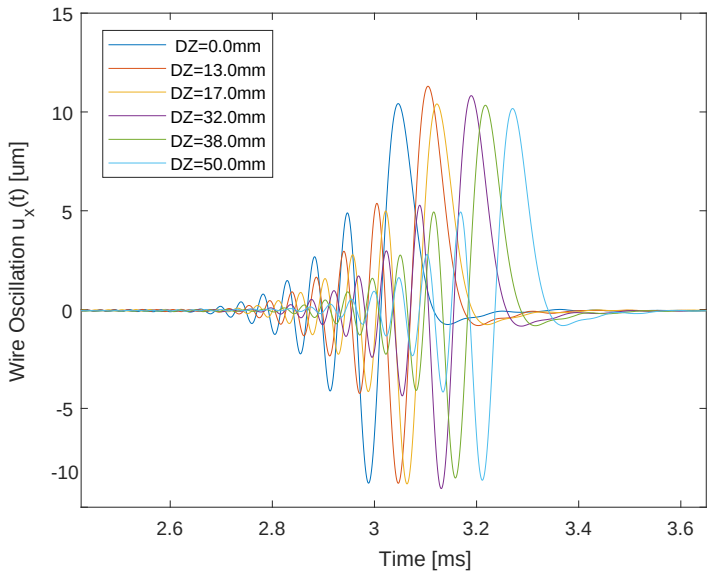

Figure 46: Wire oscillations obtained for wave speed measurement.

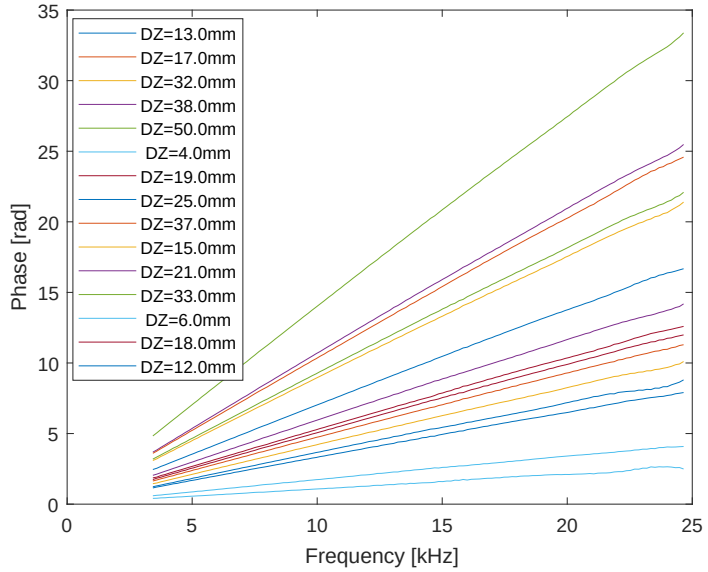

Figure 47: Phase evolution v.s. frequency for wave speed measurement.

The relative phase difference, relative displacements and linear mass density was used as input to fit the dispersion relation of an Euler-Bernoulli beam. The measured wave speeds and the fitted curve are shown in figure 48.

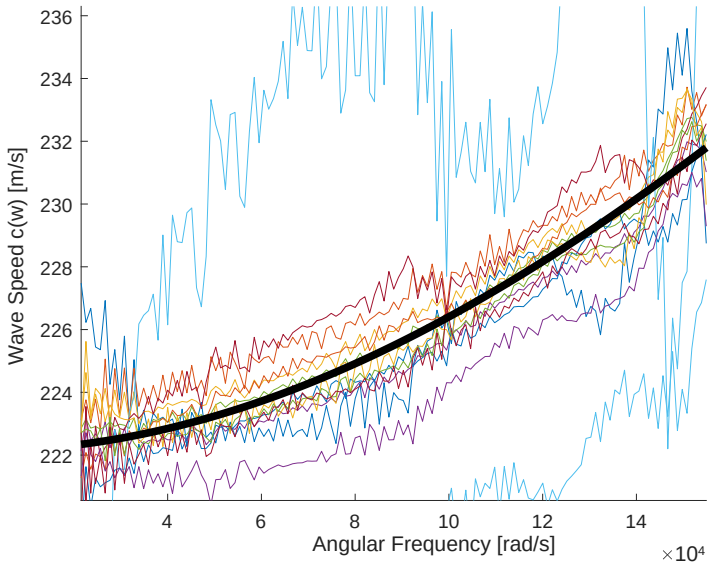

Figure 48: The measured and fitted wave speed.

This experiment was repeated 3 times in order to check if it yields consistent results, the

results from the fitting parameters are shown in table 9. Meanwhile, the obtained wire oscillations together with the fit results were used to re-construct the magnetic fields as shown in figure 49 which does resemble the magnetic field of this calibration magnet.

Measurement	T	EI_w
	$[N]$	$[N \cdot m^2]$
Take 1	3.572	$7.056 \cdot 10^{-7}$
Take 2	3.548	$7.061 \cdot 10^{-7}$
Take 3	3.564	$7.008 \cdot 10^{-7}$
Average	3.561	$7.042 \cdot 10^{-7}$
σ	0.012	$2.93 \cdot 10^{-9}$

Table 9: Measured flexural rigidity of CuCrZr wire 100 μm diameter.

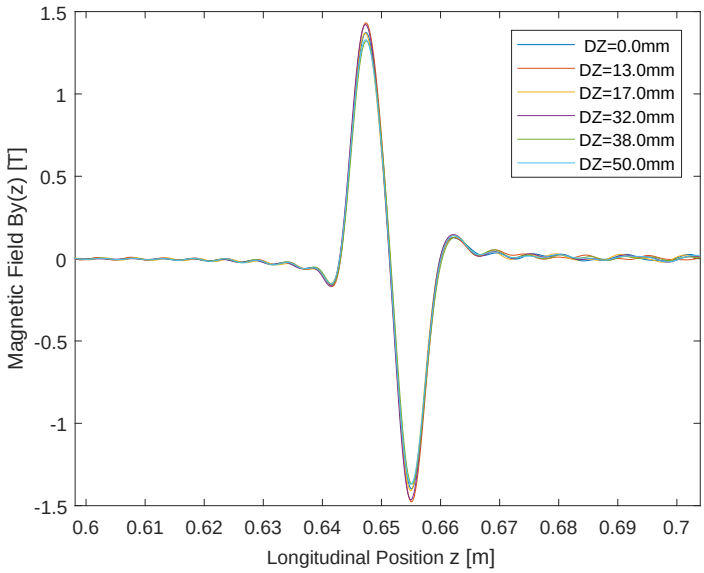

Figure 49: The reconstructed magnetic field of the wave speed measurement.

The same method for measuring the wave speed parameters was performed for 100μm diameter CuNiSi and for 200μm diameter TiAlV resulting in a flexural rigidity (EI_w) of $5.562 \cdot 10^{-7} N \cdot m^2$ and $7.919 \cdot 10^{-6} N \cdot m^2$, respectively.

5.2 Undulator Measurement Results

The ID laboratory at MAX IV offers a dedicated test undulator which was previously measured using the Hall probe mapper system and serves as a well known reference throughout the development of the pulsed wire measurement system. The main characteristics of this undulator are summarized in table 10.

Parameter	Value	Unit
Device Type	Elliptically Polarizing Undulator	
Magnet Type	Permanent Magnets	
Magnet Material	Nd-Fe-B	
Period Length λ_u	69.1	mm
Device Length L_u	2	m
Gap Movement Range	$18 - 280$	mm

Table 10: Properties of the large-period test undulator.

5.2.1 Measurement Setup

In this section, the test undulator was measured using the pulsed wire system and compared against the Hall-probe mapper data, the errors of the Hall-probe system are small enough for the purpose of this comparison and are therefore considered ideal representations of the undulator intrinsic errors. Before obtaining the measurements, the wire and the probe were placed in the magnetic mid-plane of the undulator by finding the minimum magnetic field (see equation 3.30). The measurements were taken for the undulator at gaps of $18, 20, 22, 30, 50, 75, 100$ and $150mm$.

For the experiment, a $100\mu m$ CuNiSi wire was tensioned to $4.3N$ and stretched between the towers at a distance of $5.5m$ apart, the undulator was placed between the sensors and the down-stream tower and extra wire was left up-stream of the sensor in-order to avoid contaminating the first wave pass with reflections.

Every shown PW measurement was repeated 5 times in-order to gain statistics, each one consists of 16 averaged pulses to reduce the noise level. Also, the motors were switched off during these measurements and the 1st and 2nd Eigenmodes of the wire were fitted and subtracted as discussed in section 4.5 and 4.6.

For the gap values between $18 - 75mm$ the pulse width used was $50\mu s$. And for gaps 100 and $150mm$ the pulse width was increased to $100\mu s$ in-order to obtain usable wave amplitudes. For gaps $18, 22, 30$ and $50mm$, the measurements were repeated using a much shorter $10\mu s$ pulse width to intentionally obtain lower oscillation amplitudes.

The laser sensor "setpoint" was tuned for each measurement to maximize the signal re-

sponse and include the required oscillation. The sensors were calibrated thereafter as described in section 4.1.

The arbitrary pulse response treatment described in section 3.4 was used throughout for obtaining the magnetic field data from the wire oscillation. The pulse was $sinc(t)$ shaped peaking at $3A$ and was measured and used in the data treatment. The dispersion wave-speed model of section 3.2 was applied and the in-situ measured wire constants of section 5.1 were used.

The sag correction method described in section 3.6 was applied to the magnetic field data, even though the correction factor was negligibly close to 1. This is due to the large period length of the undulator and the relatively high tension level used.

5.2.2 Measured Wire Oscillations

The obtained wire oscillation amplitude for the measurement set is shown in figure 50. The x (horizontal) oscillation amplitude is highest at minimum undulator gap since the y (vertical) magnetic field is strongest. A measurement set with intentionally lowered oscillation amplitude was obtained as well, and serves to crudely check if any non-linearity is present in the system.
At $18mm$ ID gap, the oscillation amplitude is $16\mu m$ peak or $12\mu m$ RMS. The obtained oscillations are shown in figure 51. It can be seen that a "wake" is present after the passage of undulator wave. This was consistently observed in all PW measurements performed.

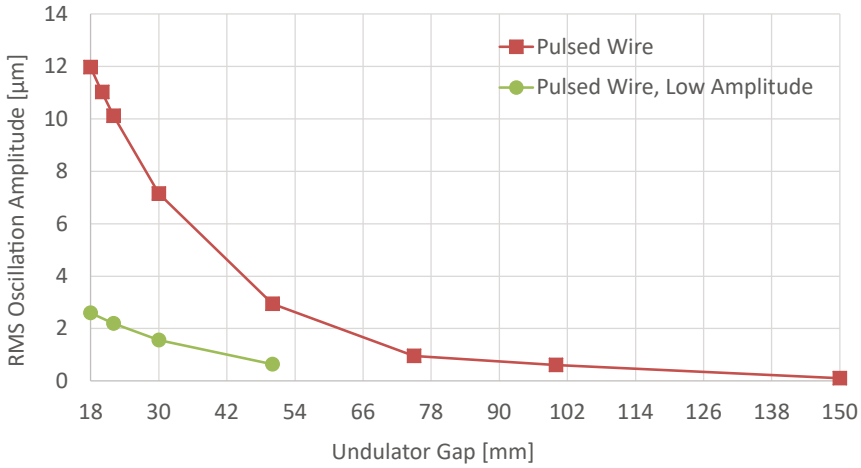

Figure 50: Measured wire oscillation amplitudes for the different undulator gaps.

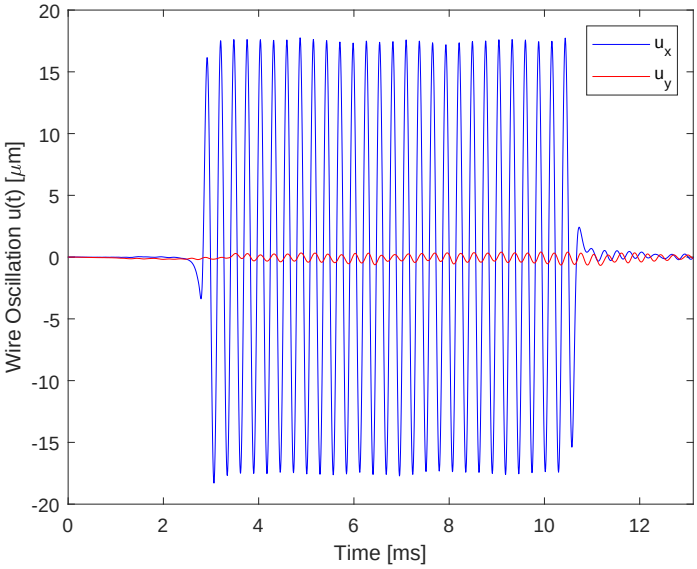

Figure 51: Example of measured oscillation data at 18mm undulator gap.

5.2.3 Measured Effective Field

The effective magnetic field is a measure of the "strength" of an undulator, it is directly used in calculating the deflection parameter (K-value) (see section B.1) which determines the wavelength of the emitted X-rays.
An example of the obtained magnetic field from the wire oscillations at $18mm$ gap compared to that of the HP system is shown in figure 52. Here the "wake waves" seen earlier in figure 51 create a fictitious periodic magnetic field behind the undulator.

Next we compare the Effective Magnetic Field (B_{eff}), including only the 3^{rd} and 5^{th} magnetic field harmonics that are present in the undulator. The magnitude of B_{eff} is compared between the HP and the PW is shown in figure 53, the relative difference between the two systems ($\Delta B_{eff}/B_{eff}$) is shown in figure 54 and the normalized standard deviation of the PW measurement ($\sigma_{B_{eff}}/B_{eff}$) is shown in figure 55.

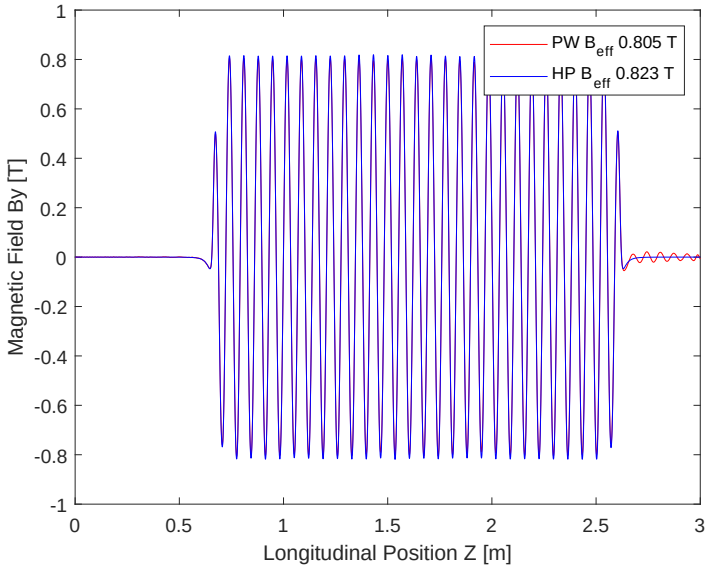

Figure 52: Example of measured magnetic field of the PW and HP systems.

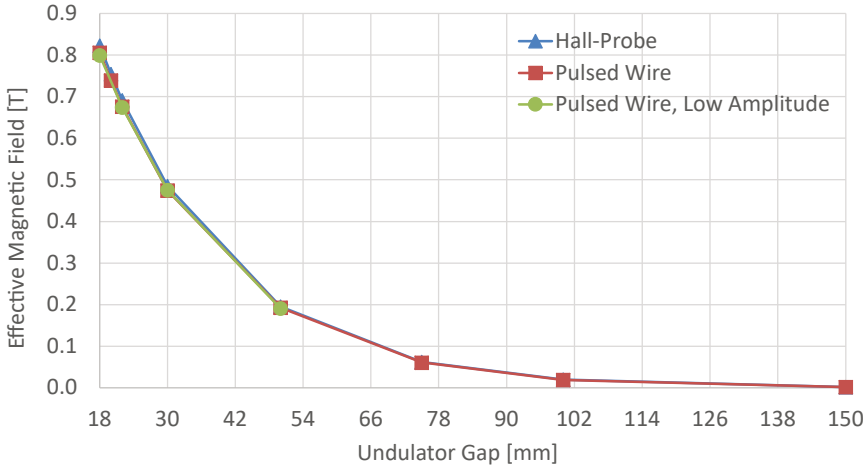

Figure 53: Measured HP and PW Effective Magnetic Field.

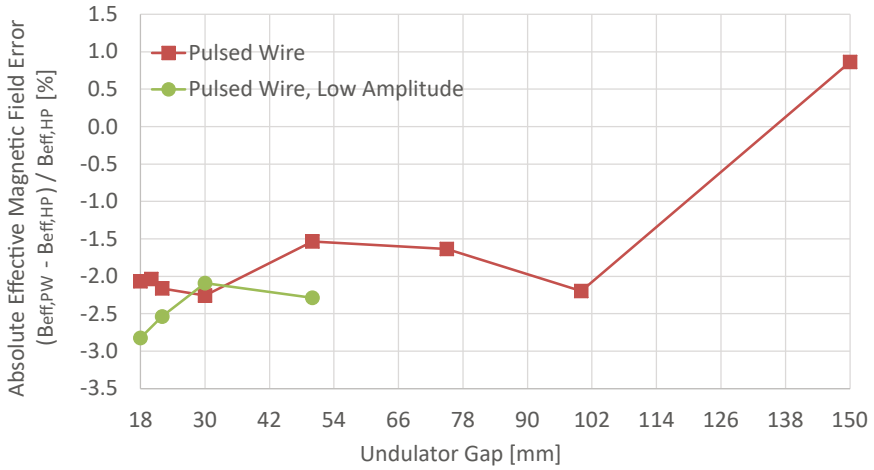

Figure 54: Relative Difference in Measured HP and PW Effective Magnetic Field.

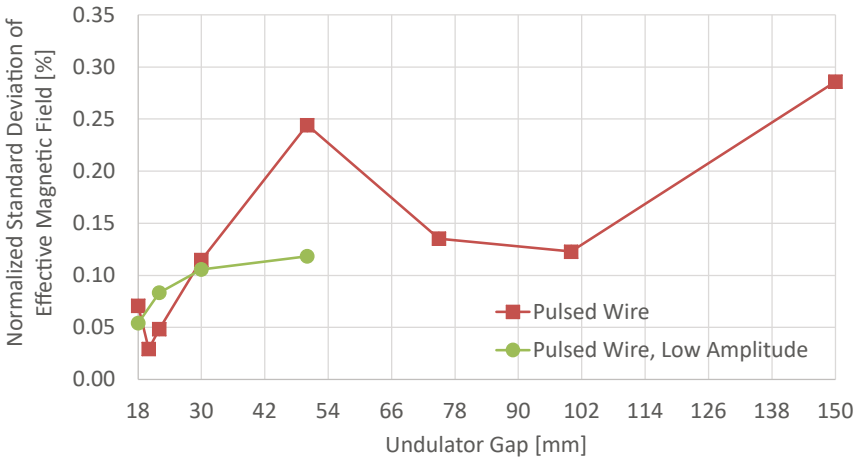

Figure 55: Normalized Standard Deviation of PW Measured Effective Magnetic Field.

The relative difference ($\Delta B_{eff}/B_{eff}$) serves to quantify the accuracy of the B_{eff} measurement value which arises from systematic errors of the PW system, these errors can be caused by the calibration of the pulse current sensor, the oscillation sensor transfer function, frequency-dependent gain of electronics or wire constant parameters such as tension, flexural rigidity, and linear mass density.
If we neglect the error seen at $150mm$ gap where the oscillation amplitude is low, the value of the error ranges between -1.5% and -3.0%. This means that there is a -2.25% constant error which could be calibrated away, improving the systematic error range of B_{eff} measurement to $\pm 0.75\%$. Where the Hall-probe sensor has an absolute accuracy of $\pm 0.25\%$.

The normalized standard deviation ($\sigma_{B_{eff}}/B_{eff}$) describes the precision of the B_{eff} mea-

surement which arises from random error source within the PW system such as background vibrations, air movement, electrical and optical noise, temperature variations and Eigenmodes of the wire and support structures.
Generally, random errors can be minimized by averaging multiple repeated measurements, but the reduction is inversely proportional to the square-root of the number of measurements ($\propto 1/\sqrt{N}$). This means that improving the standard deviation by tenfold using averaging alone requires a hundredfold increase in number of averaged measurements. Therefore, determining the sources of random errors and reducing their effects can be a more time-effective method to improve the system's precision.
And so, within this setup of the pulsed wire experiment, the precision of the B_{eff} measurement can be said to be 0.15%, this is two orders of magnitude more than the Hall-probe mapper figure of 0.0016% due to the reduced HP system complexity, the ultra-low noise figure of the sensor, trajectory flatness and low vibration levels.

5.2.4 Measured Integrated Fields

The integrated magnetic field within an undulator as described in section B.2 can be calculated from the measured PW and HP local magnetic fields. In both cases, the integrated magnetic field is sensitive to non-linearity of the measurement system, and are therefore always corrected using an external induction based integral measurement system, the Flip Coil in this case which is described in section C.2.1.

The first magnetic field integral is proportional to the angle of the electron trajectory when travelling through an undulator. An example of the measured first integral using the HP and PW system is shown in figure 56 for the test undulator at gap $18mm$.

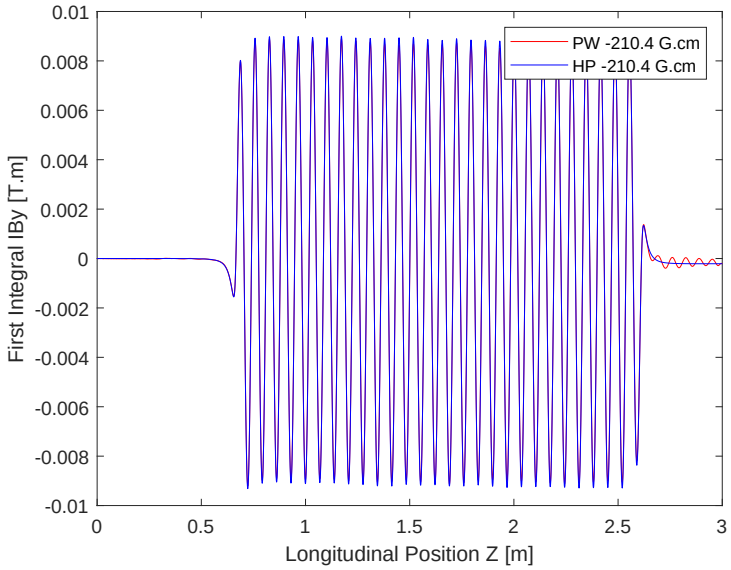

Figure 56: Measured HP and PW First Magnetic Field Integral.

The second magnetic field integral is proportional to the electron trajectory path when travelling through an undulator. And a comparison between the HP and PW in measuring the second field integral is shown in figure 57 for the test undulator at gap $18mm$.

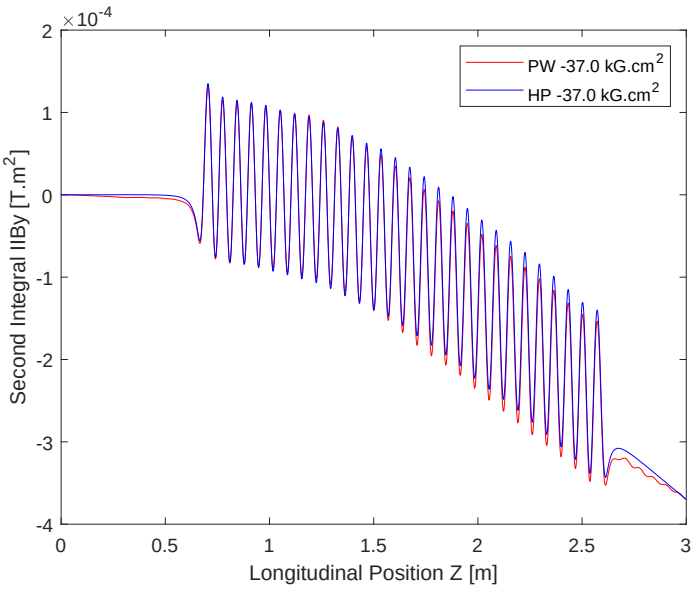

Figure 57: Measured HP and PW Second Magnetic Field Integral.

5.2.5 Measured Magnetic Pole Fields

As an undulator is built up of a series of alternating magnetic elements repeating periodically, the strength of the magnetic field in each half-period is referred to the as the "pole peak field" or "pole field" ($B_p = B(Z_p)$). Where the location of the pole within the undulator is referred to as "pole position" (Z_p).
This figure is useful during the tuning process of an undulator to help determine which magnetic block to adjust within the array. Deviations of the pole fields lead to changes in the integral values, the RMS phase error values and the effective magnetic field.

For example, making a single pole stronger mainly causes a first and second integral deviation, increasing the strength of a another subsequent and opposite polarity pole cancels out the first integral deviation and maintains the second. Similarly, increasing the strength of two adjacent poles would mainly effect the phase error at that location.

The magnetic field of the poles within the test undulator is compared at $18mm$ gap between the HP and PW measurements and is shown in figure 58. And the position deviation between two adjacent poles is compared in figure 59.

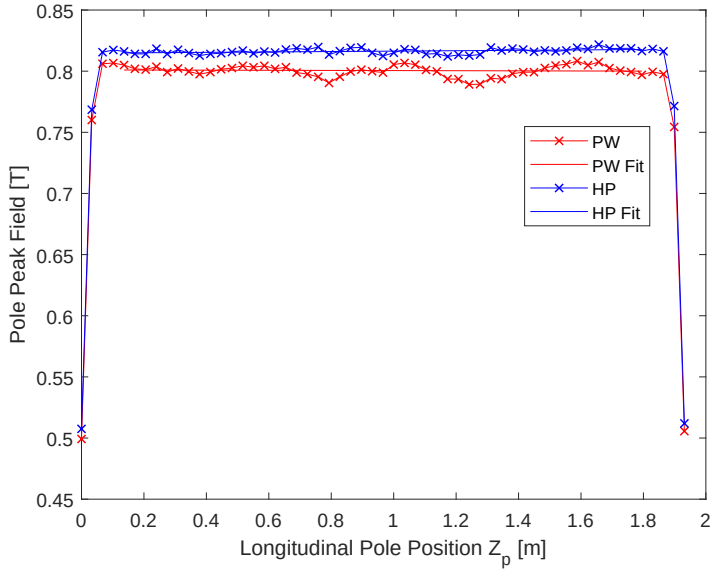

Figure 58: Measured HP and PW Pole Magnetic Field.

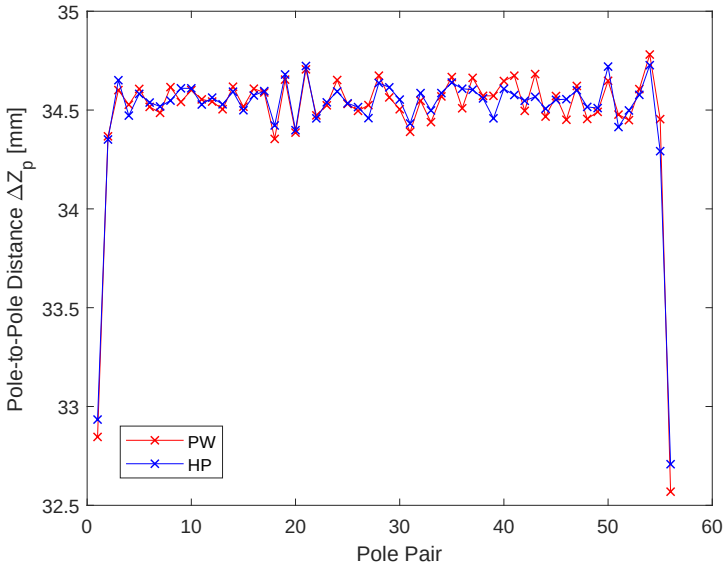

Figure 59: Measured HP and PW Pole Position Deviation.

From figure 59 we can see that the positioning of the pole location is fairly well matched between the HP and PW systems, and is representative of the pole positioning error of the test undulator itself.
Meanwhile, figure 58 shows a reduction in the overall pole strength as measured by the PW system, which is related to the reduction in the effective magnetic field discussed in

section 5.2.3.

More importantly, an oscillation in the pole magnetic field is seen in the pulsed wire measurements, this cannot be explained by a constant calibration problem but is rather a dynamic process that occurs during the measurement time. This deviation was also found to be repeatable with every measurement, and therefore cannot be explained by random errors either.
Consequently, a systematic dynamic behavior of the PW system must be responsible for this behavior. To further investigate this, two quantities were compared:
First, the difference between the pole fields measured using the PW and the undulator -as measured using the HP, removing any static difference, $(B_{p,PW} - B_{p,HP})/B_{p,HP}$.
Second, the difference between the measured wire oscillation and the simulated wire oscillation (using the measured pulse current and the HP field data), removing any static ratio difference. $(u_{PW,Measured} - u_{PW,Simulated})/Amplitude(u_{PW,Simulated})$.
These two quantities were plotted together in time domain and shown in figure 60.

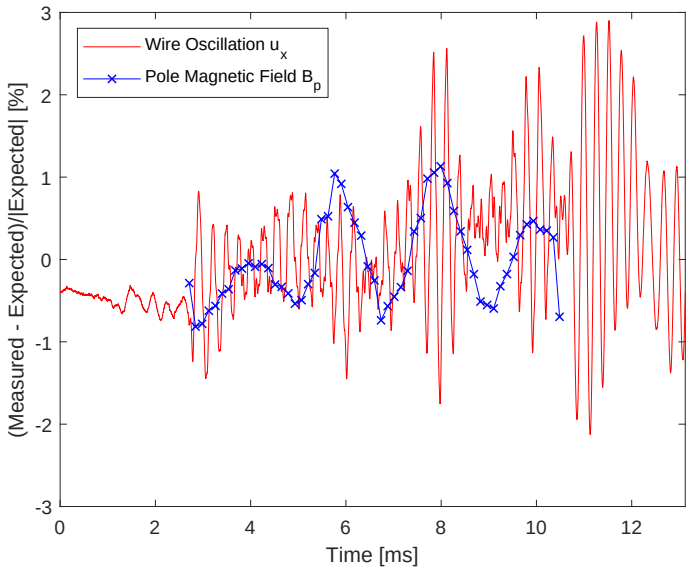

Figure 60: Normalized PW pole strength deviation against wire oscillation deviation.

It can be clearly seen from figure 60 that an amplitude modulated oscillation of the wire occurs and that it correlates to the observed deviation of the magnetic poles.
Moreover, this modulation seems to increase with time, and extend beyond the passage of the undulator wave, as seen present in the trailing end of figures 51 and 52.
This modulated oscillation is not predicted by the model used in section 3.2 since it doesn't appear in the simulations that use this model, nor is it accounted for when calculating the magnetic field out of the measured wire oscillations.

Next, in order to understand the development of this modulation effect, I calculate the standard deviation of the pole fields that results from both the PW and HP system, and isolate the contribution of the PW system using the quantity:
Standard Deviation Error of Pole Magnetic Field $\sigma_{B_{p,err}} = \sqrt{\sigma^2_{B_{p,PW}} - \sigma^2_{B_{p,HP}}}$.
Which is then normalized by the effective field magnitude $\sigma_{B_{p,err}}/B_{eff}$, and plotted in figure 61.

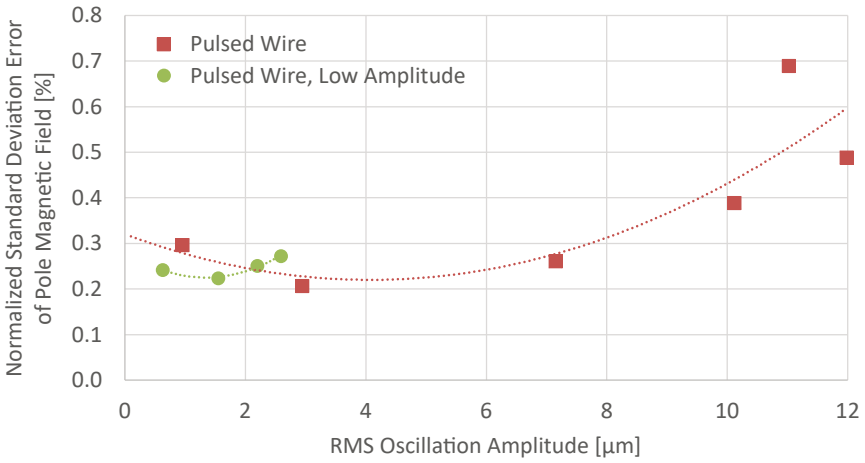

Figure 61: Error in pole magnetic field against wire oscillation amplitude.

In figure 61, we can clearly see the effect of the oscillation amplitude on the pole field measured error, which is the result of the modulated component of the wire oscillations. The wire modulation effect seem to grow non-linearly with the oscillation amplitude.

5.2.6 Measured Phase Error

The phase error as defined in the section B.3 is calculated by integrating the square of the first integral of the magnetic field. Therefore, it is an accumulative quantity of all errors within the undulator.
It will then come as no surprise that the effect of the modulation in the wire oscillation (and therefore in the pole field) would have an impact on the measured phase error quantity.
An example of the calculated phase error for the undulator gap at $18mm$ is shown in figure 62, showing large deviations.

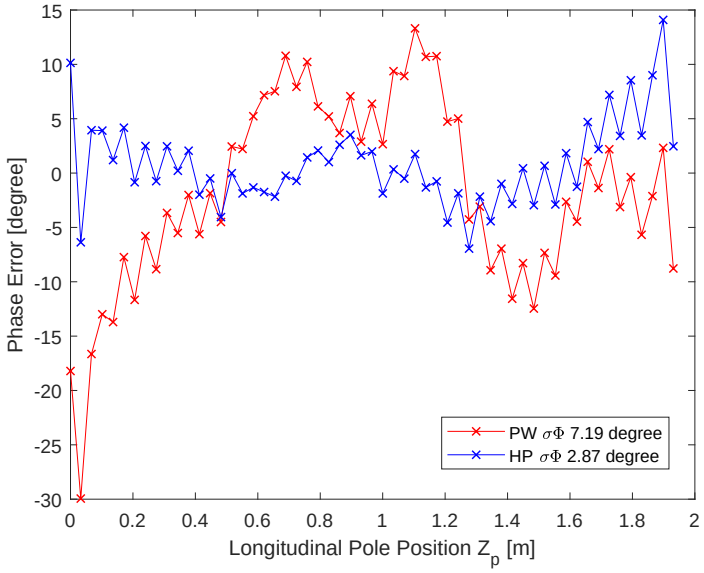

Figure 62: PW and HP phase error comparison at minimum undulator gap.

And over the entire measured range of the undulator gaps, the RMS phase error was calculated and shown in figure 63 while the standard deviation of the RMS phase error is shown in figure 64.

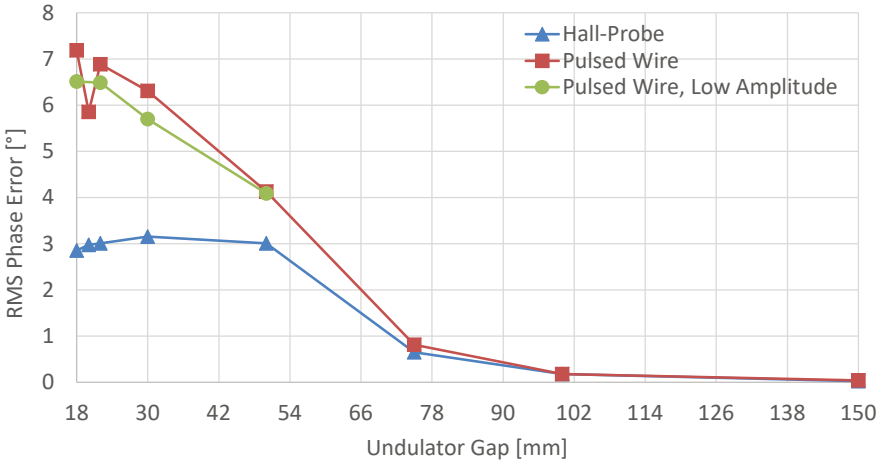

Figure 63: RMS Phase error measured using the PW and HP systems.

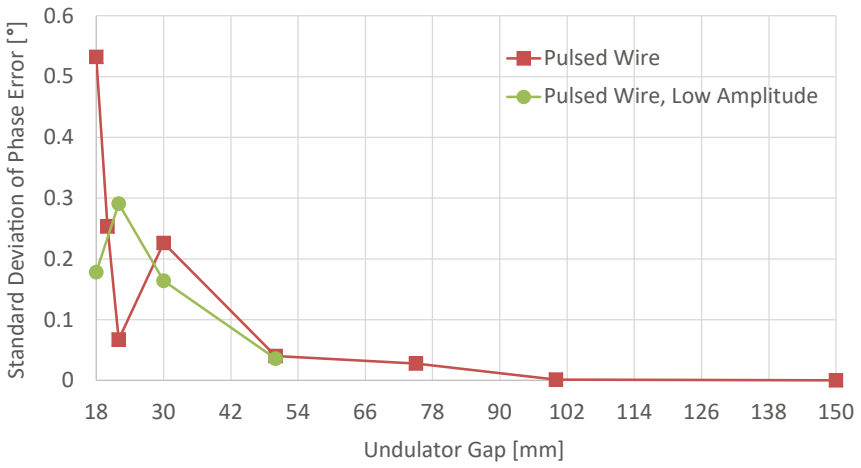

Figure 64: RMS Phase error measured using the PW and HP systems.

From figures 63, we can see the large difference in the measured RMS phase errors using the PW as opposed to what the undulator actually has, as measured by the HP.
Furthermore, we can see from figure 64 that the random error deviation of RMS phase error quantity is too small to explain the large differences in the measured values. Which indicates that the deviation of the measured values within the PW system is mainly caused by a systematic effect.

To shed more light on this discrepancy, we can isolate the contribution of the PW system towards the RMS phase error measurement from what is actually present in the undulator (as measured by the HP system):
Error of RMS Phase Error $\sigma_{\Phi_{err}} = \sqrt{\sigma^2_{\Phi_{PW}} - \sigma^2_{\Phi_{HP}}}$.

We can then see the how $\sigma_{\Phi_{err}}$ scales against $\sigma_{B_{p,err}}$ in figure 65. Where there seems to be a clear relationship between the measurement errors of the pole field and the RMS phase error.

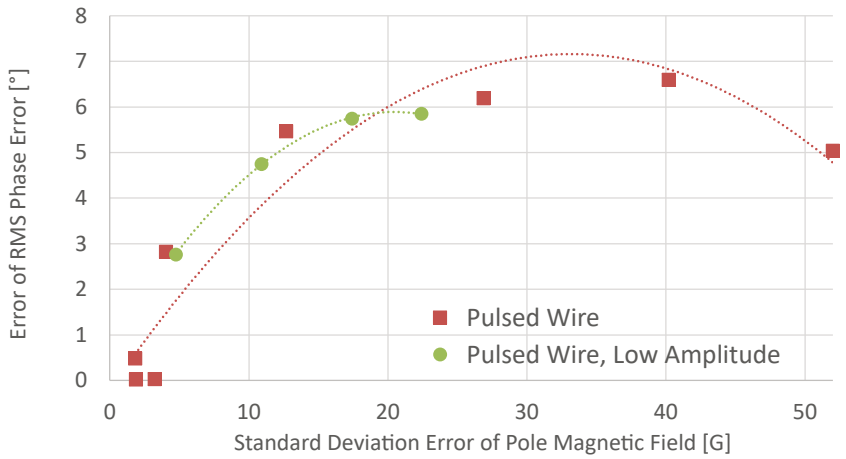

Figure 65: The error in the RMS Phase Error measurement against the error in pole magnetic field measurement.

The RMS Phase error is the single most widely used figure in characterizing the quality of an undulator, as it directly effects the longitudinal coherence of the emitted X-rays.
Experimental results of the wire oscillation within the PW system revealed a modulated wave component which is not predicted by the model used. These waves had a direct impact on the magnitude of the measured magnetic field.
Moreover, the field error grew non-linearly with the amplitude of the transverse waves, and this had a direct effect on the measurement of the RMS Phase error.

5.2.7 Searching for Optimal Results

The measurement shown earlier are not considered adequate for the characterization of an ID. This was most obvious when comparing the phase error between the PW and HP systems for the same ID.
After investigating the origin of the measurement discrepancy, it was found that the results vary widely and cyclically with respect to the oscillation observation point represented by the sensor's longitudinal position along the wire.
The sensor position is mounted on a longitudinal translation stage that has a stroke of $50mm$. That is a relatively short distance compared to the ID or wire lengths, nevertheless, measurements scanning this range were sufficient to reveal the locations where results were systematically improved and degraded.
The sensor scans were performed for the $100\mu m$ CuNiSi wire discussed in detail earlier at a tension of $4.2N$, and was done at an ID gap of $22mm$. Then, a $200\mu m$ TiAlV wire at a tension of $27.3N$ was used and it was tested for ID gaps of 18, 20 and $22mm$.
The results of the measurements were analyzed and compared to the known parameters of the ID, and the difference between the measured quantities are presented.
Figure 66 shows the relative error in the effective field seen by the pulsed wire for the

measured range of observation points $(100 \cdot (B_{eff,PW} - B_{eff,HP})/B_{eff,HP})$.

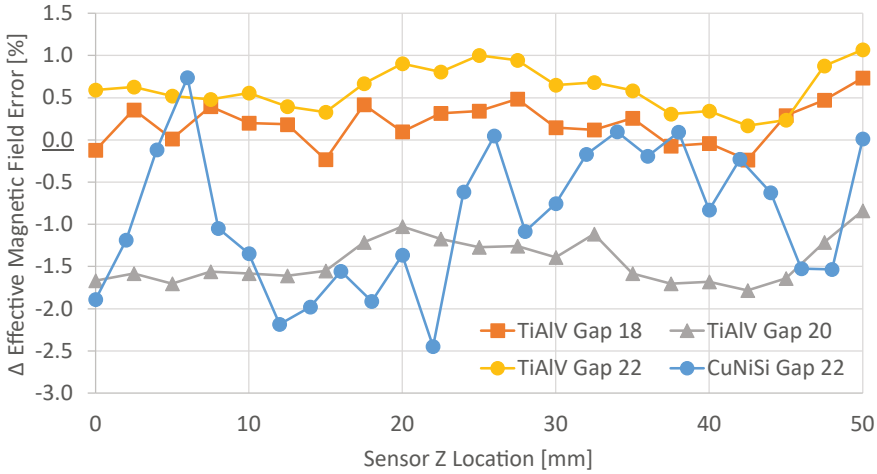

Figure 66: Relative Error of PW Effective Magnetic Field vs. Observation Point.

The effective field as measured by the PW system is directly related to the amplitude of the wire vibrations. Therefore the oscillation amplitudes seem to vary as the wave propagates the wire. Moreover, this variation seems larger in the Copper wire when compared to Titanium despite the higher SNR of the copper signal.

Figure 67 shows the error in the measured magnetic pole field spread against the observation point $(\sigma_{B_p,PW} - \sigma_{B_p,HP})$.

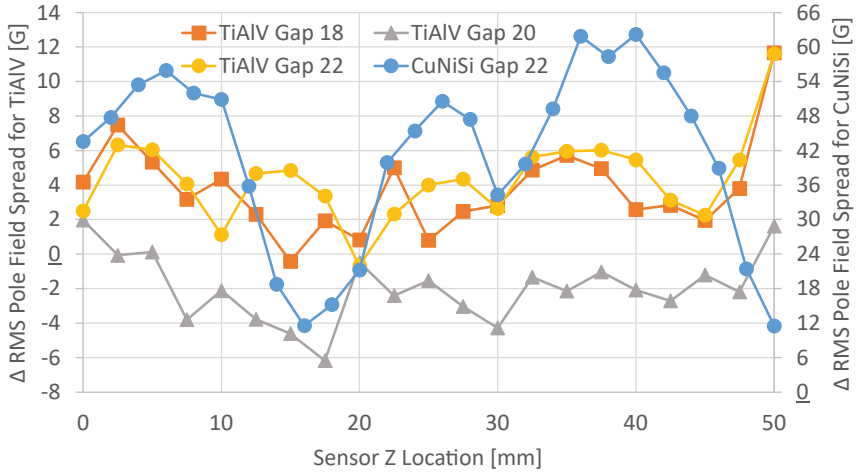

Figure 67: Error of PW RMS Pole Field Spread vs. Observation Point.

The pole field spread is a measure of how much variation seemingly exists within the magnetic field of the undulator as seen by the PW. We have seen in section 5.2.5 that the apparent variation in the magnetic field are exaggerated due to unwanted modulation of the wire oscillations.
The results for Copper and Titanium were drawn on two separate vertical axis in order to display the shape of the variation despite their difference in magnitudes.

Figure 68 shows the error in the measured RMS Phase error of the pulsed wire system against the observation point ($\sigma_{\Phi,PW} - \sigma_{\Phi,HP}$).

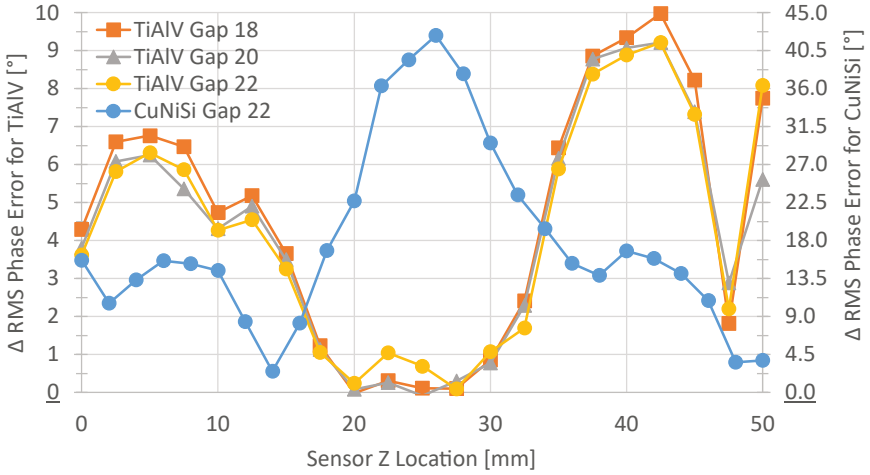

Figure 68: Error of PW RMS Phase Error vs. Observation Point.

Here we can see that both wires report better results when observed at certain "sweet spots" and the titanium wire seems to show very impressive results with a difference of under 1° over a large range ($10mm$). If we assume that the measured phase error is unlikely to be reduced due to wire distortions, then we can search the observation point for the "sweet spots" of minimal phase error when attempting to measure an unknown undulator. Moreover, the position of these spots was found to be static except when changing wire tension. Meaning that once the wire is placed and tensioned, only a single search procedure is required.

Figure 69 shows the error in the measured ID taper as seen by the PW system, compared to the HP results ($Taper_{PW} - Taper_{HP}$).

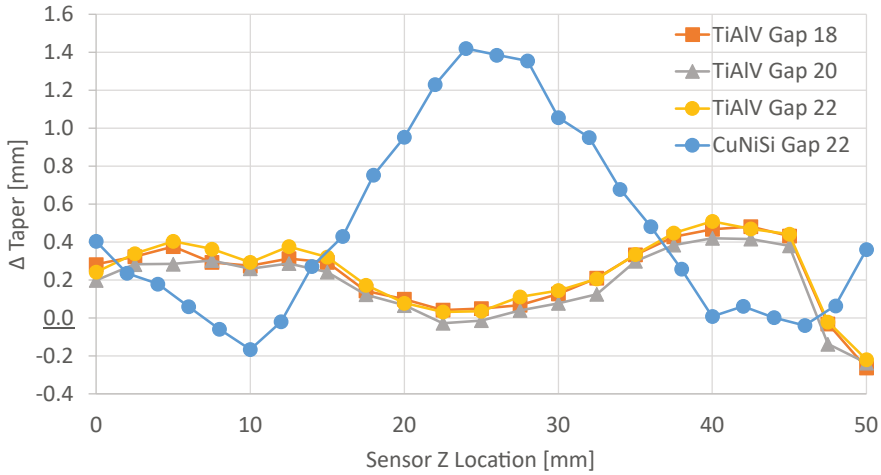

Figure 69: Error of PW Taper vs. Observation Point.

Taper is a measure of the gradual increase or decrease of the magnetic field along the beam axis, and can be influenced by attenuation of the PW oscillations as the wave propagates the wire. Nevertheless, the taper error for Titanium seems to be closest to zero in the same range where the RMS phase error error is low.

Now as we have identified a method to get PW results with reduced systematic errors, we can take a closer look at the ID measurement results and comparison against the HP. Where the results are taken from the wire observation point that provided the lowest RMS phase error (the "sweet spots").
Mainly, the pole field, the phase error and the expected radiation spectrum are shown.
The radiation spectrum is calculated using the parameters of MAX IV's $3GeV$ ring electron beam, observed $30m$ away from the source (undulator) and using an acceptance of $16\mu Rad$. This is to simulate a typical beamline and therefore compare the undulator result in its use scenario.

At the ID gap of $18mm$ and using the TiAlV wire, the observation point at $25.0mm$ was used. Figures 70 and 71 show pole fields and the PW measured RMS Phase Error compared against the HP respectively.

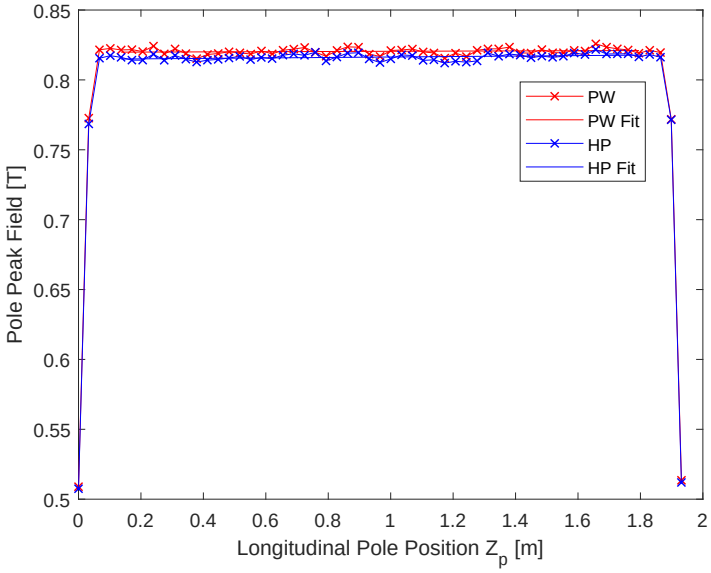

Figure 70: Pole field measurement for 18mm ID gap using TiAlV wire at the "sweet spot".

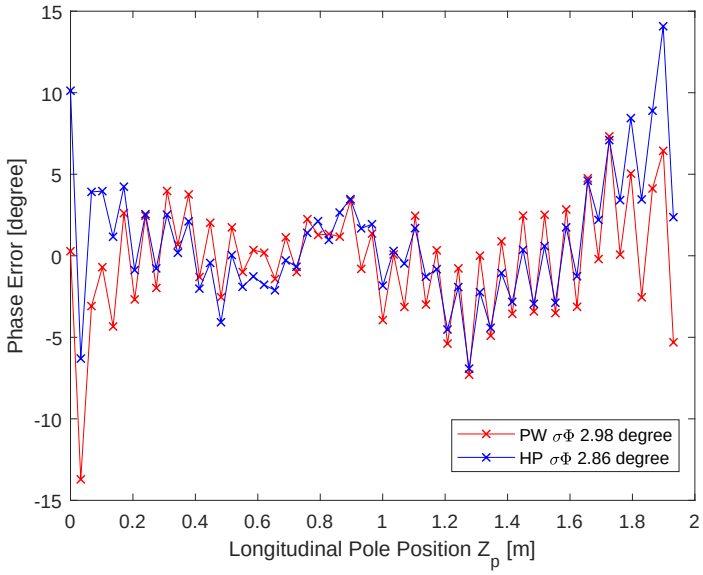

Figure 71: Phase Error measurement for 18mm ID gap using TiAlV wire at the "sweet spot".

The structure of the pole fields reported by the two systems seem to correlate well, and the modulation effect seen earlier is not dominant. This also reflects on the measured phase error, where the PW reports an RMS of 2.98° and the HP reports 2.85°.
Figure 72 shows the simulated X-Ray radiation spectrum of the ID at $18mm$ gap, calcu-

lated using the magnetic fields measured with the HP and the PW measurement systems.

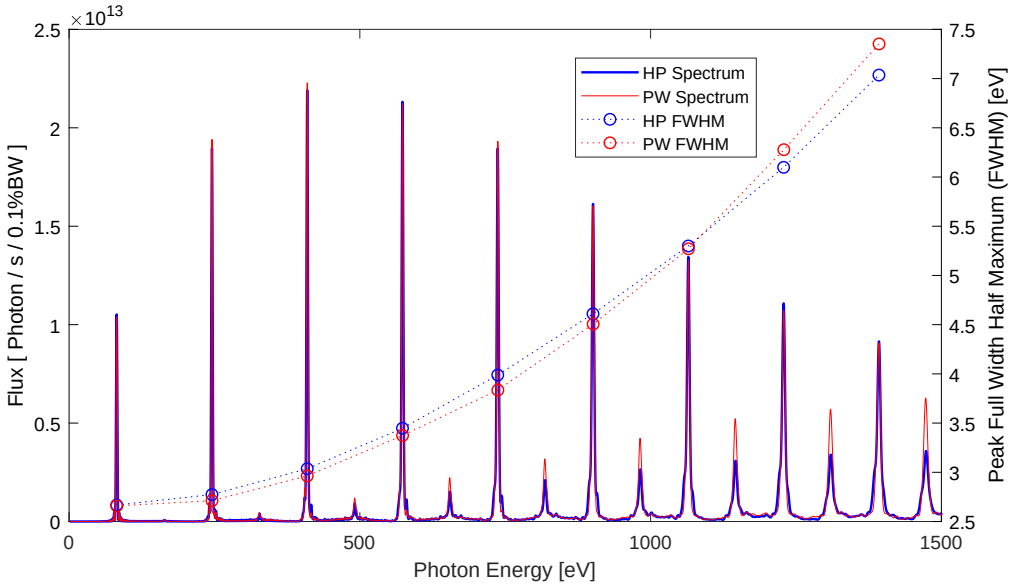

Figure 72: Simulated Photon Flux Comparison between HP and PW at 18mm Gap.

The PW measurement spectrum had reported photon energies 0.72% lower than the HP, which is to be expected due to the 0.34% higher reported effective magnetic field (see equations A.12 and B.3). The energy offset of the PW was corrected in the figure. And the FWHM of the radiated peaks is calculated and shown.

At the ID gap of $20mm$ and using the TiAlV wire, the observation point at $20.0mm$ was used. Figures 73 and 74 show pole fields and the PW measured RMS Phase Error compared against the HP respectively.

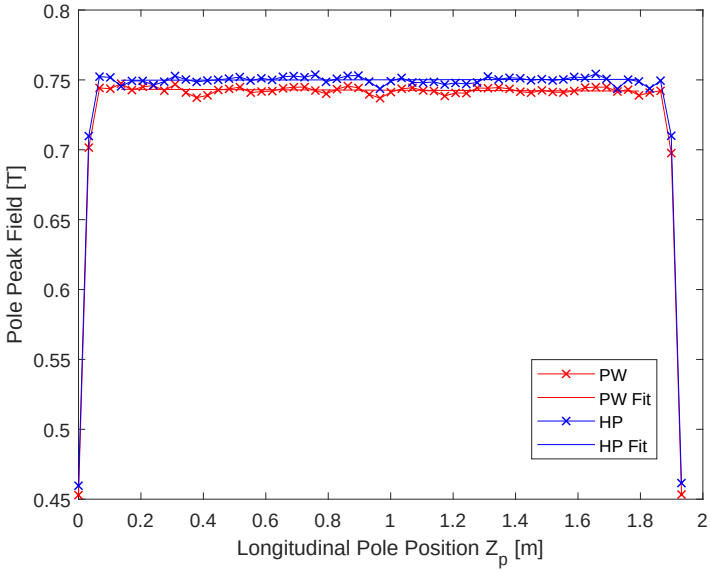

Figure 73: Pole field measurement for 20mm ID gap using TiAlV wire at the "sweet spot".

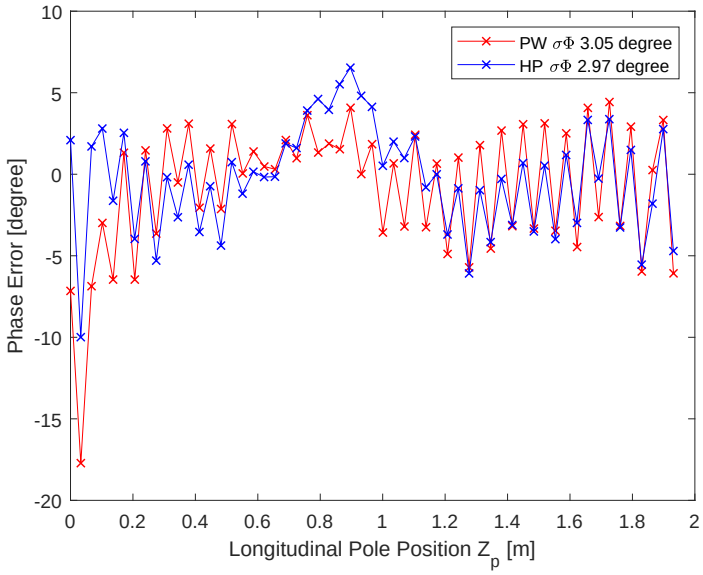

Figure 74: Phase Error measurement for 20mm ID gap using TiAlV wire at the "sweet spot".

The pole field structures reported by the two systems seem similar without significant modulation effect, despite the lower field magnitude seen by the PW. The measured phase errors report similar overall structures, and the PW reports an RMS of 3.05° while the HP reports 2.97°.

Figure 75 shows simulated X-Ray spectrum for the test ID at $20mm$ gap with magnetic field data measured using the HP and PW systems.

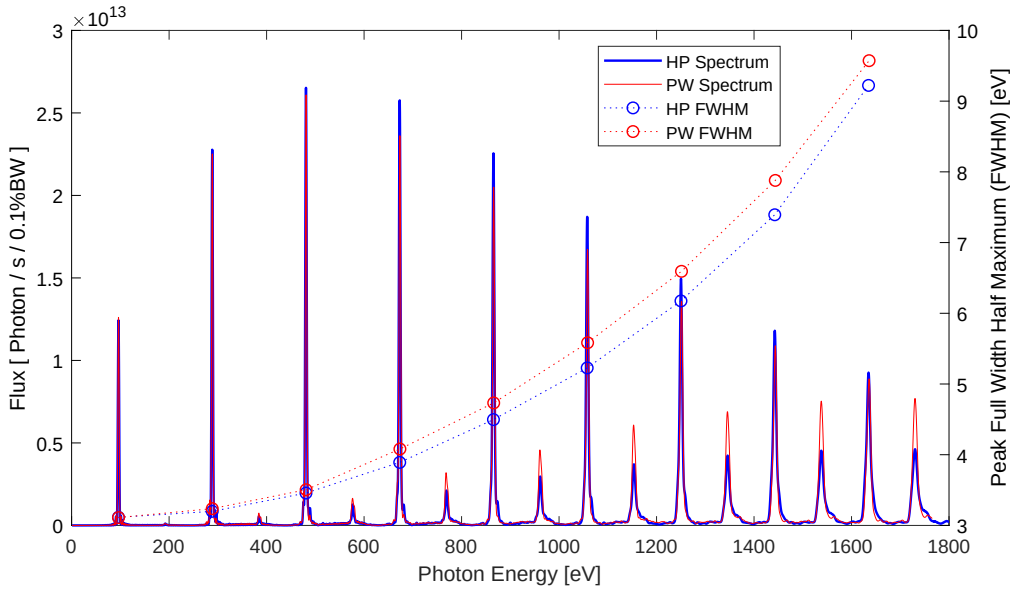

Figure 75: Simulated Photon Flux Comparison between HP and PW at 20mm Gap.

Here the PW measurement spectrum had reported photon energies 1.96% higher than the HP, which is also to be expected due to the 1.02% lower reported effective magnetic field. The energy offset of the PW was corrected in the figure. And the FWHM of the radiation peaks is calculated and shown.

At the ID gap of $22mm$ and using the TiAlV wire, the observation point at $27.5mm$ was used. Figures 76 and 77 show pole fields and the PW measured RMS Phase Error compared against the HP respectively.

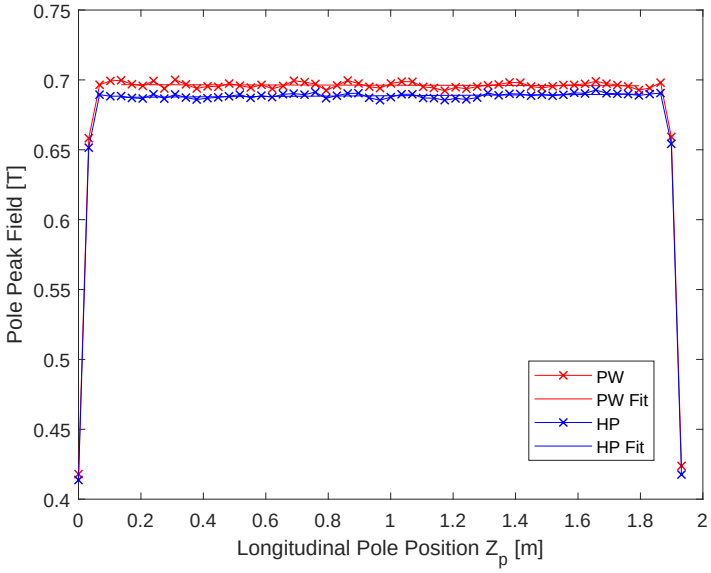

Figure 76: Pole field measurement for 22mm ID gap using TiAlV wire at the "sweet spot".

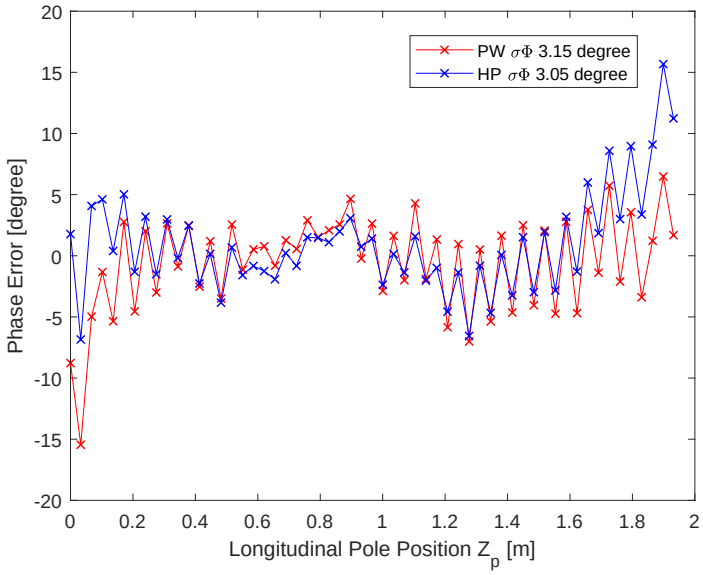

Figure 77: Phase Error measurement for 22mm ID gap using TiAlV wire at the "sweet spot".

The pole field structures reported by the two systems seem similar without significant modulation effect, despite the higher field magnitude seen by the PW. The measured phase errors report similar overall structures, and the PW reports an RMS of 3.15° and the HP reports 3.05°.

Figure 78 shows simulated X-Ray spectrum for the test ID at 22mm gap calculated using magnetic field data measured with the HP and PW systems.

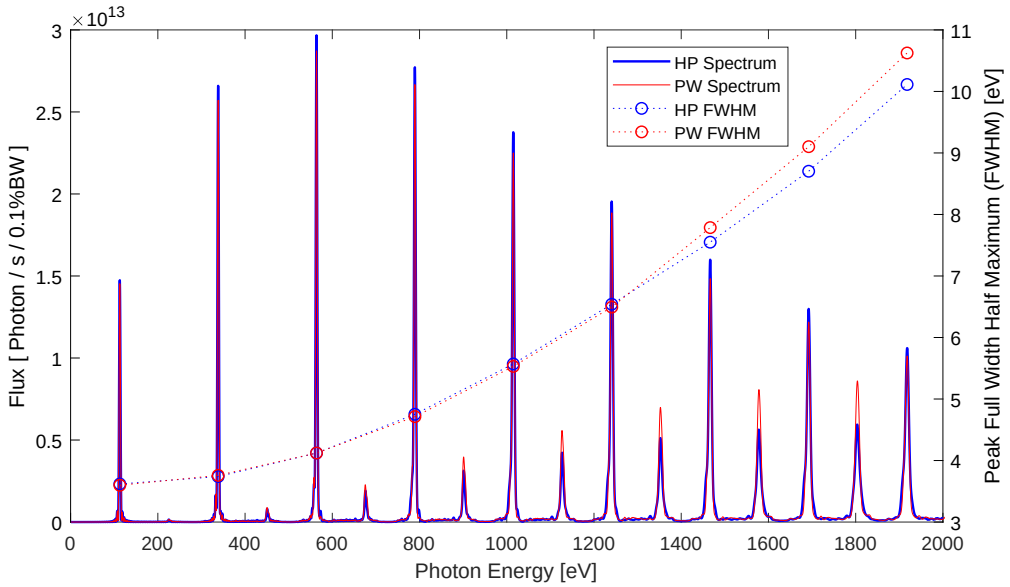

Figure 78: Simulated Photon Flux Comparison between HP and PW at 22mm Gap.

Here the PW measurement spectrum had reported photon energies 1.78% lower than the HP, which is expected due to the 0.94% higher reported effective magnetic field. The energy offset of the PW was corrected in the figure. And the FWHM of the radiation peaks is also calculated and shown.

At the ID gap of 22mm and using the CuNiSi wire, the observation point at 14.0mm was used. Figures 79 and 80 show pole fields and the PW measured RMS Phase Error compared against the HP respectively.

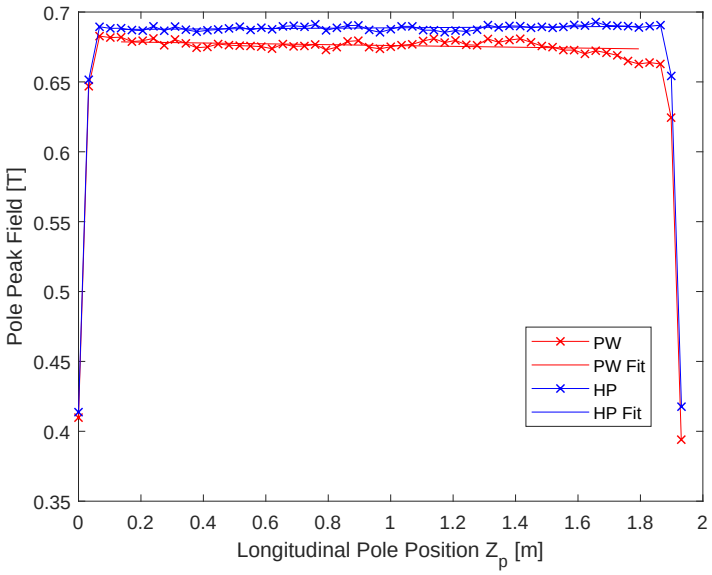

Figure 79: Pole field measurement for 20mm ID gap using CuNiSi wire at the "sweet spot".

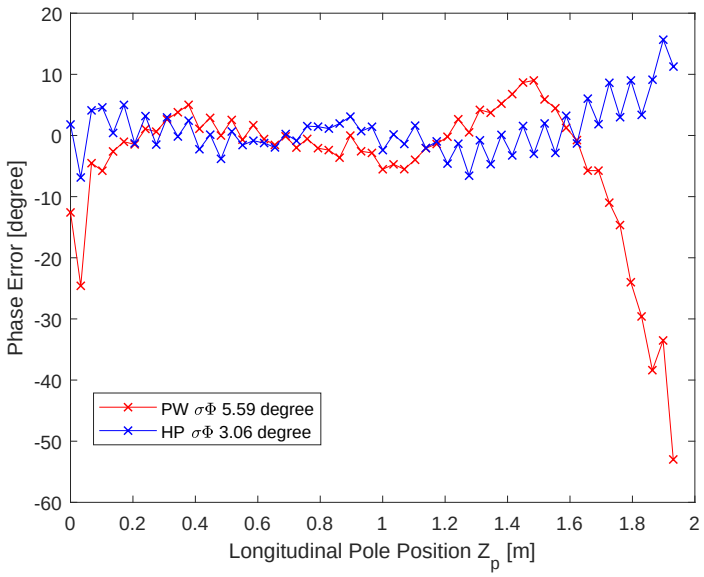

Figure 80: Phase Error measurement for 20mm ID gap using CuNiSi wire at the "sweet spot".

Here, it can seen that the pole field structure varies increasingly towards the far end of the ID, indicating the presence of wave modulation effects. The measured phase errors also diverge largely, which is why the PW reports an RMS of 5.59° and the HP reports 3.06°.

6 Wave Propagation Effects

The pulsed wire system measures the transverse traveling waves within a wire to obtain information about the magnetic fields that caused them due to it's interaction with a current pulse. It is therefore important to have a sound model of how the waves propagate through the wire material in order to successfully reconstruct the magnetic field.

6.1 Coupled Oscillation Model

The model used in equation 3.4 assumes that the wire tension, elasticity and geometry are constants. However, the model was unable to explain all the experimental observations, not to the level of accuracy that is required of the pulsed wire system for characterizing undulators, as seen by the large variation of measurement results when moving the observation point along the wire and the existence of the modulated wave component.

Beams can exhibit both a longitudinal and transverse traveling waves with the longitudinal waves propagating by compression and tension forces acting along the beam axis. It is assumed that these forces are not excited by a wire pulsed in a magnetic field since the Lorenz force can only act transversally on a moving charge. And therefore only the transverse oscillations were considered.

However, when a wire undergoes transverse deformation from its rest position, its length will slightly increase, the strain (elongation) is then given by [19]:

$$\epsilon = \sqrt{\left(1+\frac{da}{dz}\right)^2 + \left(\frac{du_x}{dz}\right)^2 + \left(\frac{du_y}{dz}\right)^2} - 1 \approx \left(\frac{da}{dz}\right) + \frac{1}{2}\left(\frac{du_x}{dz}\right)^2 + \frac{1}{2}\left(\frac{du_y}{dz}\right)^2 \tag{6.1}$$

Where ϵ is the total strain caused by the transverse wave (u_x and u_y) and the longitudinal wave (a).
Stress (σ) relates to strain by the material's Young modulus E such that $E = \sigma/\epsilon = F/(A\epsilon)$. Where F is the force and A is the cross section area. Therefore the wire's tension force T can be written as:

$$T(z,t) = T_0 + EA\epsilon = T_0 + EA\left(\frac{da}{dz}\right) + \frac{EA}{2}\left(\frac{du_x}{dz}\right)^2 + \frac{EA}{2}\left(\frac{du_y}{dz}\right)^2 \tag{6.2}$$

This can be introduced into the coupled transverse-longitudinal equation set of an Euler-Bernoulli beam with a non-constant tension [11] to produce a system of coupled equations:

$$EI_w\frac{\partial^4 u_x}{\partial z^4} - \frac{\partial}{\partial z}\left(T(z,t)\frac{\partial u_x}{\partial z}\right) + \rho A\frac{\partial^2 u_x}{\partial t^2} = B_y(z)I(t). \tag{6.3}$$

$$EI_w \frac{\partial^4 u_y}{\partial z^4} - \frac{\partial}{\partial z}\left(T(z,t)\frac{\partial u_y}{\partial z}\right) + \rho A \frac{\partial^2 u_y}{\partial t^2} = B_x(z)I(t). \tag{6.4}$$

$$\rho \frac{\partial^2 a}{\partial t^2} - E\frac{\partial^2 a}{\partial z^2} = E\frac{\partial u_x}{\partial z} \cdot \frac{\partial^2 u_x}{\partial z^2} + E\frac{\partial u_y}{\partial z} \cdot \frac{\partial^2 u_y}{\partial z^2}. \tag{6.5}$$

Equation 6.2 describes the change in tension that would occur due to both a longitudinal and transverse wave propagating through the wire.
Equations 6.3 and 6.4, describes the transverse oscillations similar to the already used model, but with the inclusion of the variable tension term. This would result in the wave reflecting part of its energy whenever entering a section of the wire with a different tension since transverse wave speed is given by $c_0 = \sqrt{T/\mu}$.
Equation 6.5, describes a non-dispersive longitudinal wave, that is constantly being generated by the transverse wave as it propagates through the wire. The longitudinal wave speed is given by $\overline{c} = \sqrt{E/\rho}$. For the case of CuNiSi wire, the longitudinal wave speed $\overline{c} = 3570m/s$ and the transverse $c_0 = 248m/s$. Therefore, the longitudinal wave speed is more than an order of magnitude faster that the transverse. Meaning that the longitudinal wave will reflect from the wire ends multiple times while the first transverse wave is being measured.

6.2 Coupled Oscillation PDE Solver

To further investigate the validity of the coupled model a custom PDE solver was written using the finite difference method [20] to simulate the effect of the transverse wave propagating through the wire. The simulation calculates the transverse and longitudinal waves and dynamically adjusts the local wire tension as the time progresses. The dispersion effect was not modeled in this simulation and therefore the EI_w term was set to 0 to simplify the solver using only a 2^{nd} order PDE instead of a 4^{th}. Future work can go towards coupling the dispersion effect directly into the PDE solver.
Dirichlet boundary conditions were used for both the transverse and longitudinal waves where the wire is fixed at both ends $u_x = u_y = a = 0, z = 0, L$ where L is the total wire length.
Figure 81 shows a basic overview of the PDE solver algorithm using an explicit finite difference method where the solution is always calculated for next time step from previous time steps.
This simulation solves for the variables $u_x(z,t)$, $u_y(z,t)$ and $a(z,t)$. Meaning that points in space and time can be reached. However, to simulate a pulsed wire measurement, the waves along the wire can be neglected except for a single point (the observation point) where the sensor is located and the waves were recorded in time as they pass that point.

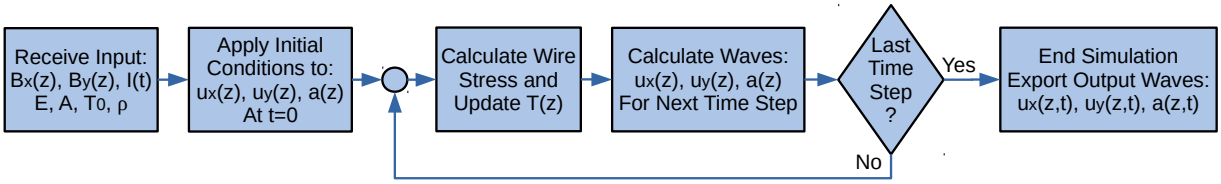

Figure 81: Overview of the Custom Built Coupled PDE Solver Algorithm.

6.3 Coupled Oscillation Simulations

In order to facilitate evaluating this model, simulations mimicking the experimental results of chapter 5.2 were performed using the known material properties of the CuNiSi wire and the HP measured magnetic field for the test undulator at $18mm$ gap.
Figures 82 and 83 show the transverse and longitudinal wire oscillations respectively. Where the characteristic wake behind the transverse wave has appeared similar to experimental results seen in figure 51.
The longitudinal oscillations have reflected 4 times during the measurement, which was expected due to its higher velocity indicating that it has already started to form a standing wave.

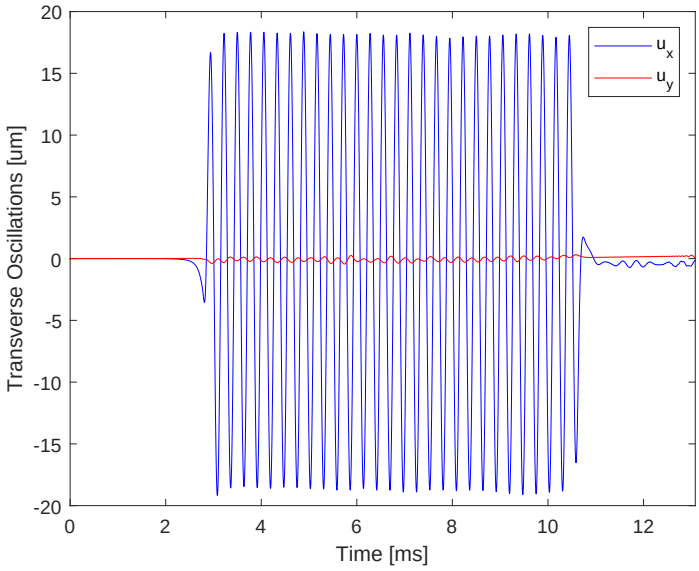

Figure 82: Simulated Transverse Oscillations Using the Coupled Model.

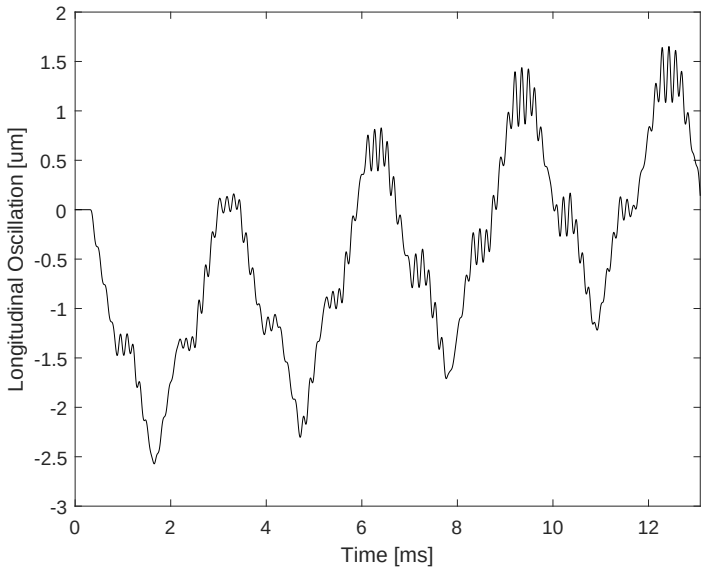

Figure 83: Simulated Longitudinal Oscillations Using the Coupled Model.

Figure 84 shows the change (modulation) of peak fields when a transverse wave is coupled to the longitudinal in simulation. Here we can notice that the modulation effect grows more towards the end of the ID, and that the modulation value was about ±0.5% which is half of what was seen earlier in the experimental results in figure 60.

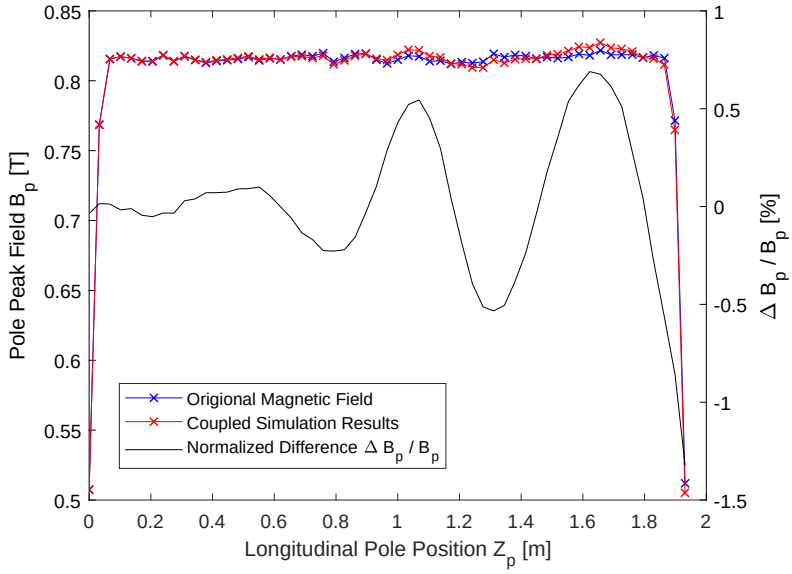

Figure 84: Simulated Peak Field Variation Using the Coupled Model.

Figure 85 shows the change of phase error due to the modulation of the wire oscillations when using coupled simulations. Here again the phase error diverges more the further away it is in space, since the wave have to propagate a longer distance through the turbulent wire medium.

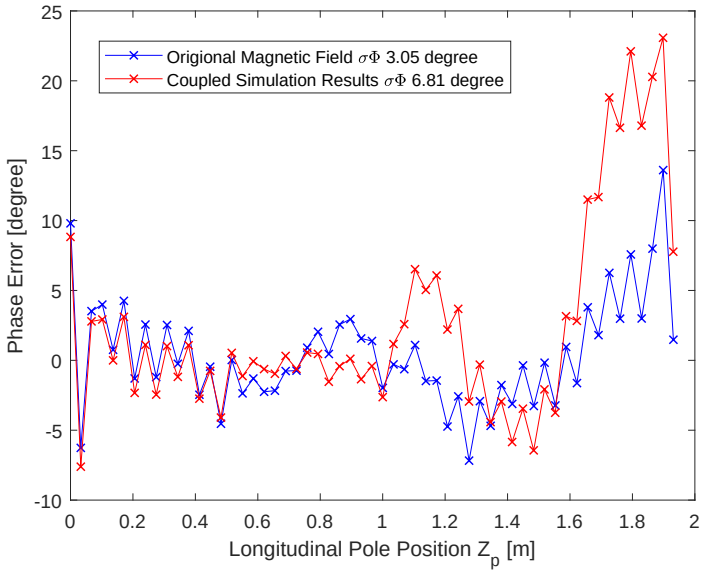

Figure 85: Simulated Phase Error Using the Coupled Model.

Next the simulation was used to see the effect of searching for a "Sweet spot" similar to the experimental results seen in chapter 5.2.7 where the observation point (the sensor location) is varied across the wire to find the location where the PW measured ID parameters best match the known ID. And more importantly, how to find the "sweet spot" for an unknown ID.
Figure 86 shows the effect of scanning the observation point in coupled simulation on the effective magnetic field. Here the change is much less than what was seen in the experimental results and the errors are in the range of $\pm 0.1\%$. Nevertheless, the error (difference) seems to vanish to zero at the observation points $6mm, 22mm$ and $44mm$.

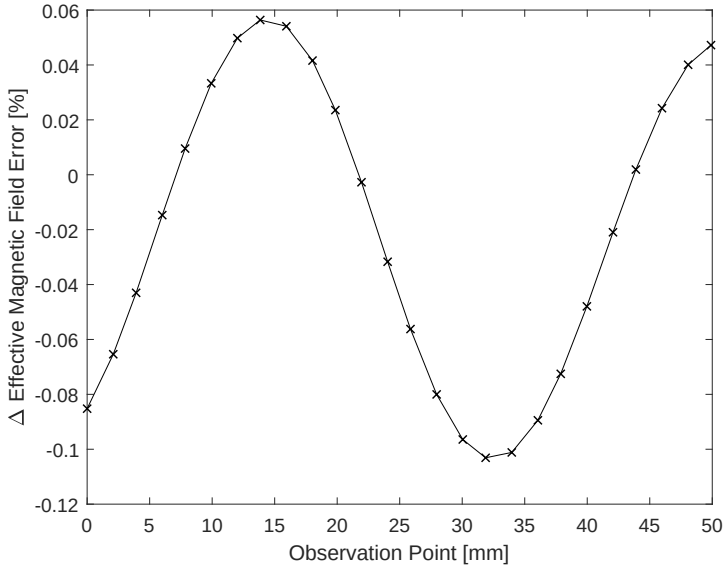

Figure 86: Simulated Effective Field Variation Against Observation Point Using Coupled Model.

Figure 87 shows the effect of scanning the observation point in coupled simulation on the RMS pole field spread, which reflects the amplitude of the wave modulation effect seen at that point. Here the difference minimized at the observation points $14mm$ and $22mm$.

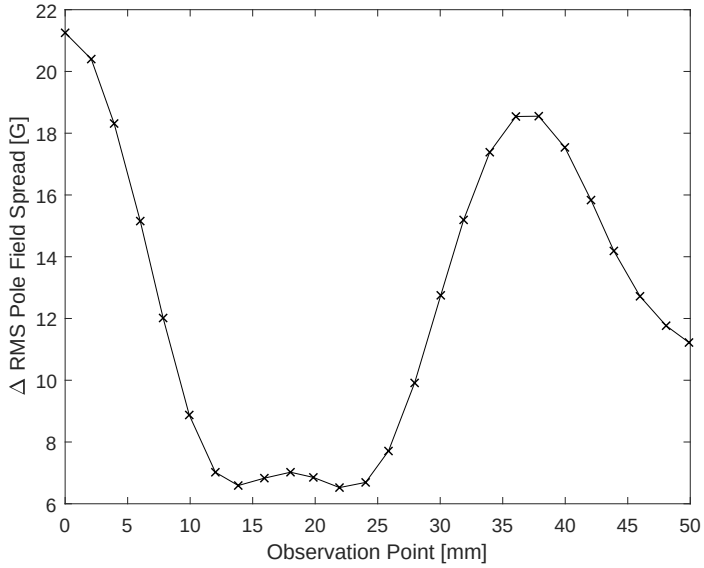

Figure 87: Simulated Peak Field Spread Against Observation Point Using Coupled Model.

Figure 88 shows the difference in RMS phase error between the original ID field used in the

simulation and the recovered field from the simulation at the range of observation points. The difference shows a minima at the $22mm$ point.

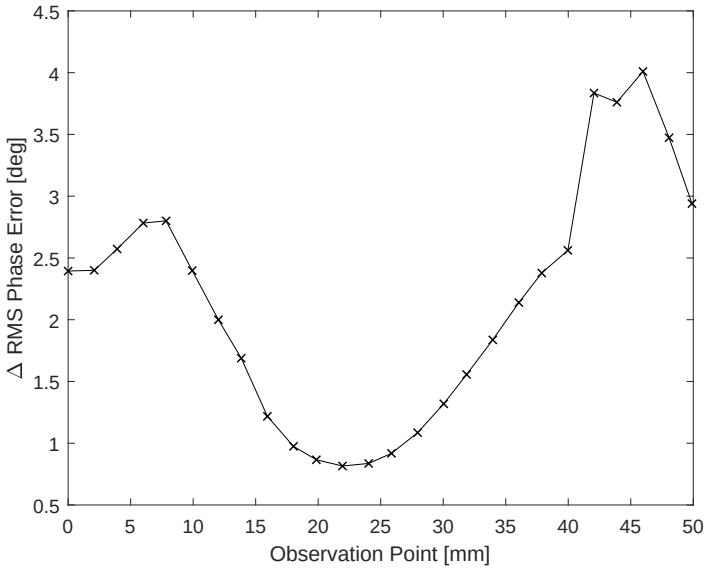

Figure 88: Simulated Phase Error Variation Against Observation Point Using Coupled Model.

Figure 89 shows the difference in Taper between the original ID field used in the simulation and the recovered field from the simulation at the range of observation points. The difference vanishes to zero at the $6mm, 22mm$ and $40mm$.

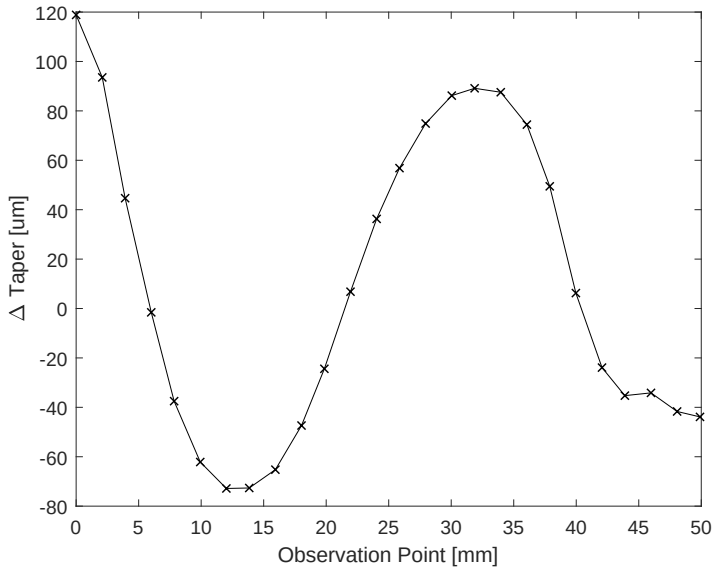

Figure 89: Simulated Taper Variation Against Observation Point Using Coupled Model.

The ID parameters recovered from the coupled simulations seem to vary against the observation point, this behavior was seen in the experiment but was more aggressive with larger variation in the values. Nevertheless, all the differences between the original ID parameters and the recovered ones seem to have minimum values. And the observation point which gave the lowest RMS phase error was a common one in all studied parameters ($22mm$ in this case).
This gives validation to the method of searching for the lowest RMS phase error when attempting to measure an unknown ID as it will also minimize the errors in the remaining parameters.

7 Conclusions

Pulsed wire magnetic measurements proved to be a challenging topic that enables measuring any closed structure ID with limited physical access. This allows for reduced complexity in the ID design by shifting it towards the measurement tool which could reflect as cost saving especially for FELs where tens of identical undulators must be built. Applications of this tool can extend beyond measuring ID magnetic fields, as it can be used to measure local magnetic field distributions in accelerator magnets such as dipoles, quadrupoles, etc. where the fringe fields are of importance.

The thesis work can be thought of in two folds. First is the system as a tool for exciting and detecting the wire oscillations. This involved the design and calibration of the wire position sensor, the effect of a moving wire in a magnetic field, background vibrations and noise sources. These technicalities were identified and solutions were offered to overcome their effects.

The second is the system as an undulator characterization tool. A method to design and use an arbitrary pulse shape was suggested and tested. While comparing the measurement results against the well-proven Hall-probe mapper data for the same undulator, the pulsed wire results seemed to be systematically modulated, resulting in an un-acceptable level of measurement errors.
An experimental method for reducing the modulation effect was luckily found, and this was able to give impressive results when applied. This method involves searching for the observation point which minimizes the phase error and the modulation effects.
Attempting to explain this method using the established model for the wire was unsuccessful at re-producing the experimental observations, because the model was built to explain (and correct) the dispersion effect only.
This has lead to the formulation of another wire model that takes into account the stress generated by the transverse oscillations which would generate longitudinal waves within the wire. That in turn, affects the transverse waves as they propagate through the wire with dynamically varying stress.
The wave propagation through this dynamic medium was successfully simulated and was able to produce the experimentally observed behaviors of the wave modulation and the emergence of low distortion observation points. This gives validation to the experimental method of searching for the minimal phase error.

Overall the pulsed wire method seems capable of obtaining reliable magnetic field measurements when enough care is taken into the process. And future work can still go towards the development of this method such as testing more wire materials, testing the measurements on a known small period undulator, studying the effect of longitudinal waves at the wire ends (boundary conditions) and better modeling of the wave propagation through the wire.

A Appendix on Synchrotron Radiation

A.1 Particle Motion in an Insertion Device

The magnetic field can be assumed to be purely vertical ($B_x = B_z = 0$), then for a relativistic electron beam incoming along the z-axis, experiencing small horizontal deviations ($\dot{x} \ll 1$), the equation of motion can be expressed as [4]:

$$\ddot{x} = \frac{d^2x}{dz^2} = \frac{eB_y}{\gamma m_0 c}. \tag{A.1}$$

For a sinusoidal magnetic field having period length λ_u and magnitude B_0:

$$B_y(z) = -B_0 \sin\left(\frac{2\pi z}{\lambda_u}\right) \tag{A.2}$$

we can integrate to find the deflection angle from the z-axis:

$$\dot{x}(z) = \frac{dx}{dz} = \frac{e}{\gamma m_0 c}\int B_y(z)\cdot dz = \frac{B_0 e}{\gamma m_0 c}\frac{\lambda_u}{2\pi}\cos\left(\frac{2\pi z}{\lambda_u}\right) \tag{A.3}$$

and the maximum deflection being:

$$\frac{B_0 e}{\gamma m_0 c}\frac{\lambda_u}{2\pi} = \frac{K}{\gamma},$$

where K known as the "deflection parameter" is unit-less and is an important property of every ID as we shall later see, K is defined as:

$$K \equiv \frac{B_0 e}{m_0 c}\frac{\lambda_u}{2\pi} = 93.36 B_0[T]\lambda_u[m]. \tag{A.4}$$

Another integral gives us the electron's position:

$$x(z) = \frac{e}{\gamma m_0 c}\iint B_y(z)\cdot dz = \frac{K}{\gamma}\frac{\lambda_u}{2\pi}\sin\left(\frac{2\pi z}{\lambda_u}\right) \tag{A.5}$$

and if we approximate $\Delta z = c\Delta t$ we can write:

$$\dot{x}(z) = \frac{\Delta x}{\Delta z} = \frac{\Delta x}{c\Delta t} = \frac{1}{c}\frac{dx}{dt} = \frac{\upsilon_x}{c} \equiv \beta_x, \tag{A.6}$$

but as the electron energy is fixed, so is β. Therefore, any change in β_x must be counteracted by a change in β_z. Since ($\beta^2 = \beta_x^2 + \beta_z^2$) we can write:

$$\beta_z^2 = \beta^2 - \beta_x^2 = \beta^2 - \frac{K^2}{\gamma^2}\cos^2\left(\frac{2\pi z}{\lambda_u}\right) = \beta^2 - \frac{K^2}{\gamma^2}\left(\frac{1}{2} + \frac{1}{2}\cos\left(\frac{4\pi z}{\lambda_u}\right)\right) \tag{A.7}$$

and the $\sqrt{1-x} \approx 1 - x/2$ approximation can be used to get:

$$\beta_z \approx \beta \left(1 - \frac{K^2}{4\beta^2\gamma^2} - \frac{K^2}{4\beta^2\gamma^2} \cos\left(\frac{4\pi z}{\lambda_u}\right)\right) \tag{A.8}$$

where we can see that the longitudinal particle speed consists of a constant and an oscillatory cosine component. Averaging over one cycle we get the average speed:

$$\overline{\beta}_z \approx \beta - \frac{K^2}{4\beta\gamma^2} \approx 1 - \frac{1}{2\gamma^2} - \frac{K^2}{4\beta\gamma^2} \tag{A.9}$$

A.2 Undulator Radiation

Now we have described the motion of a relativistic electron in the magnetic field of an ID which will generate electromagnetic radiation due to its oscillatory trajectory.
Undulators are Insertion Devices built with relatively small K-values ($K \approx< 10$), this produces oscillations that are narrow enough to enable interference between successive radiated wavefronts. Now we can investigate two radiated wavefronts, emitted at angle θ from the same electron and separated by a distance d as in Figure 90.

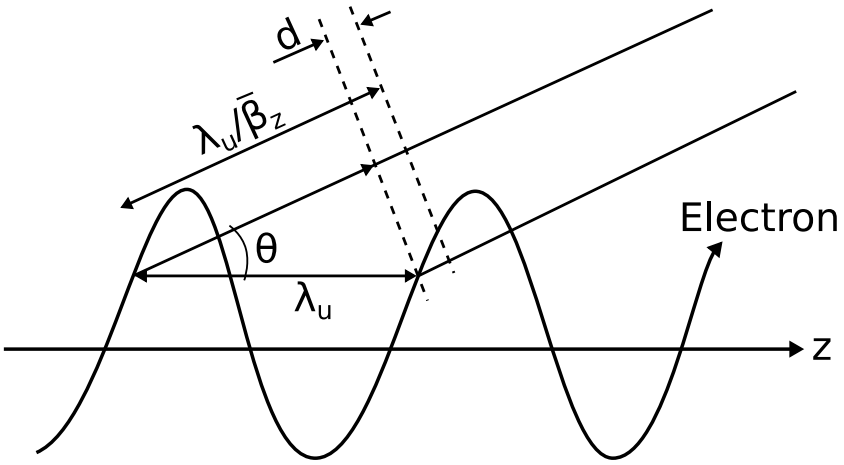

Figure 90: An electron trajectory in an Undulator showing two radiated wavefronts (dashed lines).

The time required for the electron to move one period is $\lambda_u/c\overline{\beta}_z$ during which the first wavefront had travelled a distance of $\lambda_u/\overline{\beta}_z$ and the separation distance d is now:

$$d = \frac{\lambda_u}{\overline{\beta}_z} - \lambda_u \cos\theta. \tag{A.10}$$

In order for constructive interference to occur, we impose a condition that the separation distance between wavefronts must be an integer multiple of the wavelength $d = n\lambda$ which allows us to write:

$$n\lambda = \frac{\lambda_u}{\overline{\beta}_z} - \lambda_u \cos\theta \approx \lambda_u \left(1 + \frac{1}{2\gamma^2} + \frac{K^2}{4\beta\gamma^2}\right) - \lambda_u \cos\theta \tag{A.11}$$

which can be further approximated and rearranged to obtain the Undulator Equation:

$$\lambda = \frac{\lambda_u}{2n\gamma^2}\left(1 + \frac{K^2}{2} + \theta^2\gamma^2\right). \tag{A.12}$$

Which tells us that the radiation wavelength out of an undulator is approximately its period length compressed by the large factor γ^2. In practice, we can adjust the wavelength -and energy- of the generated light by closing or opening the undulator gap which respectively increases or decreases the magnetic field amplitude in the beam axis, thus smoothly controlling the K value to produce the radiation wavelength required by the experiment. We can also note that an undulator allows the generation of smaller wavelengths at integer divisions of the fundamental. Meaning that higher energy photons are also available to the experiment at integer harmonics.

B Appendix on Undulator Performance Figures

B.1 K-Value of an Insertion Device

The most obvious parameter to consider is the K-value of the ID, this is the most direct and essential parameter to ensure that the radiation wavelength is as expected (see equation A.12). From equation A.4 we can see that both the period length and the peak field need to be known to obtain the K-value and that is accomplished by fitting a sum of odd sinusoidal functions over each half-period [5]:

$$B(z)_{fit} = \sum_{n=0} b_{2n+1} \cos\left(\frac{2\pi(2n+1)}{\lambda_u}(z - z_{2n+1})\right) \tag{B.1}$$

which is then used to calculate the effective field value for each half-period:

$$B_{eff} = \sqrt{\sum_{n=0}\left(\frac{b_{2n+1}}{2n+1}\right)^2} \tag{B.2}$$

and the average effective field throughout the device $\overline{B_{eff}}$ is then used to calculate the K_{eff} value:

$$K_{eff} = \frac{e\overline{B_{eff}}}{m_0 c}\frac{\lambda_u}{2\pi} = 93.36\overline{B_{eff}}[T]\lambda_u[m]. \tag{B.3}$$

B.2 Field Integrals and Electron Trajectory

Insertion devices need to work within an accelerator machine which might house many other insertion devices for different experiments (beamlines). The electrons in these machines need to have a stable orbit regardless of which insertion devices are in operation at the moment and hence insertion devices need to have as little impact on the overall electron position and angle as possible.
Looking at equations A.3 and A.5 we can see that the angle of the electron beam is proportional to the field integral, and the position is proportional to the second field integral.
The first and second field integrals are defined as:

$$I_{1(x,y)}(z) \equiv \int_{-\infty}^{z} B_{x,y}(\zeta) \cdot d\zeta \tag{B.4}$$

and:

$$I_{2(x,y)}(z) \equiv \int_{-\infty}^{z} I_{1(x,y)}(\zeta) \cdot d\zeta = \int_{-\infty}^{z}\int_{-\infty}^{\zeta'} B_{x,y}(\zeta) \cdot d\zeta' d\zeta \tag{B.5}$$

which are used to determine the electron beam angle:

$$\dot{x}(z) = \frac{dx}{dz} = \frac{-e}{\gamma m_0 c} I_{1y}(z) \quad \text{and} \quad \dot{y}(z) = \frac{dy}{dz} = \frac{e}{\gamma m_0 c} I_{1x}(z) \tag{B.6}$$

and trajectory:

$$x(z) = \frac{-e}{\gamma m_0 c} I_{2y}(z) \quad \text{and} \quad y(z) = \frac{e}{\gamma m_0 c} I_{2x}(z). \tag{B.7}$$

Therefore, even though there are large local magnetic fields within an insertion device, the average field should be close to zero and every deviation in local field should be compensated nearby its source in order to reduce the first and second field integrals.

B.3 Phase Error

Undulators rely on constructive interference between radiated wavefronts to generate well defined wavelengths that are longitudinally coherent. This imposes another restriction on the magnetic field which is the evolution of phase of the emitted wavefront from each half-period, this term is referred to as "phase" and is expressed as [6]:

$$\Phi(z) = \frac{\pi}{\lambda_u} \left(\frac{z}{\gamma^2} + \int_{-\infty}^{z} \dot{x}(\zeta)^2 \cdot d\zeta \right) \tag{B.8}$$

The phase quantity is evaluated throughout the undulator and then fitted with a linear function which is then subtracted to obtain the "phase error". The Root-Mean-Square (RMS) of all the poles phase errors is knows as the RMS phase error σ_Φ and is used to determine the expected reduction of peak radiated intensity and broadening of the peak Full Width Half Maximum (FWHM) due to magnetic field errors. The intensity reduction R can be calculated as:

$$R = \frac{N(1 - e^{-n^2\sigma_\Phi^2}) + N^2 e^{-n^2\sigma_\Phi^2}}{N^2} \approx e^{-n^2\sigma_\Phi^2} \tag{B.9}$$

where N is the number of undulator periods and n is the harmonic number. The reduction effect is calculated for different harmonics in figure 91, where it can be seen that higher harmonics suffer the most from undulator construction errors. Therefore, high energy X-ray undulators need a tighter control over the phase error.

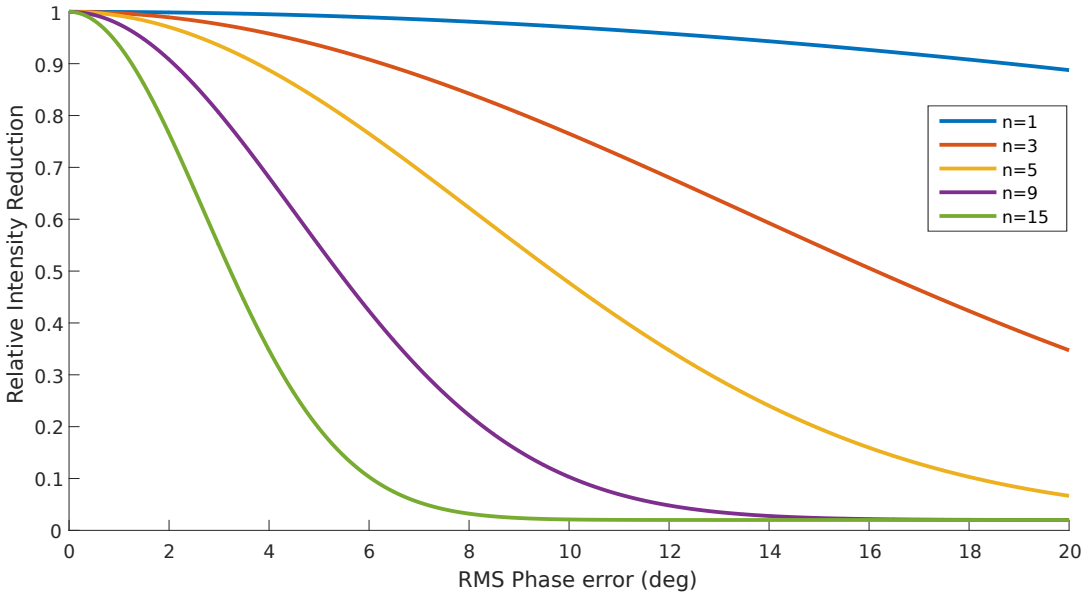

Figure 91: Intensity reduction ratio calculated for different harmonics due to RMS phase error σ_Φ within a 50 period undulator.

B.4 Taper

Taper is a property of an ID to have a smoothly increasing or decreasing magnetic field strength (or K_{eff}) between the electron beam entrance (Upstream) and exit (Downstream) ends. This is done to intentionally increase the FWHM of the emitted radiation peaks in certain experiments.
Taper can be achieved by setting a different gap at the upstream and downstream ends of an ID and can be controlled by the motion system driving the gap.
The value of the taper can be approximated as:

$$Taper = \Delta Gap = \frac{\lambda_u}{\pi} \frac{\Delta B_{eff}}{\overline{B_{eff}}} \tag{B.10}$$

B.5 Longitudinal Field

The longitudinal field component B_z doesn't exert a force on a beam traveling in the z-direction due to the cross product of the Lorentz force (equation 2.1). Also the beam deflection inside an insertion device relatively small ($\dot{x} \ll 1$), therefore the B_z component of the magnetic field can usually be neglected.

C Appendix on Undulator Measurement Techniques

This appendix presents the most common magnetic measurement techniques which are used for the measurement of magnetic fields within a insertion devices. These techniques generally fall under two categories, local field measurements that gives a value of magnetic field for each point in space and integral field measurements that measure the accumulated magnetic field quantity over the ID length.
The Hall-Probe and Pulsed Wire methods are used in local field measurements whereas the Flip Coil and Stretch Wire are integral measurement methods.

C.1 Hall-probe Mappers

Hall-probes (sensors) are thin plates of semiconductor materials with a biasing current passing through them. When magnetic fields are applied perpendicular to their surface, an electric field is produced due to the Lorentz force (see equation 2.1). Figure 92 (Source: [9], edited) shows a diagram of a Hall-plate element.
Edwin H. Hall discovered the now called Hall effect in 1879, but it took until 1948 for its

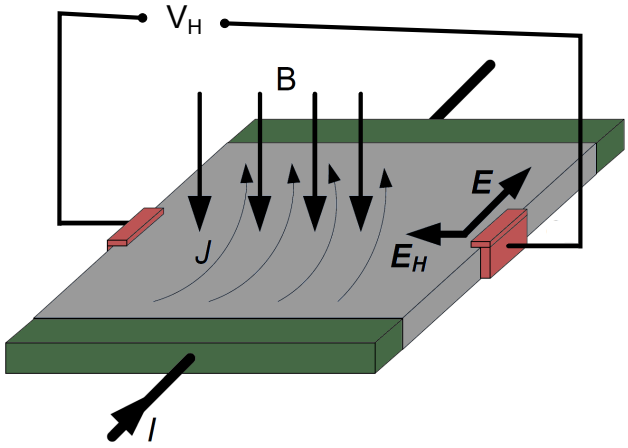

Figure 92: The Hall sensor basic arrangement.

first reported use as a magnetic measurement technique by G.L. Pearson, using germanium semiconductor [8].
The unloaded output Hall potential is given by [7]:

$$V_H = \mu_p w E B = \mu_p w \frac{J}{\sigma} B = R_H \frac{I}{t} B \quad \text{with} \quad R_H = \frac{\mu_p}{\sigma} \tag{C.1}$$

where μ_p is the carrier mobility and σ is the conductivity of the material. R_H is the Hall coefficient, which is desirable to be maximize in order to obtain the largest signal possible. This is accomplished by using high carrier mobility materials such as Indium Antimonide (InSb). Reducing the conductivity of the material has the drawback of increasing the

power dissipation in the plate which has other negative effects on the sensor.

A Hall-probe mapper is the workhorse of ID magnetic measurement laboratory, it consists of a 3D Hall-probe sensor, mounted on a 3D XYZ translation stages that can position the probe very accurately and precisely in space.

A data acquisition system that is synchronized to the position of the probe is used to sample the magnetic field at well known locations in space, thus directly obtaining the magnetic field maps containing $\boldsymbol{B}(x, y, z)$ by scanning "on-the-fly" the area of interest. The z-axis travel range of a mapper must extend beyond the length of the ID, and is the longest travel axis of the system, which leads to manufacturing the system from a single large granite piece to reduce flexing and dampen vibrations and a precision top surface to produce smooth straight travel with minimum deviations.

At MAX IV Laboratory, a 5.5m long Hall-probe mapper is used for the construction of in-house built undulators (figure 93). The peak-to-peak trajectory error of the mapper is $\Delta x = 1.5\mu m$ and $\Delta y = 2\mu m$, angular deviation $\Delta x' = 7\mu m/m$ and $\Delta y' = 8\mu m/m$, as seen in figure 94.
The Hall-probe sensor used has wide-band noise figure of $1.23\mu T$ RMS, a calibrated non-linearity of 0.15% and a total measurement accuracy of $\pm 0.25\%$.

The accuracy of the motion, sensors and data acquisition makes the Hall-probe mappers the reliable reference measurement system in any ID laboratory. The performance of the MAX IV Hall-probe mapper system has been characterized during the tuning of HIPPIE beamline undulator, table 11 shows the level of measurement errors obtained when using a single on-the-fly measurement at the maximum scan speed of $150mm/s$.

Parameter	Peak Field	Effective Field	Effective K	RMS Phase Error
Value	0.772 T	0.781 T	3.863	2.682 °
Standard Deviation σ	16.1 μT	12.7 μT	68.8 μ	0.0091 °
$\sigma/Value$	20.9 ppm	16.3 ppm	16.3 ppm	0.34 %

Table 11: Summary of MAX IV Hall-probe mapper system performance.

Figure 93: MAX IV Hall-probe mapper (left) scanning an Undulator (right).

The one limitation of using granite-based Hall-probe mappers is that they require an open frame design magnet that allows lateral access for the probe, this requires the use of a strong frame structure in order to minimize deformations in the presence of the large magnetic forces, and tends to make the IDs larger, heavier and more expensive.

The same restriction prevents the mappers from being used on an in-vacuum insertion device, where the magnets are housed within the Ultra-High-Vacuum (UHV) vessel that prevents lateral access.
Specialized in-vacuum Hall-probe systems have been developed [10], which use guide rails installed within the vacuum vessel that support the moving Hall-probe carriage as shown in figure 95 (Source: [10]). A laser system is used to measure the position and angular deviations of the moving carriage while XY stages actively deform the rails in order to compensate the Hall-probe carriage travel errors dynamically.

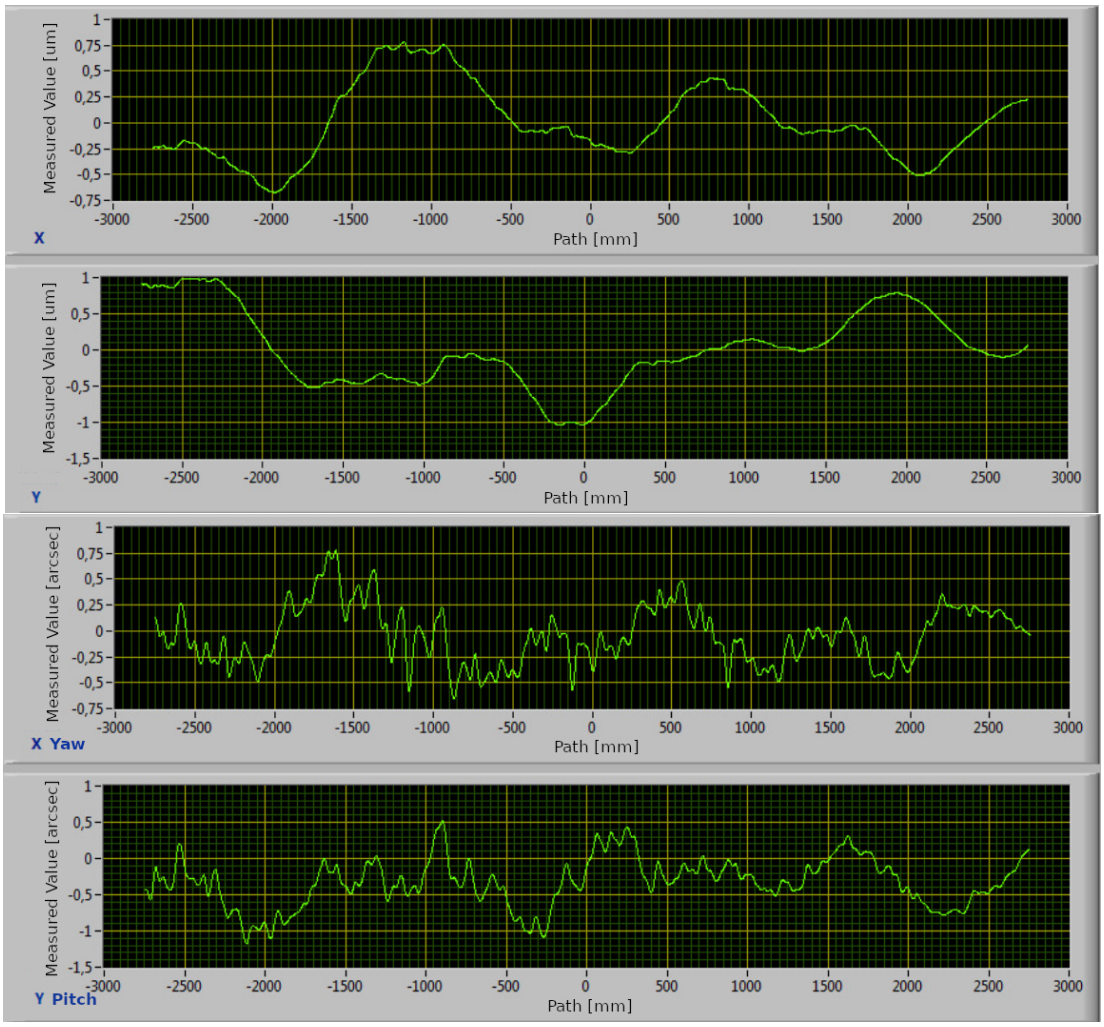

Figure 94: MAX IV Hall-probe mapper x,y trajectory (upper) and angular (lower) errors over the 5.5m long z-axis.

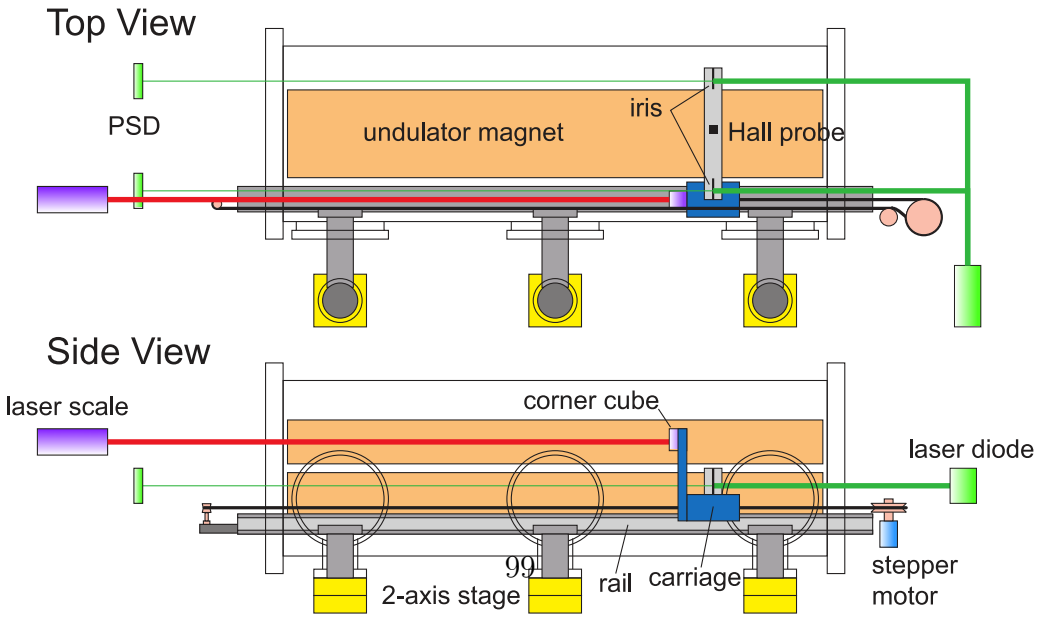

Figure 95: Layout of the SAFALI In-Vacuum measurement system.

The effect of the active trajectory compensation can be seen in figure 96 (Source: [10]), with a compensated trajectory error $\sigma_x = 5\mu m$ and $\sigma_y = 4\mu m$, that can be translated into peak-to-peak values of $\Delta x = 25\mu m$ and $\Delta y = 20\mu m$. This is at least an order of magnitude higher than what is achievable using traditional granite Hall-probe mappers.

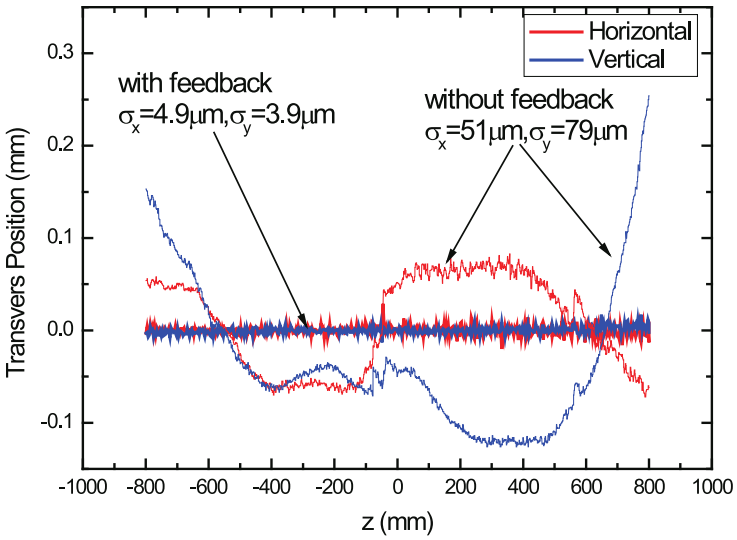

Figure 96: SAFALI Hall-probe position error with and without the dynamic feedback compensation.

Hall probe mappers, whether granite based or in-vacuum, can give local field information accurately and precisely but still can have small offset and non-linearity errors. When calculating the field integrals from the sum of all data points, these small errors can have a large impact on the integration results in the order of magnitude required by the insertion devices. That is why Hall-probe data is often corrected for field integrals using the results of another measurement system, usually induction based.

C.2 Induction Based Systems

The method of measuring the induced voltage of a coil moving in a magnetic field, or static coil in a varying magnetic field, is one of the oldest and well known methods of magnetic measurements [7]. It bases on Faraday's law of induction which states:

$$V = -N\frac{d\Phi}{dt} = -NA\frac{dB}{dt}. \tag{C.2}$$

Where V is the induced voltage, Φ is the magnetic flux crossing the coil, N is the number of turns and A is the area of the coil.
The use of induction coils for insertion device magnetic measurements is limited to field integral measurements and usually comes in two similar but distinct flavours, the Flip Coil system (FC) and the Stretch Wire system (SW).

C.2.1 Flip Coil System

A long and narrow coil of wire consisting of several turns can be placed in the ID gap, with the two coil leads connected to an integrator and a rotary stage used to flip the coil by 90° steps as in figure 97.

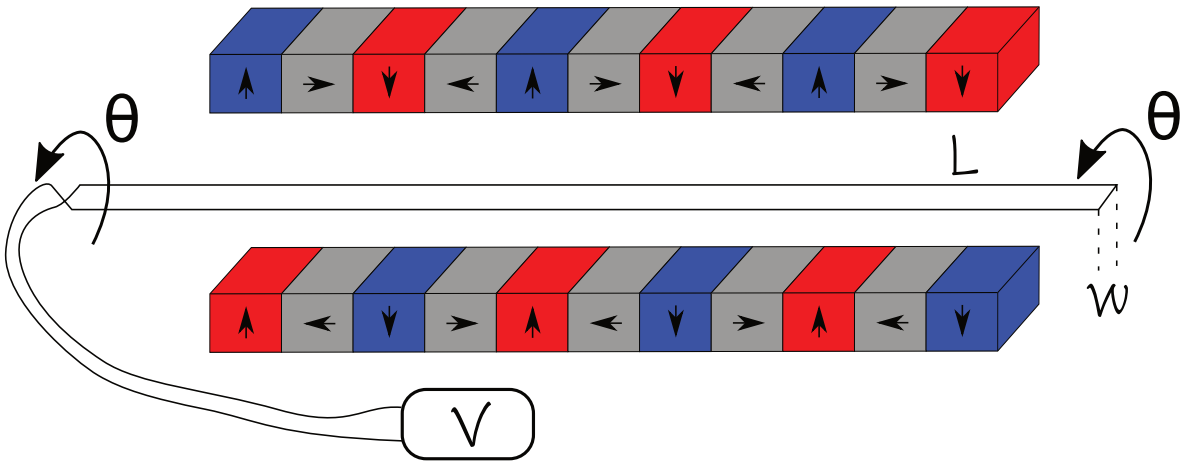

Figure 97: Sketch of the Flip Coil measurement system.

If the magnetic field is assumed static over the width of the coil (W), the resulting first field integrals are:

$$I_{1x} = \frac{-1}{NW}\int_{\theta=90°}^{\theta=270°} V \cdot dt \quad \text{and} \quad I_{1y} = \frac{-1}{NW}\int_{\theta=0°}^{\theta=180°} V \cdot dt. \tag{C.3}$$

The second field integrals can also be measured if one end of the coil was offset by 180° creating a triangular shaped coil:

$$I_{2x} = \frac{LI_{1x}}{2} + \frac{L}{2NW}\int_{\theta=90°}^{\theta=270°} V \cdot dt \quad \text{and} \quad I_{2y} = \frac{LI_{1y}}{2} + \frac{L}{2NW}\int_{\theta=0°}^{\theta=180°} V \cdot dt \tag{C.4}$$

The FC system gives very precise results (high repeatability) on the order of $\pm 0.5 \mu Tm$ peak-to-peak or better due to its high signal level and low noise, which are the result of high number of turns and small area, respectively.
However, due to the difficulties of knowing the exact coil width, the absolute value of the measured field integrals can be off by $1-5\%$, but this is usually not a problem for insertion devices since the field integrals are very low.
The coil width of a FC is usually around 5mm, which can also be problematic for use in small gap IDs such as in-vacuum devices.

C.2.2 Stretched Wire System

In the case of a stretched wire system, only a single thin wire ($N = 1$) is passed along the ID gap, and instead of rotation we translate the wire horizontally (Δx) or vertically (Δy) on both ends simultaneously. As before, we integrate the induced voltage signal. This setup is shown in figure 98.

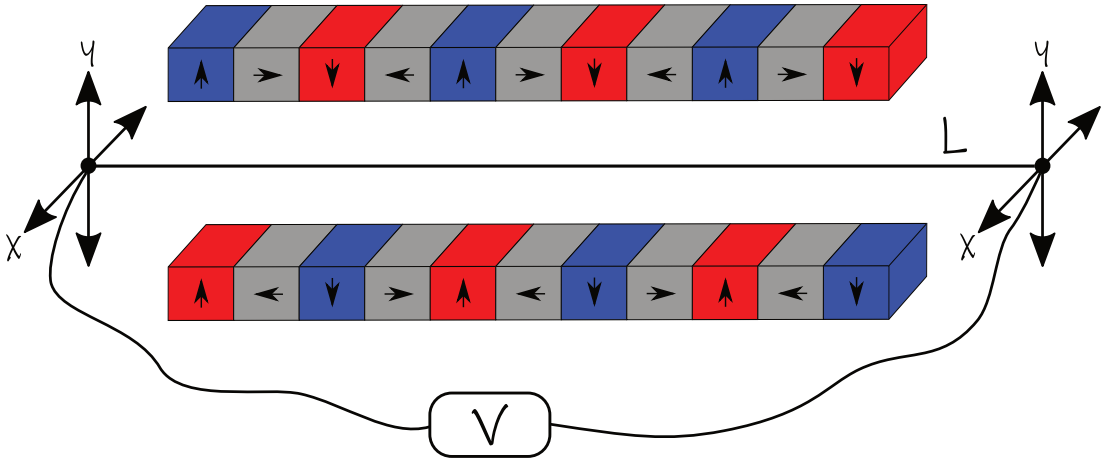

Figure 98: Sketch of the Stretch Wire measurement system.

If again the magnetic field is assumed constant over the wire translation, the resulting first field integrals are:

$$I_{1x} = \frac{-1}{\Delta y}\int_{y=y_0}^{y=y_0+\Delta y} V \cdot dt \quad \text{and} \quad I_{1y} = \frac{-1}{\Delta x}\int_{x=x_0}^{x=x_0+\Delta x} V \cdot dt. \tag{C.5}$$

The second field integrals can also be measured if one end of the coil was translated in the opposite direction of the other (e.g. Δx and $-\Delta x$), giving the result:

$$I_{2x} = \frac{LI_{1x}}{2} + \frac{L}{2\Delta y}\int_{y=y_0}^{y=y_0+\Delta y} V \cdot dt \quad \text{and} \quad I_{2y} = \frac{LI_{1y}}{2} + \frac{L}{2\Delta x}\int_{x=x_0}^{x=x_0+\Delta x} V \cdot dt. \tag{C.6}$$

The SW system gives very accurate results (low absolute error) in the order of 0.1% because it relies on the voltage and motion only, and both can be known accurately using nano-voltmeters and sub-μm precision linear encoders.
However the results are less repeatable than those of the FC due to low signal level and high noise, which are the result of the single turn and large area, respectively. This is why the typical peak-peak repeatability of a SW system is around $\pm 10 \mu T m$.
The SW can use wire diameters down to $50 \mu m$ comfortably, making it ideal for small gap IDs such as in-vacuum devices.

References

[1] Griffiths, D. J. (2017). Introduction to electrodynamics. Cambridge University Press.

[2] Barnes, P. Cockcroft, J. Jacques, S. Vickers, M. (n.d.) How do Synchrotrons Work? Retrieved from http://pd.chem.ucl.ac.uk/pdnn/inst2/work.htm

[3] NanoMAX Beamline Optics (n.d.) Retrieved from http://www.maxiv.lu.se/accelerators-beamlines/beamlines/nanomax/optics

[4] Clarke, J. A. (2004). The Science and Technology of Undulators and Wigglers. Oxford University Press.

[5] Dejus, R et al. (1995). Phase errors and predicted spectral performance of a prototype undulator. Review of Scientific Instruments, 66:2, 1875-1877.

[6] Walker, R. (1993). Interference effects in undulator and wiggler radiation sources. Nuclear Instruments & Methods in Physics Research, A 335, 328-337.

[7] Tumanski, S. (2011). Handbook of Magnetic Measurements. CRC Press.

[8] Kvitkovic, J. (1998). Hall Generators. CERN Accelerator School Measurement and Alignment of Accelerator and Detector Magnets, 98-05, 246-262.

[9] Wikimedia Commons, the free media repository (2019) Retrieved from https://commons.wikimedia.org/wiki/File:Zasada_dzia%C5%82ania_hallotronu.png.

[10] Tanaka, T. (2007). In-Situ Undulator Field Measurement with the SAFALI System. Proceedings of FEL 2007, Novosibirsk, Russia, 468-471.

[11] Graff, K. F. (1991). Wave Motion in Elastic Solids. Dover Publications.

[12] Warren, R. W. (1988). Limitations on the Use of the Pulsed-Wire Field Measuring Technique. Nuclear Instruments & Methods in Physics Research, A 272, 257-263.

[13] Arbelaez, D et al. (2013). A Dispersion and Pulse Width Correction Algorithm for the Pulsed Wire Method. Nuclear Instruments & Methods in Physics Research, A 716, 62-70.

[14] N'gotta, P. Ebbeni, M. Thiel, A. Tarawneh, H. (2019). First Results of a Pulse Wire Measurement System for ID Characterization at MAX IV. Proceedings of International Magnetic Measurement Workshop IMMW21, France.

[15] Riley, K. F. Hobson, M. P. Bence, S. J. (2006). Mathematical Methods for Physics and Engineering. Cambridge University Press.

[16] Dutt, A. Rokhlin, V. (1993). Fast Fourier Transforms for Nonequispaced data. Society for Industrial and Applied Mathematics, 14, 1368-1393.

[17] Wille, K. (2005). The Physics of Particle Accelerators An Introduction. Oxford University Press.

[18] Tarawneh, H. Thiel, A. Ebbeni, M. (2019). First commissioning results of phase I insertion devices at MAX IV Laboratory. AIP Conference Proceedings, 2054, 030023.

[19] Sorokin, V et al. (2021). Coupled longitudinal and transverse vibrations of tensioned Euler-Bernoulli beams with general linear boundary conditions. Mechanical Systems and Signal Processing, 150, 107244-107264.

[20] Langtangen, H. Linge, S. (2017). Finite Difference Computing with PDEs a Modern Software Approach. Cham: Springer.